Department of
Mining and Metallurgical Engineering

Technical University
of Nova Scotia

Halifax, Nova Scotia

TRANSMISSION ELECTRON MICROSCOPY STUDY ON THE EFFECTS OF SIMULATED RAIL LOADING ON AN EXPERIMENTAL PREMIUM RAIL STEEL

CONTRACT 20 SU.23440-0-9191

FINAL REPORT - DECEMBER 1983

by

E.E. Laufer

and

C. MacDonald

Transmission Electron Microscopy Study on the Effects of Simulated Rail Loading on an Experimental Premium Rail Steel

FINAL REPORT

by

E.E. Laufer and C. MacDonald
Technical University of Nova Scotia

Work on this project was conducted under the auspices of the Canada Centre for Mineral and Energy Technology, Energy, Mines and Resources Canada

DSS File Number	:	20SU.23440-0-9191
DSS Contract Serial Number	:	05U81-00231
CANMET Project Number	:	370071
CANMET Scientific Authority	:	Dr. D.M. Fegredo

December 31, 1983

145 pp

This report should be cited as Contract Report No. 0SU81-00231

MICROMEDIA
OCT 23 1985

TABLE OF CONTENTS

	PAGE
TABLE OF CONTENTS	i
LIST OF FIGURES	ii
TABLE	xiv
1. SUMMARY	1
2. INTRODUCTION	3
3. SPECIAL TECHNIQUES	5
4. OBSERVATIONS	9
4.1 New Samples	9
4.1.1 EEL-1: Upper Bainite, HRC 45	9
4.1.2 EEL-2: Upper Bainite, HRC 42	10
4.1.3 EEL-3: Upper Bainite, HRC 38	10
4.1.4 EEL-4: Transitional Pearlite, HRC 44.5	11
4.1.5 EEL-5: Pearlite, HRC 42	11
4.1.6 EEL-6: Pearlite, HRC 38.5	11
4.1.7 Tempered Martensite	11
4.2 Worn Samples	12
4.2.1 Bainite, HRC 45	13
4.2.1.1 Low Rail, Disc 32	13
4.2.1.2 High Rail, Disc 33	14
4.2.2 Bainite, HRC 42	16
4.2.2.1 Low Rail, Disc 8	16
4.2.2.2 High Rail, Disc 7	16

TABLE OF CONTENTS (Cont'd)

	PAGE
4.2.3 Bainite, HRC 37	17
4.2.3.1 Low Rail, Disc 30	17
4.2.3.2 High Rail, Disc 31	17
4.2.4 Transitional Pearlite, HRC 43-44	18
4.2.4.1 Low Rail, Disc 29	18
4.2.4.2 High Rail, Disc 28	18
4.2.5 Fine Pearlite, HRC 42	19
4.2.5.1 Low Rail, Disc 19	19
4.2.5.2 High Rail, Disc 20	19
4.2.6 Pearlite, HRC 38.5	20
4.2.6.1 Low Rail, Disc 14	20
4.2.6.2 High Rail, Disc 15	20
4.2.7 Tempered Martensite, HRC 45-46	22
4.2.7.1 Low Rail, Disc 36	22
4.2.7.2 High Rail, Disc 37	22
4.2.8 Tempered Martensite, HRC 43	23
4.2.8.1 Low Rail, Disc 38	23
4.2.8.2 High Rail, Disc 39	23
4.2.9 Tempered Martensite, HRC 38-39	24
4.2.9.1 Low Rail, Disc 40	24
4.2.9.2 High Rail, Disc 41	24
4.2.10 Bainite with Martensite	25
4.2.10.1 High Rail, Disc 12	25
5. DISCUSSION	27
5.1 Identification of Texture	27
5.2 Comparison of Microstructures	28
5.3 Effect of Martensite Particles	30

TABLE OF CONTENTS (Cont'd)

		PAGE
6.	APPENDIX	31
6.1	Sample Codes	31
6.2	Principles of Image Formation in the TEM	31
7.	REFERENCES	37

LIST OF FIGURES

FIGURE		
3-1	Sampling for TEM	5
3-2	Disc 12, 250 μm below surface. Electropolished 50 000 X. (Neg. 1835)	F-1
3-3	Same sample as shown in figure 3-2, after subsequent ion thinning. 100 000 X (Neg. 1881)	F-1
3-4	Disc 19. Optical micrograph, showing premature perforation at sub-surface microcracks. 220 X.	F-2
4.1-1	EEL-1, Upper Bainite, Lath microstructure. 50 000 X. (Neg. 1157)	F-3
4.1-2	EEL-1, Upper Bainite. High density of carbide-decorated dislocations. 50 000 X. (Neg. 1162)	F-3
4.1-3	EEL-1, Upper Bainite. Sub-grains and high dislocation density. 25 000 X. (Neg. 1159)	F-4
4.1-4	EEL-1, Upper Bainite. As 4.1-3, 50 000 X. (Neg. 1161)	F-4
4.1-5	EEL-2, Upper Bainite. Compare sub-grain structure with figure 4.1-3. 50 000 X. (Neg. 1116)	F-5
4.1-6	EEL-2, Upper Bainite. Typical region showing high dislocation density. 50 000 X. (Neg. 1187)	F-5
4.1-7	Upper Bainite, transformed at 460°C. Compare figures 4.1-2 and 6. 50 000 X (Neg. 1092)	F-6

TABLE OF CONTENTS (Cont'd)

FIGURE		PAGE
4.1-8	EEL-3, Upper Bainite, transformed at 460°C. 50 000 X. (Neg. 1055)	F-6
4.1-9	EEL-4, Transitional pearlite, 50 000 X. Neg. 1065)	F-7
4.1-10	EEL-4, Transitional pearlite. 50 000 X. (Neg. 1072)	F-7
4.1-11	EEL-5, Fine pearlite, 100 000 X. (Neg 1013).	F-8
4.1-12	EEL-5, Fine pearlite. High dislocation density is atypical, 100 000 X. (Neg. 1020)	F-8
4.1-13	EEL-6, Fine pearlite, 50 000 X (Neg. 1123)	F-9
4.1-14	EEL-6, Fine pearlite, 50 000 X (Neg. 1133)	F-9
4.1-15	EEL-7, Tempered at 510°C. 25 000 X. (Neg. 2224)	F-10
4.1-16	EEL-7, Tempered at 510°C. 50 000 X. (Neg. 2152)	F-10
4.1-17	EEL-8, Tempered at 566°C. 25 000 X. (Neg. 2192)	F-11
4.1-18	EEL-8, Tempered at 566°C. Part of figure 4.1-17 50 000 X. (Neg. 2194)	F-11
4.1-19	EEL-9, Tempered at 616°C. 25 000 X. (Neg. 2290)	F-12
4.1-20	EEL-9, Tempered at 616°C. 50 000 X. (Neg. 2285)	F-12
4.2-1a	Disc 32, 260 μm from tread surface. 25 000 X. Compare figure 4.1-3 (Neg. 2235)	F-13
4.2-1b	Diffraction pattern corresponding to central portion of figure 4.2-1a. 3.5 μm S.A. (Neg 2236)	F-13
4.2-2a	Disc 32, 220 μm from tread surface, 25 000 X. (Neg 2237)	F-14
4.2-2b	Diffraction pattern corresponding to central portion of figure 4.2-2a. 3.5 μm S.A. (Neg. 2238)	F-14
4.2-3a	Disc 32, 80 μm from tread surface. 50 000 X. (Neg. 1988)	F-15

TABLE OF CONTENTS (Cont'd)

FIGURE		PAGE
4.2-3b	Diffraction pattern corresponding to figure 4.2-3a. 3.5 μm S.A. (Neg. 1989)	F-15
4.2-4a	Disc 32, 37 μm from tread surface. 50 000 X. (Neg. 2239)	F-16
4.2-4b	Diffraction pattern corresponding to figure 4.2-4a. 3.5 μm S.A. (Neg. 2240)	F-16
4.2-5a	Disc 33, 200 μm from gage surface. 50 000 X. (Neg. 1808)	F-17
4.2-5b	Diffraction pattern corresponding to figure 4.2-5a. 3.5 μm S.A. (Neg. 1810)	F-17
4.2-5c	Dark field image corresponding to figure 4.2-5a. {110} reflection. (Neg. 1811)	F-18
4.2-6a	Disc 33, 200 μm from gage surface. 50 000 X. (Neg. 1812)	F-19
4.2-6b	Diffraction pattern corresponding to figure 4.2-6a. 3.5 μm S.A. (Neg. 1813)	F-19
4.2-6c	Dark field image corresponding to figure 4.2-6a. {110} reflection. (Neg. 1814)	F-20
4.2-7a	Disc 33, 170 μm from field surface. 25 000 X (Neg. 1779)	F-21
4.2-7b	Diffraction pattern corresponding to central portion of figure 4.2-7a. 3.5 μm S.A. (Neg. 1780)	F-21
4.2-8a	Disc 33, 60 μm from tread surface. 25 000 X. (Neg. 1794)	F-22
4.2-8b	Diffraction pattern corresponding to central portion of figure 4.2-8a. 3.5 μm S.A. (Neg. 1803)	F-23
4.2-9a	Disc 33, 60 μm from tread surface. 75 000 X. (Neg. 1822)	F-23
4.2-9b	Disc 33, 60 μm from tread surface. 75 000 X. (Neg. 1823)	F-23
4.2-10a	Disc 33, 34 μm from tread surface. 25 000 X. (Neg. 1790)	F-24

TABLE OF CONTENTS (Cont'd)

FIGURE		PAGE
4.2-10b	Diffraction pattern corresponding to figure 4.2-10a. 3.5 μm S.A. (Neg. 1789)	F-24
4.2-11a	Disc 33, 24 μm below tread surface. 100 000 X. (Neg. 1805)	F-25
4.2-12a	Disc 33, 14 μm below tread surface. 75 000 X. (Neg. 1786)	F-26
4.2-12b	Diffraction pattern corresponding to central region of figure 4.2-12a. 0.9 μm S.A. (Neg. 1787)	F-26
4.2-13a	Disc 8, 240 μm below gage surface. 50 000 X. (Neg. 1272)	F-27
4.2-13b	Diffraction pattern corresponding to central portion of figure 4.2-13a. (Neg. 1273)	F-27
4.2-14a	Disc 8, approximately 35 μm below gage surface. 50 000 X. (Neg. 1870)	F-28
4.2-14b	Diffraction pattern corresponding to figure 4.2-14a. 3.5 μm S.A. (Neg. 1873)	F-28
4.2-15a	Disc 8, approximately 8 μm below field surface. 50 000 X. (Neg. 1855)	F-29
4.2-15b	Diffraction pattern corresponding to central portion of figure 4.2-15a. 0.9 μm S.A. (Neg. 1856).	F-29
4.2-15c	Dark field image corresponding to figure 4.2-15a. {110} reflection. (Neg. 1858)	F-30
4.2-16	Disc 8, approximately 8 μm below field surface, showing incipient crack. 50 000 X. (neg. 1861)	F-30
4.2-17	Disc 7, 640 μm below field surface. 50 000 X. (Neg. 1532)	F-31
4.2-18	Disc 7, 300 μm below field surface. 100 000 X. (Neg 1364)	F-31
4.2-19a	Disc 7, 40 μm below field surface. 75 000 X. (Neg. 1561)	F-32

TABLE OF CONTENTS (Cont'd)

FIGURE		PAGE
4.2-19b	Diffraction pattern corresponding to central portion of figure 4.2-19a. 0.9 μm S.A. (Neg. 1562)	F-32
4.2-20a	Disc 7. 58 μm below surface, 2 mm from gage corner. 100 000 X. (Neg. 1556)	F-33
4.2-20b	Diffraction pattern corresponding to figure 4.2-20a. 0.9 μm S.A. (Neg. 1557)	F-33
4.2-21a	Disc 7, 30 μm below surface, 2 mm from gage corner. 100 000 X. (Neg. 1548)	F-34
4.2-21b	Diffraction pattern corresponding to figure 4.2-21a. 0.9 μm S.A. (Neg. 1550)	F-34
4.2-22a	Disc 7, at surface, 2 mm from gage corner. 50 000 X. (Neg. 1543)	F-35
4.2-22b	Diffraction pattern of surface region of figure 4.2-22a. 0.9 μm S.A. (Neg. 1537)	F-36
4.2-23	Dark field micrograph of part of figure 4.2-22a 100 000 X. (Neg. 1542)	F-36
4.2-24	Disc 30, 250 μm below tread surface. 50 000 X. (Neg. 2349)	F-37
4.2-25a	Disc 30, 90 μm below field surface. 50 000 X. (Neg. 2351)	F-38
4.2-25b	Diffraction pattern corresponding to figure 4.2-25a. 3.5 μm S.A. (Neg. 2352)	F-38
4.2-26a	Disc 31, 65 μm below field surface. 50 000 X. (Neg. 2299)	F-39
4.2-26b	Diffraction pattern corresponding to figure 4.2-26a. 3.5 μm S.A. (Neg. 2300)	F-39
4.2-27a	Disc 31, 50 μm below field surface. 25 000 X. (Neg. 2304)	F-40
4.2-27b	Diffraction pattern corresponding to central portion of figure 4.2-27a. 3.5 μm S.A. (Neg. 2307)	F-40

TABLE OF CONTENTS (Cont'd)

FIGURE		PAGE
4.2-28a	Disc 31, 40 μm below field surface. 50 000 X. (Neg. 2297)	F-41
4.2-28b	Diffraction pattern corresponding to figure 4.2-28a. 3.5 μm S.A. (Neg. 2298)	F-41
4.2-29a	Disc 31, 130 μm below tread surface. 25 000 X. (Neg. 2319)	F-42
4.2-29b	Diffraction pattern corresponding to central portion of figure 4.2-29a. 3.5 μm S.A. (Neg. 2320)	F-42
4.2-30a	Disc 31, 80 μm below tread surface. 25 000 X. (Neg. 2317)	F-43
4.2-30b	Diffraction pattern corresponding to central portion of figure 4.2-30a. 3.5 μm S.A. (Neg. 2318)	F-43
4.2-31a	Disc 31, 33 μm below tread surface. 50 000 X. (Neg. 2291)	F-44
4.2-31b	Diffraction pattern corresponding to figure 4.2-31a. 3.5 μm S.A. (Neg. 2292)	F-44
4.2-32a	Disc 31, 75 μm below gage surface. 25 000 X. (Neg. 2311)	F-45
4.2-32b	Diffraction pattern corresponding to central portion of figure 4.2-32a. 0.9 μm S.A. (Neg. 2313)	F-45
4.2-33a	Disc 31, 30 μm below gage surface. 25 000 X. (Neg. 2314)	F-46
4.2-33b	Diffraction pattern corresponding to central portion of figure 4.2-33a. 0.9 μm S.A. (Neg. 2316)	F-46
4.2-34a	Disc 39, 550 μm below tread surface. 50 000 X. (Neg. 2347)	F-47
4.2-34b	Diffraction pattern corresponding to figure 4.2-34a. 3.5 μm S.A. (Neg. 2348).	F-47

TABLE OF CONTENTS (Cont'd)

FIGURE		PAGE
4.2-35a	Disc 29, 110 µm below tread surface. 25 000 X. (Neg. 2343)	F-48
4.2-35b	Diffraction pattern corresponding to central portion of figure 4.2-36a. 3.5 µm S.A. (Neg. 2344)	F-48
4.2-36a	Disc 29, 70 µm below tread surface. 25 000 X. (Neg. 2345)	F-49
4.2-36b	Diffraction pattern corresponding to central portion of figure 4.2-37a. 3.5 µm S.A. (Neg. 2346)	F-49
4.2-37a	Disc 28, 100 µm below field surface. 50 000 X. (Neg. 2353)	F-50
4.2-37b	Diffraction pattern corresponding to figure 4.2-37a. 3.5 µm S.A. (Neg. 2354).	F-50
4.2-38a	Disc 19, 110 µm below field surface. 75 000 X. (Neg. 2116)	F-51
4.2-38b	Diffraction pattern corresponding to figure 4.2-38a. 3.5 µm S.A. (Neg. 2117)	F-51
4.2-39a	Disc 19, 12 µm below field surface. 75 000X. (Neg. 2110)	F-52
4.2-39b	Diffraction pattern corresponding to figure 4.2-39a. 3.5 µm S.A. (Neg. 2111)	F-52
4.2-40a.	Disc 19, 6 µm below field surface. 75 000 X. (Neg. 2106)	F-53
4.2-40b	Diffraction pattern corresponding to figure 4.2-40a. 3.5 µm S.A. (Neg. 2108)	F-53
4.2-41a	Disc 20, 130 µm below tread surface. 50 000X. (Neg. 2243)	F-54
4.2-41b	Diffraction pattern corresponding to figure 4.2-41a. 3.5 µm S.A. (Neg. 2244)	F-54
4.2-42a	Disc 20, 75 µm below tread surface. 50 000 X. (Neg. 2247)	F-55

TABLE OF CONTENTS (Cont'd)

FIGURE		PAGE
4.2-42b	Diffraction pattern corresponding to figure 4.2-42a. 3.5 μm S.A. (Neg. 2248)	F-55
4.2-43a	Disc 20, 30 μm below tread surface. 50 000 X. (Neg. 2245)	F-56
4.2-43b	Diffraction pattern corresponding to figure 4.2-43a. 3.5 μm S.A. (Neg. 2246)	F-56
4.2-44a	Disc 14, 300 μm below tread surface. 75 000 X. (Neg. 1944)	F-57
4.2-44b	Diffraction pattern corresponding to figure 4.2-44a. (Neg. 1945)	F-57
4.2-45a	Disc 14, 75 μm below tread surface. 75 000 X. (Neg. 1941)	F-58
4.2-45b	Diffraction pattern corresponding to figure 4.2-45a. (Neg. 1940)	F-58
4.2-46a	Disc 14, at tread surface. 100 000 X. (Neg. 1746)	F-59
4.2-46b	Diffraction pattern corresponding to figure 4.2-46a. 0.9 μm S.A. (Neg. 1747)	F-59
4.2-47a	Disc 14, 72 μm below gage surface. 75 000 X. (Neg. 2426)	F-60
4.2-47b	Diffraction pattern corresponding to figure 4.2-47a. 3.5 μm S.A. (Neg. 2427)	F-60
4.2-48a	Disc 14, 30 μm below gage surface. 75 000 X. (Neg. 2422)	F-61
4.2-48b	Diffraction pattern corresponding to figure 4.2-48a. 3.5 μm S.A. (Neg. 2423)	F-61
4.2-49a	Disc 15, 140 μm below tread surface. 50 000 X. (Neg. 2132)	F-62
4.2-49b	Diffraction pattern corresponding to figure 4.2-49a. 3.5 μm S.A. (Neg. 2130)	F-62

TABLE OF CONTENTS (Cont'd)

FIGURE		PAGE
4.2-50a	Disc 15, 55 μm below gage surface. 75 000 X. (Neg. 2122)	F-63
4.2-50b	Diffraction pattern corresponding to figure 4.2-50a. 3.5 μm S.A. (Neg. 2123)	F-63
4.2-51a	Disc 15,10 μm below tread surface. 75 000 X. (Neg. 2003)	F-64
4.2-51b	Diffraction pattern corresponding to figure 4.2-51a. 0.9 μm S.A. (Neg. 2004)	F-64
4.2-52a	Disc 36, 110 μm below gage surface. 50 000 X. (Neg. 2142)	F-65
4.2-52b	Diffraction pattern corresponding to figure 4.2-52a. 3.5 μm S.A. (Neg. 2143)	F-65
4.2-53a.	Disc 36, 90 μm below gage surface. 75 000 X. (Neg. 2144)	F-66
4.2-53b	Diffraction pattern corresponding to figure 4.2-53a. 3.5 μm S.A. (Neg. 2145)	F-66
4.2-54a	Disc 36, 75 μm below field surface. 50 000 X. (Neg. 2150)	F-67
4.2-54b	Diffraction pattern corresponding to figure 4.2-54a. 3.5 μm S.A. (Neg. 2151)	F-67
4.2-55a	Disc 36, 20 μm below field surface. 75 000 X. (Neg. 2015)	F-68
4.2-55b	Diffraction pattern corresponding to figure 4.2-55a. (Neg. 2016)	F-68
4.2-56a	Disc 37, 150 μm below tread surface. 75 000 X. (Neg. 2084)	F-69
4.2-56b	Diffraction pattern corresponding to figure 4.2-56a. 3.5 μm S.A. (Neg. 2085)	F-69
4.2-57a	Disc 37, 90 μm below tread surface. 75 000 X. (Neg. 2080)	F-70
4.2-57b	Diffraction pattern corresponding to figure 4.2-57a. 3.5 μm S.A. (Neg. 2081)	F-70

TABLE OF CONTENTS (Cont'd)

FIGURE		PAGE
4.2-58a	Disc 37, 75 µm below tread surface. 75 000 X. (Neg. 2058)	F-71
4.2-58b	Diffraction pattern corresponding to figure 4.2-58a. 3.5 µm S.A. (Neg. 2059)	F-71
4.2-59a	Disc 37, 50 µm below gage surface. 75 000 X. (Neg. 2041)	F-72
4.2-59b	Diffraction pattern corresponding to figure 4.2-59a. 3.5 µm S.A. (Neg. 2040)	F-72
4.2-60a	Disc 38, 130 µm below field surface. 75 000 X. (Neg. 2196)	F-73
4.2-60b	Diffraction pattern corresponding to figure 4.2-60a. 3.5 µm S.A. (Neg. 2197)	F-73
4.2-61a	Disc 38, 35 µm below tread surface. 75 000 X. (Neg. 2177)	F-74
4.2-61b	Diffraction pattern corresponding to figure 4.2-61a. 3.5 µm S.A. (Neg. 2178)	F-74
4.2-62a	Disc 38, 20 µm below tread surface. 50 000 X. (Neg. 2183)	F-75
4.2-62b	Diffraction pattern corresponding to figure 4.2-62a. 3.5 µm S.A. (Neg. 2184)	F-75
4.2-63a	Disc 39, 180 µm below the field surface. 25 000 X. (Neg. 2226)	F-76
4.2-63b	Diffraction pattern corresponding to figure 4.2-63a. 3.5 µm S.A. (Neg. 2227)	F-77
4.2-63c	Diffraction pattern corresponding to a single grain in figure 4.2-63a. 0.9 µm S.A. (Neg. 2228)	F-77
4.2-64a	Disc 39, 35 µm below field surface. 50 000 X. (Neg. 2133)	F-78
4.2-64b	Diffraction pattern corresponding to figure 4.2-64a. 3.5 µm S.A. (Neg. 2134)	F-78

TABLE OF CONTENTS (Cont'd)

FIGURE		PAGE
4.2-65a	Disc 40, 260 µm below field surface. 50 000 X. (Neg. 2162)	F-79
4.2-65b	Diffraction pattern corresponding to figure 4.2-65a. 3.5 µm S.A. (Neg. 2163)	F-79
4.2-66a	Disc 40, 35 µm below tread surface. 50 000 X. (Neg. 2269)	F-80
4.2-66b	Diffraction pattern corresponding to figure 4.2-66a. 3.5 µm S.A. (Neg. 2270)	F-80
4.2-67a	Disc 40, 10 µm below tread surface. 50 000 X. (Neg. 2263)	F-81
4.2-67b	Diffraction pattern corresponding to figure 4.2-67a. 3.5 µm S.A. (Neg. 2264)	F-81
4.2-68a	Disc 41, 135 µm below field surface. 50 000 X. (Neg. 2278)	F-82
4.2-68b	Diffraction pattern corresponding to figure 4.2-68a. 3.5 µm S.A. (Neg. 2279)	F-82
4.2-69a	Disc 41, 80 µm below field surface. 50 000 X. (Neg. 2276)	F-83
4.2-69b	Diffraction pattern corresponding to figure 4.2-69a. 3.5 µm S.A. (Neg. 2277)	F-83
4.2-70a	Disc 41, 50 µm below tread surface. 50 000 X. (Neg. 2257)	F-84
4.2-70b	Diffraction pattern corresponding to figure 4.2-70a. 3.5 µm S.A. (Neg. 2258)	F-84
4.2-71	Disc 41, 70 µm below tread surface. Overview showing elongated grain structure. 15 000 X. (Neg. 2284)	F-85
4.2-72	Disc 12, 160 µm below gage surface. Opaque areas are martensite. 2 000 X. (Neg. 2198)	F-86
4.2-73	Disc 12, 160 µm below gage surface. Note increased deformation between martensite particles. 6 000 X. (Neg. 2199)	F-87

TABLE OF CONTENTS (Cont'd)

FIGURE		PAGE
4.2-74	Sketch showing locations of figures 4.2-75 to 4.2-78. Compare figure 4.2-73.	F-88
4.2-75a	Disc 12, 160 μm below gage surface. Augmented deformation near martensite. 25 000 X. (Negs. 2202, 2203)	F-89
4.2-75b	Diffraction pattern corresponding to figure 4.2-75a. 3.5 μm S.A. (Neg. 2333)	F-90
4.2-76	Disc 12. 160 μm below gage surface. 25 000 X. (Neg. 2204)	F-91
4.2-77a	Disc 12, 160 μm below gage surface, 20 μm from martensite. Compare figure 4.2-29. 25 000 X. (Neg. 2208)	F-92
4.2-77b	Diffraction pattern corresponding to figure 4.2-77a. 3.5 μm S.A. (Neg. 2209)	F-92
4.2-78	Disc 12, 160 μm below gage surface. Detail of martensite particle. 25 000 X. (Neg. 2207)	F-93
6.1	Schematic ray diagram illustrating the formation of a diffraction pattern and an intermediate image by the objective lens of an electron microscope (adapted from Head et al. (6)).	33

LIST OF TABLES

TABLE		
6.1	Equivalent sample codes	32

1. Summary

TEM samples were prepared from thirty specimens of rail steel, as follows:

- steel transformed at 385°C to produce Bainite, HRC 45.
- steel transformed at 415°C to produce Bainite, HRC 42.
- steel transformed at 460°C to produce Bainite, HRC 38.
- steel transformed at 570°C to produce very fine Pearlite or Transitional Pearlite, HRC 44.5.
- steel transformed at 595°C to produce Pearlite, HRC 42.
- steel transformed at 627°C to produce Pearlite, HRC 38.5.
- steel austenetized at 816°C, oil-quenched to produce martensite, and tempered at 510°C for 1 hour to HRC 45-46.
- martensite as above, tempered at 566°C for 1 hour to HRC 43.
- martensite as above, tempered at 616°C for 1 hour to HRC 38-39.
- steel incompletely transformed at 460°C to Bainite, HRC 38, with martensite inclusions.

The last steel mentioned was prepared to investigate the possible effects of accidentally formed martensite, e.g., in a weldment. All steels were examined in the un-tested, tested as low rail and tested as high rail conditions. In addition, some attempt was made to separate all tested samples into gage, tread and field regions. The purpose of the observations was to compare the microstructures formed during simulated rail loading, especially microstructures formed close to the sample surface, in order to attempt to explain the observation that, for a given hardness, pearlite wears better than bainite while tempered martensite is inferior to both.

All tested samples examined showed the following:

- an ultra-fine ferrite grain size in the near-surface regions, especially within about 30 μm of the running surface. Grains are flattened or elongated, parallel to the running surface;

- a texture in the ultra-fine grain region. While this texture was not studied in detail, the electron diffraction patterns obtained are consistent with a ⟨111⟩ wire texture, with ⟨111⟩ parallel to the rolling direction or direction of travel of the train;

- deformation of cementite;

- re-alignment of cementite parallel to the running surface. The cementite often defines grain boundaries.

- For a given depth below the running surface, more deformation was observed on the gage than on the field side, and the high rail showed more deformation than the low rail.

Thus, while observations are to some extent still incomplete, it appears that the integrity of the cementite in the pearlitic and bainitic structures is preserved on deformation. The more nearly continuous re-inforcing cementite lamellae of the pearlite then give it better properties than the bainite. The bainite, in turn, has more nearly continuous cementite in its microstructure than the tempered martensite, and better properties. The hardness test on the original microstructure is not a reliable measure of wear resistance.

2. Introduction

The Technical University of Nova Scotia responded to a CANMET requirement for the examination of samples of several experimental rail steels, subjected to simulated rail loading. The steels were all of the same composition, i.e.,

C	Mn	Si	S	P	Cr	Mo
0.72	0.79	0.25	0.023	0.009	0.78	0.21

but subjected to different heat treatments, as shown in Table 6.1. The microstructures examined were thus Bainite, at HRC 45, 42 and 38; pearlite, including "transitional" pearlite, at HRC 44, 42 and 38.5 and tempered martensite, at HRC 45-46, 43 and 38-39. All samples had been subjected to the same test sequence on the disc-on-disc testing machine described by Kalousek[1], as follows:

- The first 40 000 revolutions, equivalent to 1 million gross tons (MGT) of service, were run dry.
- The next 760 000 revolutions (2nd to 20th MGT) were run in a grease/20% sand environment.
- The next 40 000 revolutions (21st MGT) were run dry and,
- The final 1 560 000 revolutions (22nd - 60th MGT) were run with pure grease lubricant.

The load was maintained constant at 800 lb. (3.6×10^3 N) per wheelset during tests. Angles of attack of $10'$, $18'$, $32'$ and $40'$ were applied successively for 2 500 revolutions each, then decreased in order to complete a cycle of 20 000 revolutions. After 20 000 revolutions, the direction of rotation of the discs, simulating wheels and rails, was reversed.

Specimens were examined after a total of 2.4×10^6 revolutions, or a simulated 60 MGT of service.

As a result of these tests, it was observed that, for any given hardness, the pearlite showed less wear than the bainite, and the tempered martensite considerably more. It was therefore of interest to observe and compare the microstructures in all worn samples.

A secondary experiment involved the preparation of a specimen similar to EEL-3 (Table 6.1), i.e., bainite at HRC 38, but containing martensite inclusions as might occur on field welding of such a steel. This specimen was subjected to the same test sequence, and examined using TEM, to study the flow of matrix metal in the vicinity of the martensite particles.

3. Special Techniques

In order to obtain thin foils for TEM at the worn surfaces of the samples and at known distances below the surface, the samples were electro-plated and sectioned as shown in Figure 1. Nickel was used for electro-plating, since it can be electro-polished at very nearly the same rate as steel in solutions based on perchloric acid and since, being fcc, it is readily distinguished from the bcc ferrite or orthorhombic cementite present in the steel.

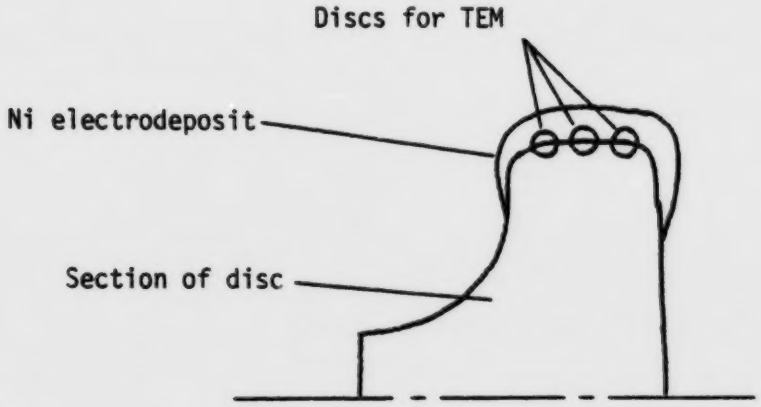

FIGURE 3-1: Sampling for TEM

The electro-plating of the samples initially presented great difficulty, as absolutely perfect bonding is required to assure the integrity of the thin foils and to preserve the surface. A good bond could not be obtained without thorough cleaning of the surface, and most suggested cleaning procedures involved significant loss of material, which could not be tolerated. The procedure finally adopted involved the following steps:

1. Ultrasonic clean using distilled water and detergent.

2. Clean, using organic solvent, and "Q-tip" swabs.

3. Ultrasonically clean in organic solvents.

4. Rinse with clean solvent from squeeze bottle.

5. Repeat 2-4.

6. Anodically clean, in solution of "Oakite 290" (Oakite Products Inc., U.S.A.)

7. Activate in "Actane 82" (Enthone, Inc., U.S.A.)

8. Nickel plate ($NiCl_2 \cdot 6H_2O$, 300 g/ℓ, H_3BO_3, 38 g/ℓ, $NaC_{15}H_{45}SO_4$, 0.50 g/ℓ, 50-70°C, pH = 2.0, 5 - 55 A/dm^2)

The entire cleaning and activating sequence was carried out on a test sample, a part of which had been masked with lacquer. On removing the lacquer, it was not possible to discern any step in the surface, on focusing an optical microscope alternately on the cleaned portion and on the lacquered portion. A step height of 1 μm would have been detectable. It was therefore concluded that the cleaning procedure removed less than 1 μm of material, and measurements of depth below the surface are given with this degree of confidence.

Discs of 1.5 mm diameter were cut as indicated, and each disc was electropolished in a jig, so that a perforation occurred at or near the Ni - sample interface. The periphery of the perforation was generally transparant to electrons

and suitable for observation. The regions examined could be located with an optical microscope, and the distances from the interface measured. Where the interface itself was visible in the TEM, the distance of an observed field from the surface was measured in the TEM, using the calibrated stage drive.

Jet electro-polishing of the TEM discs was carried out using a solution consisting of:

30 mℓ $HC\ell O_3$

45 mℓ Butoxyethanol

225 mℓ Methanol

as recommended by Charest[2], at -50°C and approximately 30 V, giving a current of about 100 mA or a current density of about 400 A $(dm)^{-2}$. A moderately high jet velocity was used.

Certain difficulties experienced in sample preparation are worth mentioning. While perforation of a well-polished disc always occurred very near the centre of that part of the disc exposed to the electropolishing solution, the precise location of the thin area involved a certain element of chance, as did the precise location of the disc in the electropolishing jig. Thus, an element of chance entered into the selection of thinned regions for TEM viewing. Any attempt to extend a perforation, to bring it to a more desirable region of a disc by continued electropolishing, failed to produce new thin (transparent) regions. The electropolishing always acted preferentially on the edges of the perforation, consuming thin area as the perforation was enlarged.

Attempts to increase thin areas by ion beam milling were also unsuccessful. In this case, the thin areas were indeed extended, but ion damage was observed, so that it would not be possible to have confidence that observed sample deformation was due entirely to the wear testing and not to the ion thinning. Figures 3-2 and 3-3 show regions of the same sample before and after ion thinning: the damage is apparent as regions of "black death" in the ion-thinned sample. An Edwards ion thinning unit was used, employing 5 kV argon ions, and a sample current of about 30 μA.

Another difficulty was experienced with cleaning of certain samples, prior to electroplating. We were often unable to adequately clean portions of discs where metal flow had formed a hooked edge, e.g., the gage corner of certain high rail discs. Separation of the Ni plating from the sample sometimes resulted as the samples were in the final stages of thinning.

A third difficulty was encountered with samples containing sub-surface cracks. In these cases, premature perforation often occurred by enlargement of these cracks, precluding proper sample preparation by subsequent electropolishing. Figure 3-4 illustrates this effect.

4. OBSERVATIONS

All samples were examined by transmission electron microscopy. A very brief review of the method is given in appendix 6.2, and good detailed treatises are numerous, including Hirsch et al.[3], Agar et al.[4] and Edington[5] among others. Sample coding is summarized in appendix 6.1.

4.1 New Samples

Samples EEL-1 through EEL-6 were examined as new, un-worn material to establish a reference against which to compare the worn samples. Samples EEL-1 to EEL-9 were examined only as worn samples. However, specimens taken from these samples at depths of 1 mm or more were essentially un-deformed, and examples of these are shown in this section as "new" samples.

4.1.1 EEL-1: Upper Bainite, HRC 45.

Sample EEL-1 was transformed at 385°C, to Upper Bainite of HRC 45. At the level of resolution of the TEM, the bainitic microstructure is strikingly different from pearlite in three respects:

- the well-known lath microstructure is well resolved (figure 4.1-1).
- the cementite lamellae are not continuous (figures 4.1-1 to 4)
- the dislocation density in the ferrite matrix is very high, even in the un-deformed material (compare figures 4.1-4 and 4.1-12).

Figures 4.1-1 to 4.1-4 are typical. Figure 4.1-1 illustrates the lath microstructure. Figure 4.1-2 shows the high dislocation density, and also shows apparently unsharp dislocation images. However, much of the apparent unsharpness is in fact due to fine precipitates, presumably fine carbides, on the dislocations. This was not observed in samples transformed at higher temperatures. Figures 4.1-3 and 4 show the same region of a sample at different magnifications. The high dislocation density is again apparent, and also the presence of sub-grains. A small correction of the orientation of the sample in the microscope would cause the dull, apparently dislocation-free areas of figures 4.1-3 or 4 to appear in good contrast, and to show their true high dislocation content. The regions now bright would then appear out of contrast.

4.1.2 EEL-2: Upper Bainite, HRC 42.

Sample EEL-2 was transformed at 415°C, to Upper Bainite of HRC 42. This sample has a microstructure almost indistinguishable from that of EEL-1, although perhaps less fine in scale. Figure 4.1-5, for example, is very similar to figures 4.1-3 and 4, and figure 4.1-6 may be compared to figures 4.1-1 and 2. Note however, that the dislocations in Figure 4.1-6 are clean, not decorated with carbides. This decoration of dislocations with carbides seems to indicate some differences in transformation mechanisms as temperatures are increased. It was frequently observed in EEL-1 (385°C), seldom in EEL-2 (415°C) and never in EEL-3 (460°C). Possibly, the EEL-1 steel should be considered as lower Bainite.

4.1.3 EEL-3: Upper Bainite, HRC 38.

Sample EEL-3 was transformed at 460°C, to Upper Bainite of HRC 38. The microstructure is similar to EEL-1 and 2, but less fine. Again, the dislocation density is high, Figures 4.1-7 and 8 are typical.

4.1.4 EEL-4: Transitional Pearlite, HRC 44.5

Sample EEL-4 was transformed at 570°C to transitional pearlite at HRC 44.5. The sample in fact consisted mainly of very fine pearlite. The very much reduced dislocation density of the pearlite, compared to Bainite, is remarkable. Figures 4.1-9 and 10 are typical. The lamellar spacing of the pearlite is about 60 nm.

4.1.5 EEL-5: Pearlite, HRC 42.

Sample EEL-5 was transformed at 595°C to fine pearlite of HRC 42. The microstructure observed was similar to that of EEL-4, but slightly less fine, with a lamellar spacing of about 70 nm. The dislocation density was generally low, and such heavily dislocated areas as that of figure 4.1-12 were the exception rather than the rule. Figure 4.1-11 is more typical.

4.1.6 EEL-6: Pearlite, HRC 38.5

Sample EEL-6 was transformed at 627°C to fine pearlite of HRC 38.5. The microstructure observed was similar to EEL-4 and EEL-5, but less fine again. The lamellar spacing observed was about 78 nm. Figures 4.1-13 and 14 are typical.

4.1.7 Tempered Martensite

Discs 36 and 37 were austenitized at 816°C, oil quenched and tempered at 510°C for 60 minutes, to obtain a tempered martensite of HRC 45-46. Discs 38 and 39 were tempered at 566°C, to HRC 43 and discs 40 and 41 were tempered at 616°C to HRC 38-39. For consistency with the notation used hitherto, i.e., EEL-1 to 6, undeformed samples of these quenched and tempered specimens were referred to as EEL-7 to 9. In this context, "undeformed" means any sample taken 1 mm or more below the wearing surface. Figures 4.1-15 to 20 show typical microstructures. Generally, as tempering temperature increased the carbides changed from predominantly acicular to

predominantly spheroidal, and the dislocation density decreased. The observed drop in hardness was associated with these changes.

4.2 Worn Samples

In this section we present micrographs and descriptions of the microstructures observed in the worn samples. The notation "RD" is used on many of the micrographs to indicate approximately the rolling direction or, more precisely, the trace of the rail surface. The direction of travel of the "train", i.e., rolling direction of the test discs, is in all cases approximately normal to the plane of the micrographs. Where selected area diffraction patterns are shown, the diameter of the selected area is indicated, e.g., "3.5 μm S.A." etc., to aid in obtaining a qualitative inpression of grain size. Thus, for example, a fine ring pattern with a 0.9 μm S.A. indicates a grain diameter much smaller than 0.9 μm, while a simple spot pattern would be obtained from grains whose diameter is similar to or larger than the diameter of the selected area. Also, in many instances, especially in samples taken near the running surface, the diffraction patterns indicate some degree of texture. A polycrystalline rail steel sample would be expected to give a ring diffraction pattern (assuming a S.A. diameter much larger than the grain size) showing Fe{110}, {200}, {211}, etc., reflections. The diameters of these rings are respectively proportional to $\sqrt{2}$, $\sqrt{4}$, $\sqrt{6}$, etc. Thus, if the {110} ring (diameter 9.85 nm^{-1}) is imaged with a diameter of 46 mm (typical in this report), then the {200} ring (13.9 nm^{-1}) and the {211} ring (17.1 nm^{-1}) will be imaged with diameters 65 mm and 80 mm, respectively.

Cementite reflections will be much weaker in strength, since the fraction of cementite is much less than that of ferrite. The strengths of the first three rings, as observed, would normally be roughly equal, with the {110} ring slightly brighter and the {211} slightly less bright than the {200}. A regular variation in brightness around the circumference of an otherwise smooth ring, or a significant deviation from the normal brightness of a ring indicates some degree of texture. A detailed study of textures was beyond the scope of this project (but see Section 5, Discussion, below).

4.2.1 Bainite, HRC 45 (Discs 32, 33 or E29LR, RR)

4.2.1.1 Low Rail

Typical micrographs of samples from disc 32 (E29LR) are shown in figures 4.2-1 to 4.2-4. Figure 4.2-1 shows that at 260 μm from the running surface, the microstructure is essentially that of the virgin material (compare figure 4.1-3). Figure 4.2-2 shows the microstructure at 220 μm. Again, the material seems essentially unchanged from the virgin material. Although the carbides are not continuous lamellae (as in good pearlite) an average spacing of about 80 - 100 nm can be measured on this micrograph, about the same as seen on the un-deformed material.

Figures 4.2-3 and 4 show the microstructures at 80 μm and 37 μm, respectively. By 37 μm, the spacing of the carbides has decreased to 40-60 nm, and both at 80 μm and 37 μm, there is a tendency for carbides to lie in the rolling plane. This tendency is quite absent at 260 μm. In no case does the dislocation density appear to be much different from that observed in the un-deformed material. However, the diffraction patterns are more informative: we

have gone from a grain size (as opposed to sub-grains) larger than 3.5 μm in diameter (figures 4.2-1, 2) to smaller than 3.5 μm, as shown by the incomplete rings which have replaced the simple spot patterns observed further from the surface.

4.2.1.2 High Rail

Typical micrographs of samples from disc 33 (E29RR) are shown in figures 4.2-5 to 4.2-12. Figures 4.2-5 and 4.2-6 show regions both at about 200 μm from the gage surface of the disc. Superficially, the bright-field images resemble the different regions of the original microstructure. However, the dark field images and especially the diffraction patterns show that there has been considerable deformation, leading to a striking grain refinement, and the development of a strong texture, as evidenced by the almost complete absence of the {200} diffraction rings. This absence of the {200} ring, in the presence of strong {110} and {211} rings, suggests a ⟨111⟩ wire texture (see section 5, Discussion). This texture was seen in virtually all heavily deformed regions of all samples. The individual grains which appear bright in the dark field image (figures 4.2-5c) are typical of the grain size of this deformed region.

Figures 4.2-7 show the same sample at about the same depth (170 μm) from the field corner of the rail. Here, the deformation has been much less severe, and the microstructure is not significantly different from that of the un-deformed material.

Figures 4.2-8 and 4.2-9 show the tread section of disc 33 at 60 μm from the surface. The microstructure seen in

figure 4.2-8a, inhomogeneous in comparison to pearlite, is still recognizable as bainite. However, there has been a refinement of the carbide structure, from the 80-100 nm spacing of the un-deformed material, to 30-50 nm, with occasional spacings to 10 nm observed. The relative widths of cementite and ferrite lamellae have remained essentially constant, showing that both phases have deformed. The diffraction pattern, figure 4.2-8b, shows grain refinement, and suggests that texture is beginning to develop. Figures 4.2-9a and 4.2-9b show the microstructure at higher magnification. The dislocation density is very high, but not significantly higher than in the original material (compare figure 4.1-4). This suggests that there has been deformation of the ferrite with respect to the cementite, so that dislocations responsible for ferrite deformation have passed completely through individual ferrite lamellae, to disappear at the ferrite/cementite interfaces. Note also sub-surface cracks (most likely somewhat enlarged by electropolishing) in figures 4.2-8a and 4.2-9a. When such cracks were observed, they were always parallel to the sample surface, and always in regions where the microstructure had been rolled parallel to this surface. However, they might occur in either the coarser bainitic microstructure or the finer, almost pearlitic, microstructure.

Figures 4.2-10 to 4.2-12 show the microstructures developed at 34 μm, 24 μm and 14 μm, respectively, below the tread surface. The most striking feature of this sequence of micrographs is the continuing refinement of the grain size, together with the development of texture. Note that the diffraction patterns, figures 4.2-11b and 4.2-12b, correspond to a selected area of only 0.9 μm diameter.

4.2.2 Bainite, HRC 42 (Discs 8, 7 or E16LR, RR)

4.2.2.1 Low Rail

Typical micrographs of samples from disc 8 (E16LR) are shown in figures 4.2-13 to 4.2-16.

Figures 4.2-13a and 4.2-13b show that the microstructure at 240 μm below the gage surface is essentially unchanged from the original microstructure. Figures 4.2-14 and 4.2-15 show how the microstructure refines progressively as the running surface is approached, the carbides become parallel to the surface, the carbide spacing and grain size become finer, and texture develops. The carbide spacing remains less fine than that observed in the corresponding regions of disc 32, being never less than about 20 nm, and usually more. In any case, the carbides in bainite are not regular lamellae and the "spacing" is not clearly defined. Finally, figure 4.2-16 shows an incipient crack developing by the void-formation and coalescence process.

4.2.2.2 High Rail

Typical micrographs of samples from disc 7 (E16RR) are shown in figures 4.2-17 to 4.2-23. Figures 4.2-17 to 4.2-19 show that at 640 μm and 300 μm below the surface, and at the field corner even as close to the surface as 40 μm, there is substantially no deformation evident. However, at 2 mm from the gage corner, i.e., between "gage" and "tread" sections, at 58 μm we see definite signs of deformation, in the form of refinement of the carbide spacing, and in the development of a finer grain structure. This continues until the surface is reached (figures 4.2-22, 23). The diffraction pattern of figure 4.2-22b again shows texture, probably more well defined than the ⟨111⟩ texture suggested above. However, of all the foils

prepared during the course of this study, only one permitted good micrographs to be taken from the sample surface, and it would therefore be premature to attempt to describe the texture more precisely at this time. This diffraction pattern also implies a very fine grain size, and this is illustrated graphically in figure 4.2-23, where grains as small as about 15 nm in diameter, and ranging up to 40 nm wide by 550 nm long are shown.

4.2.3 Bainite, HRC 37 (Discs 30, 31 or E30LR, RR)

4.2.3.1 Low Rail

Typical micrographs of samples from disc 30 are shown in figures 4.2-24 and 4.2-25. As described in section 3 above, certain samples presented difficulties in final thinning for TEM examination, due generally to the presence of relatively more frequent small sub-surface cracks. This sample was one of these.

The observations we have of disc 30 are consistent with those of other foils. At 250 μm no deformation is observable in the electron micrographs. At 90 μm, even at the field side, some deformation is apparant, observable most easily as tangential streaking in diffraction spots. This indicates the division of grains into sub-grains, which precedes the development of fine grains.

4.2.3.2 High Rail

Typical micrographs of samples from disc 31 are shown in figures 4.2-26 to 4.2-33. They again show increasing deformation, evidenced by the development of a fine grain size and of texture, on approaching the wearing surface or,

at a given depth, moving from the field to the gage side of the rail. Note in figures 4.2-27, as in figures 4.2-8 and others, the mixture of fine and coarse microstructure, deriving from the original bainitic structure.

4.2.4 Transitional Pearlite, HRC 43-44, (Discs 28, 29 or E35RR, LR)

As was the case with disc 30, both high-rail and low-rail specimens of transitional pearlite presented difficulty in TEM sample preparation, as described in section 3 above. The crack shown in figure 3-4 is typical of the difficulty encountered.

4.2.4.1 Low Rail

Although disc 29 is in fact transitional pearlite, the regions observed in this tested sample more nearly resemble upper bainite. Figures 4.2-34 to 4.2-36 show the microstructures developed at depths of 550 μm, 110 μm and 70 μm in this disc. Again, the polygonization and grain refinement increase as the wearing surface is approached, so that figure 4.2-34 at 550 μm shows little evidence of deformation, and a nearly single-crystal diffraction pattern, while at 70 μm polygonization is evident.

4.2.4.2 High Rail

Figures 4.2-37 show little evidence of deformation of the high rail disc 28 at a depth of 100 μm from the field surface, other than a somewhat higher dislocation density than that seen in the un-tested sample. Due to sample preparation difficulties, no other micrographs are available from this sample.

4.2.5 Fine Pearlite, HRC 42. (Discs 19 and 20, or E34LR, RR)

4.2.5.1 Low Rail

Figures 4.2-38 to 40 show the microstructures developed in disc 19 at depths of 110 μm, 12 μm and 6 μm below the field surface. At 110 μm (figures 4.2-38) the microstructure is indistinguishable from the un-tested material. At 12 μm, however, the ferrite has become fine-grained and the dislocation density has increased substantially. At 6 μm from the surface, the grain refinement is even more pronounced. Note that the diffraction pattern (figure 4.2-40b) does not show any strong texture.

4.2.5.2 High Rail

Figures 4.2-41 to 43 show the microstructure developed in disc 20, at depths of 130 μm, 75 μm and 30 μm below the tread surface. Again, the diffraction pattern gives the clearest evidence of the development of a very fine polycrystalline grain structure. The bright field micrographs also show that both ferrite and cementite have deformed. For example, Figure 4.2-43 shows pearlite spacings as fine as 20 nm - 30 nm, without broken cementite, which is to be compared to the 70 nm average spacing observed in the new material.

4.2.6 Pearlite, HRC 38.5. Discs 14 and 15, or E33LR, RR.

It was generally observed that deformation was most severe at the gage corners and least at the field. Also, deformation was most severe nearest the wear surface, as expected. Thus, certain of the micrographs presented in this section are apparently anomalous (4.2-49, 4.2-55) and suggest that a certain amount of sample inhomogeneity is present. However, the general pattern observed on other specimens is still apparent.

4.2.6.1 Low Rail

Figures 4.2-44 to 48 show observations on disc 14. The only sign of deformation at 300 μm (Figure 4.2-44) is the clustering or piling up of dislocations against the reinforcing cementite (compare the clean cementite/ferrite boundaries of figures 4.1-13 and 14). Figure 4.2-46, in contrast, shows a microstructure no longer recognizable as pearlite. The diffraction pattern, Figure 4.2-46b, shows that the structure is extremely fine grained polycrystal, and is comparable to figure 4.2-22b.

Figures 4.2-47 and 48 show the gage corner of the same disc at 30 μm and 72 μm below the surface. The diffraction patterns show that the deformation here is greater than that beneath the tread section at similar depths (e.g., compare figures 4.2-47b and 4.2-45b).

4.2.6.2 High Rail

Figures 4.2-49 to 51 show microstructures observed in disc 15. Even more than the observations on disc 14, the observations on this disc seem inconsistent with those of other worn discs and among themselves, in that Figure 4.2-49, (disc 15, 140 μm below tread) shows more deformation

than either Figure 4.2-50 (55 μm below tread surface) or figure 4.2-51 (10 μm below tread surface). In any case, however, what we see to be the more significant features are still present, i.e., the deformation leads to polygonization of the ferrite (Figure 4.2-49b) and the cementite acts as a re-inforcing constituent, so that dislocations in the ferrite pile up at ferrite/ cementite boundaries, leading ultimately to work hardening of the ferrite and rotation of ferrite blocks between cementite laths (Figures 4.2-44, 49, 50).

4.2.7 Tempered Martensite, HRC 45-46. Discs 36 and 37 or E38LR, RR.

4.2.7.1 Low Rail

Micrographs 4.2-52 to 4.2-55 show the microstructures developed in disc 36. Although Figure 4.2-55 shows less deformation than expected, the micrographs show a generally increasing level of deformation as the surface is approached, and a superficial similarity to pearlite or bainite, in that the deformation leads to the formation of elongated cells, with cementite at the boundaries. These cells are in fact polycrystalline grains. This is particularly evident in Figure 4.2-54.

4.2.7.2 High Rail

Micrographs 4.2-56 to 4.2-59 show the microstructure developed in disc 37 at depths of 150 μm, 90 μm and 75 μm below the tread surface, and 50 μm below the gage surface. The microstructures at 150 μm and 90 μm are superficially similar to that of the undeformed material. However, the diffraction patterns obtained from undeformed material, with a 3.5 μm selected area, were similar to single crystal patterns, i.e., simple spot patterns, while the patterns for the deformed material are clearly polycrystalline already at 150 μm, and show grain refinement as the wearing surface is approached. It is interesting that figure 4.2-59b shows much less texture than other ring diffraction patterns obtained. While other ring patterns not showing texture were obtained, these seem the exception rather than the rule, in the tempered martensite samples as in the bainitic and pearlitic steels examined.

4.2.8 Tempered Martensite, HRC43, Discs 38 and 39 or E39LR, RR

4.2.8.1 Low Rail

Figures 4.2-60 to 62 show the microstructures developed in disc 38 at 20 μm and 35 μm below the tread surface and 130 μm below the field surface. Again, we note the development of a fine grain size and texture. Superficially, the microstructures at 20 μm and, to a lesser degree at 35 μm resemble the bainitic and pearlitic steels. This is a result of the elongated grains produced by the deformation, with the carbides tending to lie on the grain boundaries. Closer inspection, however, reveals that the carbides remain separate in the deformed tempered martensite, and continuous in the deformed pearlite, so that to this extent the original microstructure is preserved.

4.2.8.2 High Rail

Micrographs 4.2-63 and 64 show the microstructures developed in disc 39 at 35 μm below the field surface, and at 180 μm. The number of successful samples of this specimen was not as great as would be desirable, due to difficulty with electroplating. Specifically, difficulty was experienced in cleaning the specimens, and a successful plating was not obtained at the gage or tread surfaces. Still, the results obtained are consistent with other observations. Grain refinement is again observed near the surface, although here, at the field corner, the deformation even at 35 μm has been insufficient to develop texture. Figures 4.2-63b and 4.2-63c illustrate the use of different selected areas in evaluating grain sizes: the 3.5 μm S.A. pattern is polycrystalline, while the 0.9 μm S.A. of figure 4.2-63c shows only a single grain.

4.2.9 Tempered Martensite, HRC38-39. Discs 40 and 41 or E40 LR and RR

4.2.9.1 Low Rail

Figures 4.2-65 to 67 show how the microstructure of disc 40 evolves from nearly equiaxed grains with a limited range of orientations over a 3.5 μm diameter, at 260 μm below the wearing surface to an array of elongated grains, showing a highly polygonal and somewhat textured structure at 10 μm from the surface. In these elongated grains, one sees the cementite arranged along the grain boundaries, forming a microstructure superficially resembling pearlite (compare also figures 4.2-54 and 4.2-50). However, the carbides along grain boundaries are not continuous in the deformed tempered martensite, as they are (nearly) in the pearlite.

4.2.9.2 High Rail

Figures 4.2-68 to 71 show the microstructures developed in disc 41. They are quite similar to those seen in disc 40, but the grain size is not quite as fine, as judged from the diffraction patterns. Figure 4.2-71 shows the tendency to produce elongated grains particularly well.

4.2.10 Bainite with Martensite. Discs 11 and 12 or E17RR, LR

The main interest in these discs was to investigate the effect of martensite particles in the bainitic matrix, to decide whether such particles might be harmful.

The difficulty in obtaining samples just at the wearing surface, referred to in section 3, was multiplied by an order of magnitude when seeking the effect of martensite particles, since the martensite was present only as a minor constituent, and of interest only at or very near the wearing surface. As a result, only one good sample showing the effect of martensite particles was obtained. No good sample was obtained from disc 11.

4.2.10.1 Low Rail, Disc 12

Figures 4.2-72 to 78 show microstructure developed at and near martensite particles. Figure 4.2-72 gives a low magnification view of the area examined, which was centered about 160 μm below the field surface of the sample. Figure 4.2-73 shows the region, between two martensite particles, which was examined in detail. The sketch, Figure 4.2-74 identifies areas from which high magnification micrographs were taken. Figure 4.2-78 shows the heavily twinned microstructure of the martensite particle. The general impression is as of laminar flow of a fluid (the bainitic matrix) past obstacles (the martensite). Following the analogy, the microstructure developed in the regions of more rapid flow is finer and finer grained than that in the backwater regions. Also, even at some distance from the immediate vicinity of the martensite, there seems to be a refinement of the microstructure. Thus, the microstructure of Figure 4.2-77, about 20 μm from any martensite particles, shows a finer grain size than a comparable

area of disc 31, with the same bainitic structure but no martensite (compare figure 4.2-29).

5. DISCUSSION

5.1 Identification of Texture

Body centered cubic crystals such as iron give electron (or X-ray) diffraction lines or spots corresponding to planes {h k ℓ} such that (h + k + ℓ) = 2n where n is any integer, 0, 1, 2, 3, etc. Thus, diffraction is permitted from planes {110}, {200}, {211} , etc. In 100 kV transmission electron diffraction, diffraction rings from {110}, {200} and {211} are all bright. Higher order rings become significantly weaker as the value of $(h^2 + k^2 + \ell^2)$ increases. In the present study, however, many of the diffraction patterns from regions very near to the running surface showed missing or anomalously weak {200} rings, with {100} and {211} rings at normal intensities. Since the Bragg angle for diffraction of 100 kV electrons is very small (of the order of 0.01 rad or 0.5^{o}), we observe diffraction essentially from planes belonging to zones whose zone axes are parallel to the electron beam. Thus, to explain missing {200} rings together with strong {100} and {211} rings, we conclude that the foil normal, very nearly the rolling direction or direction of train travel in this case, is a direction or zone axis perpendicular (or very nearly perpendicular) to {110} and to {211}, but far from perpendicular to {200}. Thus, the observation of weak or missing {200} rings in diffraction patterns suggests ⟨111⟩ wire texture. Further observation, especially of sections perpendicular to that observed, would establish the texture more precisely. Automated X-ray equipment would yield still more reliable results with less effort, although the relatively small size of the test discs may present problems. No difficulties should be encountered with full size rail samples.

5.2 Comparison of Microstructures

Inoue et al. (7) observed that cementite in pearlite, deformed in tension, slips on (100) and on (001), at room temperature and at 300°C. At 400°C and above, slip was observed also on (010) and on certain {110} planes. Embury and Fisher (8) and Langford (9) studied pearlite highly deformed by wire drawing. As in the present work, it was found that the deformation led to a considerable refinement of the pearlite, with significant deformation and little fragmentation of the cementite. Thus, one must conclude that under these conditions (wire drawing or simulated rail service) glide planes other than (100) and (001), most likely also (010) and {110}, must operate in cementite. Systems involving only (100) and (001) would not be sufficient to permit the observed ductility of cementite.

The correlation of flow stress with pearlite spacing, for both the data of Embury and Fisher and of Langford, fitted a Hall-Petch type of relationship.

$$\sigma = \sigma_o + k\, d^{-\frac{1}{2}} \quad . \quad . \quad . \quad . \quad . \qquad 5.1$$

where d is the pearlite spacing or slip distance in the ferrite. The relationship may be re-stated in terms of the amount of strain, as

$$\sigma = \sigma_o + \frac{k}{\sqrt{2 r_o}} \exp\left(\frac{\varepsilon}{4}\right) \quad . \quad . \qquad 5.2$$

where r_o is the initial pearlite spacing, and ε the true strain. Embury and Fisher found that the same result held for upper Bainite and for pure iron, where d in the Hall-Petch relation was the width of narrow elongated grains which formed on deformation. Enbury and Fisher

state that the grains or "slab like cells" of ferrite which developed on deformation had relative misorientations of about 1^{o}. In this respect, their observations differ from ours, in that in the present work the observed cells were grains of quite different orientations, leading to the polycrystalline diffraction patterns shown. Neither Embury and Fisher nor Langford show diffraction patterns. However, we also observe a significant hardening, up to about 700 KHN, close to the surface, associated with a refinement of the microstructure, as well as the polygonization and texture development.

Langford observes that where cementite is discontinuous, the average spacing (d, in the Hall-Petch relation 5.1) is increased, and hence the expected flow stress is decreased. Such discontinuities could arise from some fragmentation of the cementite as in Langford's work, or because the cementite was not continuous to begin with, as in the present case when dealing with Bainite or tempered martensite. That is, the pearlite develops an effectively finer structure, with a smaller slip distance, d, than does either the Bainite or tempered martensite. We would therefore expect to observe higher near-surface hardness in the pearlite than in the bainite, and less hardening still in the tempered martensite.

In this manner, the more continuous cementite of the pearlite would explain its superior wear performance. While microhardness measurements did not fall directly within the scope of the present investigation, a few traverses were done and reported in our Interim Report No. 4. Among them, we found for disc 14 (pearlite, low rail, initial hardness HRC 38.5) a maximum near-surface hardness of nearly 700 KHN. For disc 6 (bainite, low rail, initial hardness HRC 42), the maximum near surface

hardness developed was about KHN 400, lending support to the hypothesis. The improved performance of fine pearlite, say, compared to coarser pearlite, would be due to the r_o dependance in equation 5.2, assuming similar strains to be observed in both cases. However, the effect of strain is predominant.

5.3 Effect of Martensite Particles

The observed effect of martensite particles in the matrix is to concentrate the strain in the regions between particles. Thus, to the extent that increased strain eventually leads to failure, as in delamination near the wear surface, the presence of martensite particles must be considered to be deleterious.

6. APPENDIX

6.1 Sample Codes

It was found convenient to refer to all samples, which had received similar heat treatments, by a similar code. Thus, up to three different codes might be used to refer to a given sample. These are summarized in Table 6.1

6.2 Principles of Image Formation in the TEM

Consider Figure 6.1. The specimen is supposed to be illuminated by a parallel beam of electrons, itself parallel to the optic axis of the instrument. Some of these electrons pass undeviated through the sample, and others are diffracted, as from the set of atomic planes sketched. Both of these transmitted beams are still parallel, the undeviated beam being still parallel to the optic axis, and the diffracted beam making an angle 2θ with the optic axis. Two points are now essential to bear in mind:

1) Both parallel beams come to foci in the back focal plane of the objective lens. The undeviated beam is focused to a point on the optic axis, (at the origin of the vector labelled "r") while the diffracted beam is brought to a focus a distance $|r|$ from the optic axis. In fact, since 2θ is in reality a very small angle, of the order of 0.5^{o} - 1^{o}, we have to a very good approximation:

$$r = (2\theta) f$$

where f is the focal length of the objective lens.

2) All rays (beams of electrons) originating from or passing through a point on the specimen are focused at the conjugate point on the "intermediate image"

TABLE 6.1

Equivalent Sample Codes

CODE						
TUNS	CANMET	NRC Vancouver	Transformation Temperature °C	Time, Minutes	Hardness HRC	Microstructure
EEL-1	EEL-1	-	385		45	Upper Bainite
2	2	-	415		42	" " "
3	3	-	460		38	" " "
4	4	-	570		44.5	Transitional Pearlite
5	5	-	595		42	Fine Pearlite
6	6	-	627		38.5	Pearlite
EEL-1	32, 33	E29LR, RR	385	50	45	Upper Bainite
2	7, 8	E16RR, LR	415	40	42	Upper Bainite
3J	11, 12	E17RR, LR	460	45		Upper Bainite with martensite
4	28, 29	E35RR, LR	575	45	43-44	Transitional Pearlite
5	19, 20	E34LR, RR	595	35		Pearlite
6	14, 15	E33LR, RR	627	30		Pearlite
2	34, 35	E31LR, RR	415	80	42	Upper Bainite
3	30, 31	E30LR, RR	460	90	37	Upper Bainite
7	36, 37	E38LR, RR	510*	60	45-46	Tempered martensite
8	38, 39	E39LR, RR	566*	60	43	Tempered martensite
9	40, 41	E40LR, RR	616*	60	38-39	Tempered martensite

* These samples were austenitized at 816°C, oil-quenched and tempered 60 minutes at the indicated temperature.

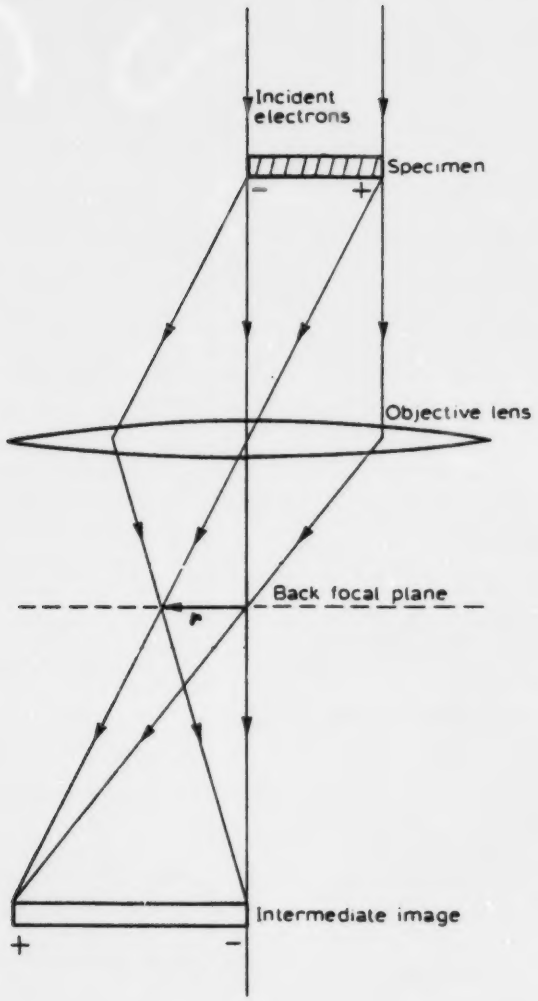

FIGURE 6.1: Schematic ray diagram illustrating the formation of a diffraction pattern and an intermediate image by the objective lens of an electron microscope (adapted from Head et al. (6)).

in the image plane of the objective lens. Thus, both the undeviated and the diffracted rays from the point "+" on the specimens are focused at the conjugate point "+" on the image. The image can be constructed wholly from a bundle or pencil of rays parallel to the optic axis, or from a pencil of diffracted rays, or (with a good lens!) from both together as indicated in the diagram.

The electron microscope consists essentially of a source of parallel electrons (gun and condenser lenses), the objective lens, and two or more lenses after the objective (three in the Philips EM 300, four in the EM 400). These lenses may be controlled so that they project on to a viewing screen or photographic film either

a) a magnified image of the spot pattern in the back focal plans of the objective lens or

b) a magnified image of the intermediate image in the image plane of the objective lens.

Image (a) is the diffraction pattern of the sample, and image (b) is the image of the sample.

If an aperture be placed in the back focal plane of the objective lens, so that only the electrons focused at the optic axis may pass, while those focussed at points such as "r" are stopped, the resulting image will be bright where the sample is such that it does not diffract strongly, and dark in regions corresponding to parts of the sample which diffract (or scatter) electrons strongly, so that these scattered electrons are lost from the undeviated beam. This is the "bright field" image.

Alternatively, if an aperture be placed in the back focal plane so that the diffracted electrons pass while the undeviated electrons are stopped, we obtain a "dark field" image. Now, those regions of the sample which diffract into the selected beam are imaged brightly. In a specific case, these might be small grains in a polycrystalline sample.

Next, consider an aperture in the plane of the intermediate image, of such a size that only electrons contributing to that part of the image between the points "+" and "-" may pass, while electrons contributing to any part of the image lying beyond these limits are intercepted. That is, electrons leaving the specimen from any point outside the indicated region ("+" to "-") would be intercepted, and not contribute to an ultimate final image. The aperture is in fact the field limiting aperture common to ordinary metallurgical microscopes. If now the lenses after the objective lens are focussed to project a diffraction pattern on to the viewing screen or film, then only those diffraction spots formed by electrons which have passed through the selected area of the specimen (between + and -) will be imaged. Other electrons, although they may pass through the same points in the back focal plane of the objective lens, are intercepted by the field limiting aperture, before they can be collected by the final lenses. Thus, the use of a field limiting aperture permits the technique known as "selected area diffraction".

The magnification of the final image is an easily understood concept, by analogy with the operation of an ordinary microscope. The "Magnification" of the diffraction pattern has a slightly different interpretation. Let the

distance "r" be magnified to a value "R" on the screen, as though the pattern had been formed by a single lens of focal length L. Then,

$$R = (2\theta)\, L$$

Now, for the small angles of interest here, Bragg's law becomes

$$\lambda = 2d\theta$$

or,

$$2\theta = \lambda d^{-1}$$

where "λ" is the wavelength of the electrons (3.7 pm or 0.037 $\mathring{A}$) and "d" is the separation of the planes diffracting the electrons. Then

$$R = (L\lambda)\, d^{-1}$$

That is, distances R measured on the diffraction pattern represent reciprocals of atomic plane separations in the sample. The quantity ($L\lambda$), known as the "camera constant" of the electron microscope is in effect the magnification of the diffraction pattern. All the diffraction patterns in this report have been presented at a magnification such that 23 mm represents 5 nm^{-1}.

7. REFERENCES

1. Kalousek, J., "Development of a 1/8 scale disc-on-disc rail/wheel wear testing facility", Can. Met. Q. 21, 67-72, 1982.

2. Charest, M., "La préparation de lames minces de divers aciers étudiés par microscopie électronique", PMRL Report MRP/PMRL-79-45 (TR), CANMET, Ottawa, 1979.

3. Hirsch, P.B., A. Howie, R.B. Nicholson, D.W. Pashley and M.J. Whelan, "Electron microscopy of thin crystals", Butterworths, London, 1965.

4. Agar, A.W., R.H. Alderson and D. Chescoe, "Principles and practice of electron microscope operation", North Holland, Amsterdam/Elsevier, New York, 1974.

5. Edington, J.W., "Practical electron microscopy in materials science", Van Nostrand Reinhold Co., New York, 1976.

6. Head, A.K., P. Humble, L.M. Clarebrough, A.J. Morton and C.T. Forwood, "Computed electron micrographs and defect identification", North Holland, Amsterdam, 1973.

7. Inoue, A., T. Ogura and T. Masumoto, "Microstructures of deformation and fracture of cementite in pearlitic carbon steels strained at various temperatures", Met. Trans. A., 8A, 1689-1695, 1977.

8. Embury, J.D. and Fisher, R.M., "The structure and properties of drawn pearlite", Acta Met. 14, 147-159, 1966.

9. Langford, G., "Deformation of pearlite", Met. Trans. A., 861-875, 1977.

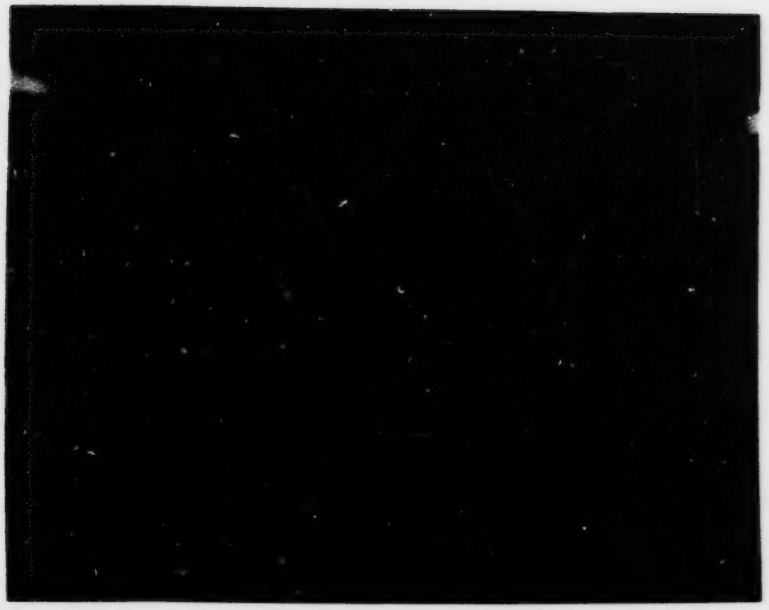

0.5μm

FIGURE 3-2: Disc 12, 250 μm below surface. Electropolished. 50 000 X. (Neg. 1835)

0.25μm

FIGURE 3-3: Same sample as shown in Figure 3-2, after subsequent ion thinning. 100 000 X. (Neg. 1881)

0.1mm

FIGURE 3-4: Disc 19 . Optical micrograph, showing premature perforation at sub-surface microcracks. 220X

0.5 μm

FIGURE 4.1-1. EEL-1. Upper Bainite. Lath microstructure. 50 000 X (Neg. 1157)

0.5 μm

FIGURE 4.1-2. EEL-1. Upper Bainite. High density of carbide-decorated dislocations. 60 000 X (Neg. 1162)

1 μm

FIGURE 4.1-3. EEL-1. Upper Bainite. Sub grains and high dislocation density. 25 000 X (Neg. 1159)

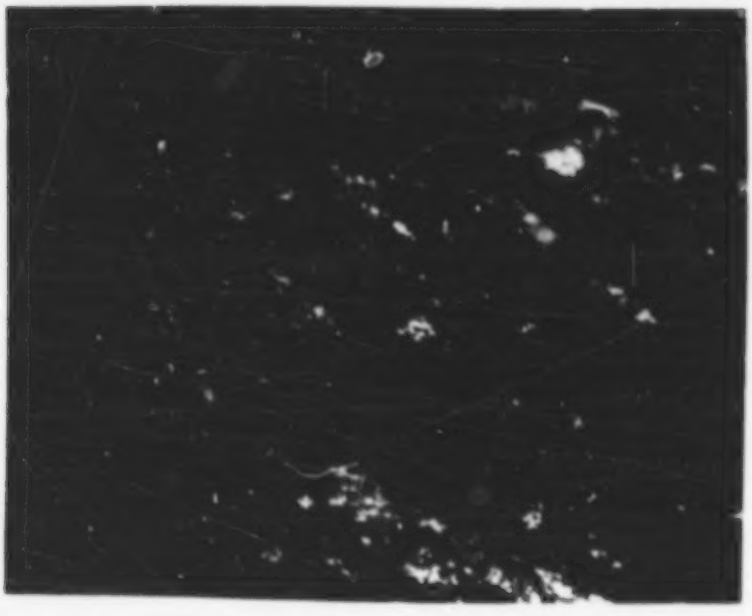

0.5 μm

FIGURE 4.1-4. EEL-1. Upper Bainite, As figure 4.1-3. 60 000 X (Neg. 1161)

0.5 μm

FIGURE 4.1-5. EEL-2 Upper Bainite. Compare sub-grain structure with figure 4.1-3. 50 000 X (Neg. 1116)

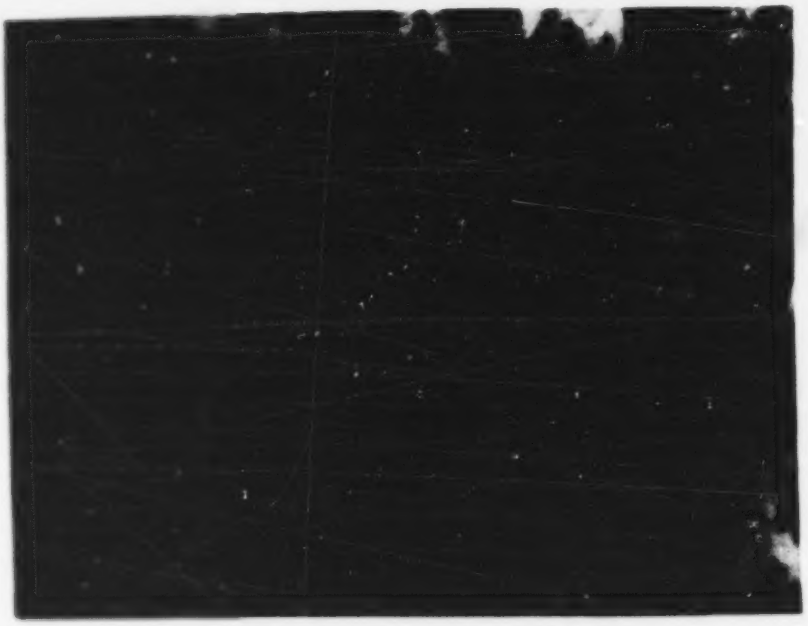

0.5 μm

FIGURE 4.1-6. EEL-2 Upper Bainite. Typical Region showing high dislocation density. 50 000 X. (Neg. 1187)

FIGURE 4.1-7. EEL-3. Upper Bainite, transformed at 460°. Compare figures 4.1-2 and 6. 50 000 X. (Neg. 1092)

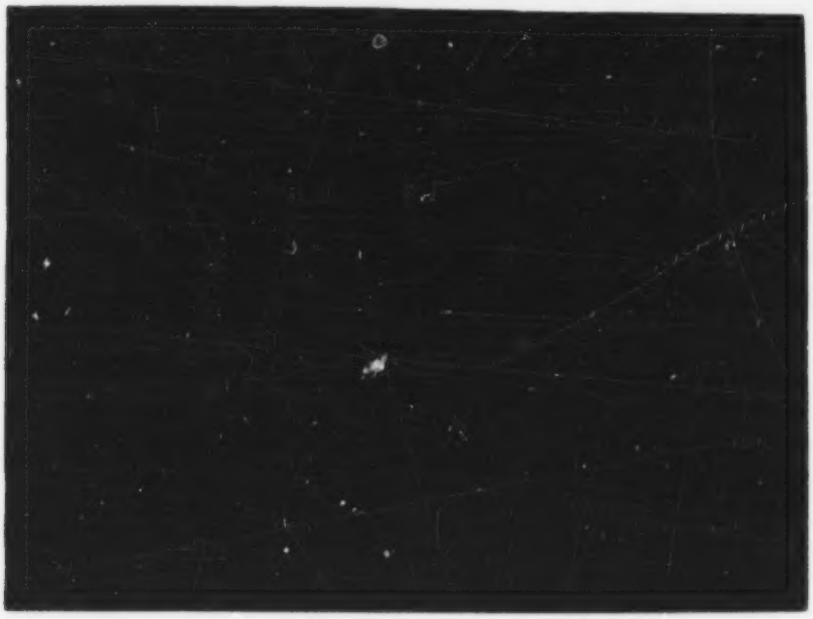

FIGURE 4.1-8. EEL-3 Upper Bainite, transformed at 460°C. 50 000 X. (Neg. 1055)

0.5μm

FIGURE 4.1-9. EEL-4. Transitional Pearlite. 50 000 X. (Neg. 1065)

0.5μm

FIGURE 4.1-10. EEL-4. Transitional Pearlite. 50 000 X. (Neg. 1072)

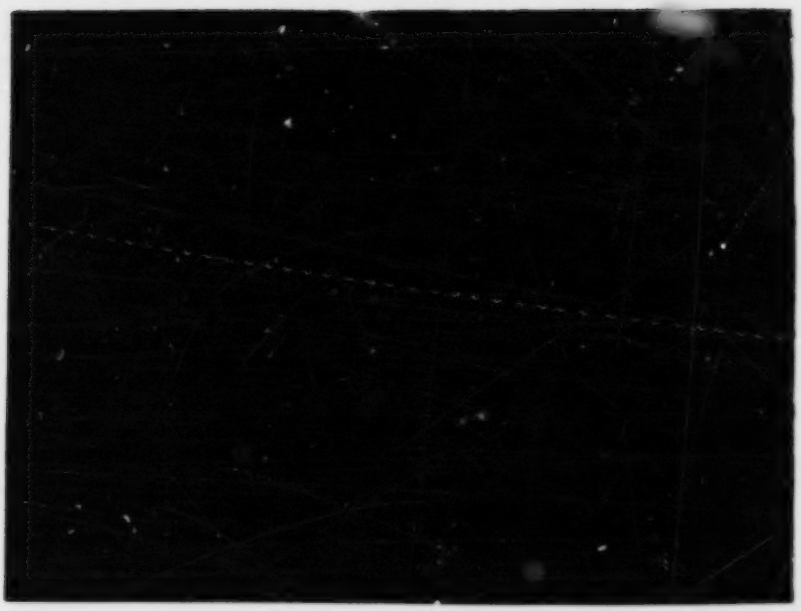

FIGURE 4.1-11. EEL-5. Fine pearlite. 100 000 X. (Neg. 1013)

FIGURE 4.1-12. EEL-5. Fine pearlite. High dislocation density is atypical. 100 000 X. (Neg. 1020)

FIGURE 4.1-13. EEL-6. Fine pearlite. 50 000 X. (Neg. 1123)

FIGURE 4.1-14. EEL-6. Fine pearlite. 50 000 X. (Neg. 1133).

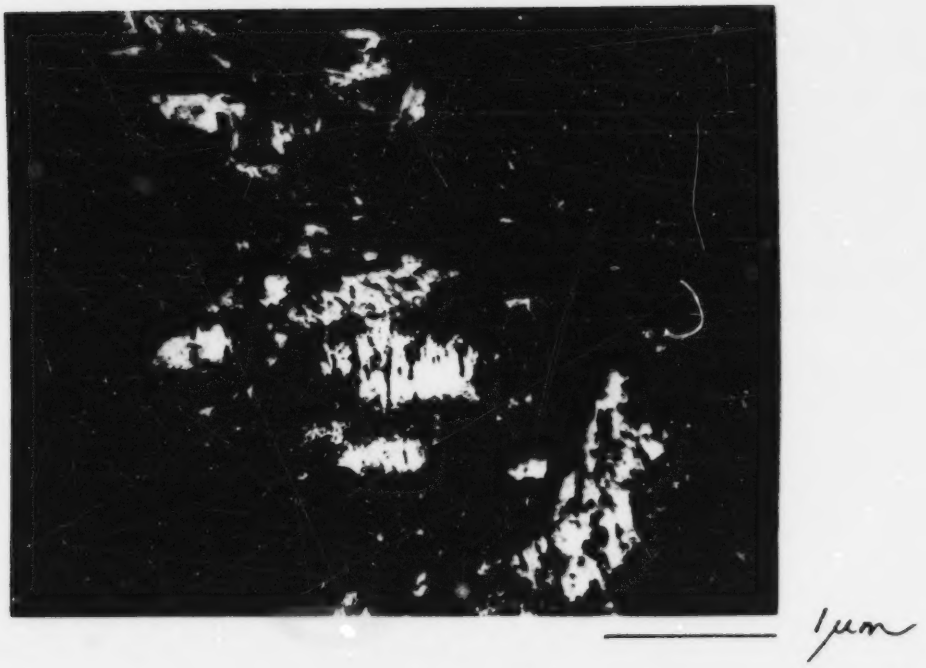

FIGURE 4.1-15. EEL-7. Tempered at 510°C. 25 000 X. (Neg. 2224)

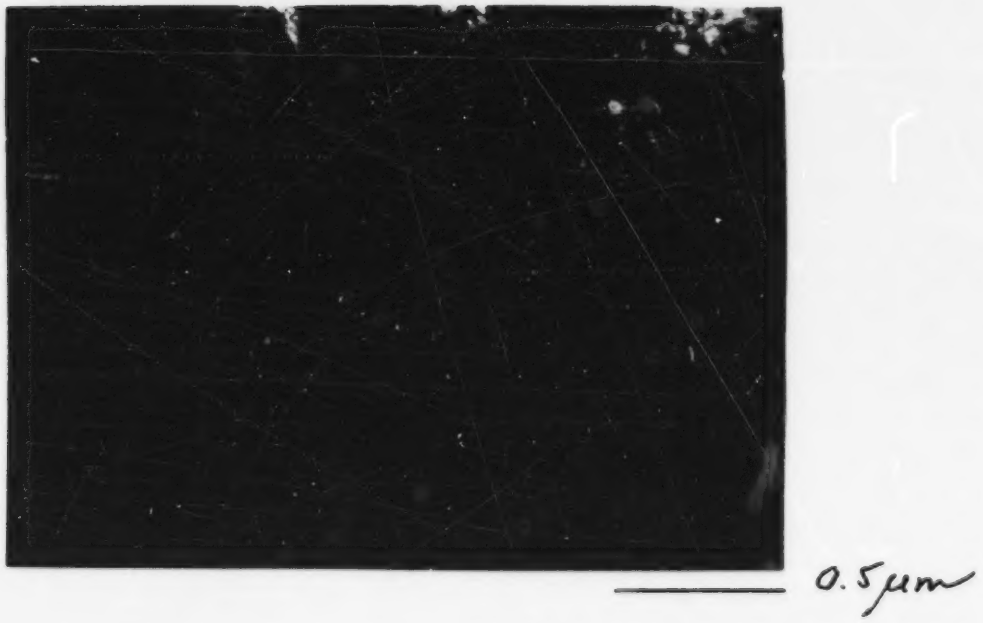

FIGURE 4.1-16. EEL-7. Tempered at 510°C. 50 000 X. (Neg. 2152)

FIGURE 4.1-17. EEL-8. Tempered at 566°C. 25 000 X. (Neg. 2192)

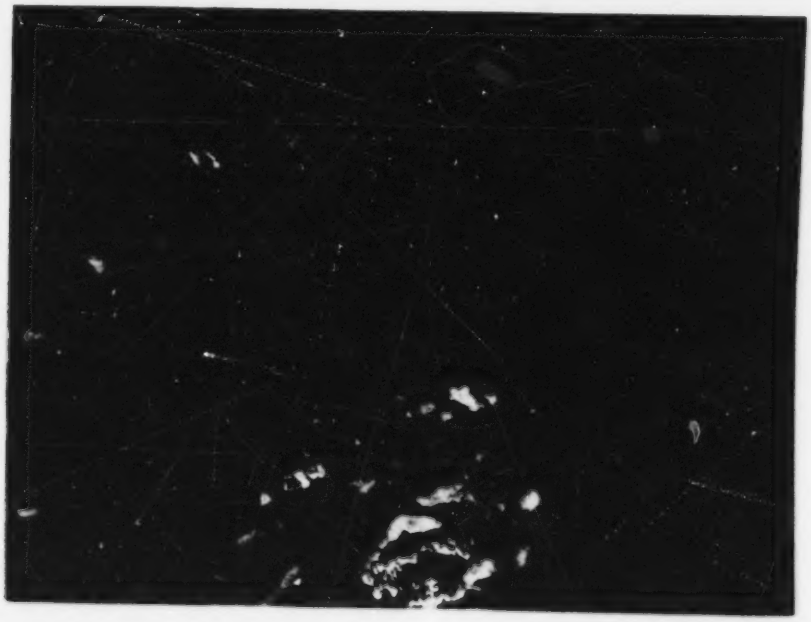

FIGURE 4.1-18. EEL-8. Tempered at 566°C. Part of figure 4.1-17. 50 000 X. (Neg. 2194)

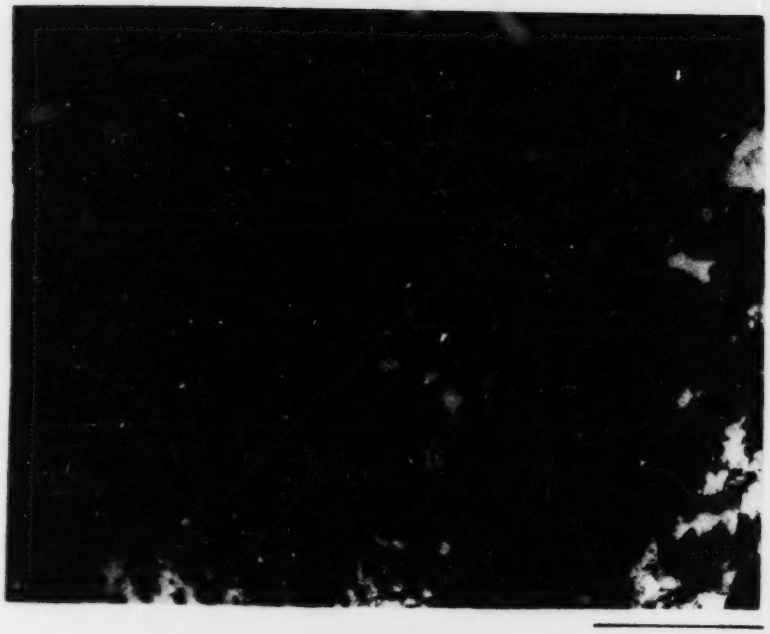

FIGURE 4.1-19. EEL-9. Tempered at 616°C. 25 000 X. (Neg. 2290)

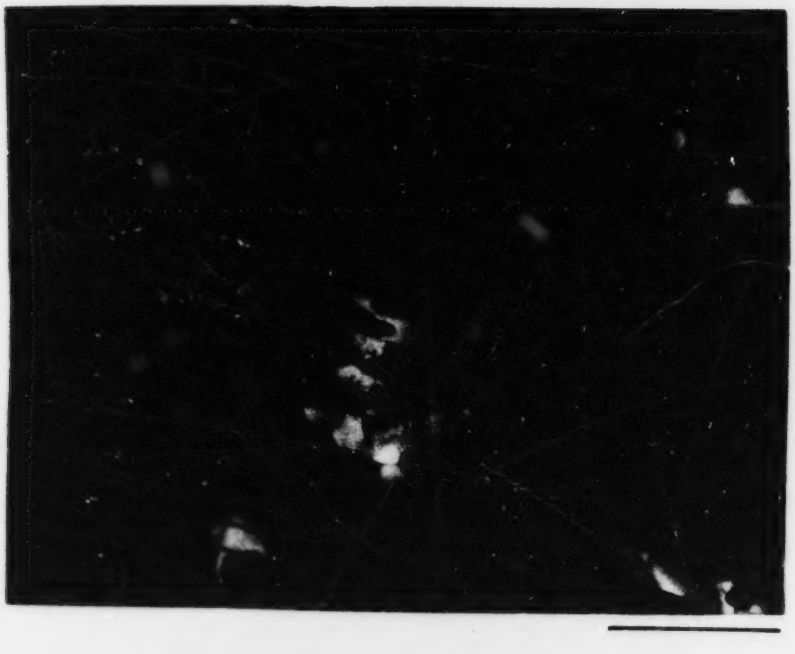

FIGURE 4.1-20. EEL-9. Tempered at 616°C. 50 000 X. (Neg. 2285)

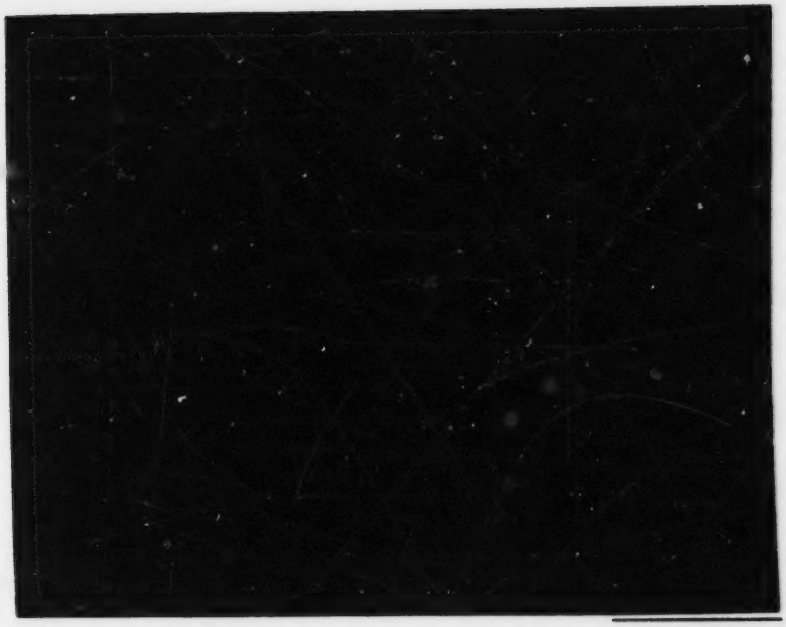

FIGURE 4.2-1a: Disc 32, 260 μm from tread surface, 25 000 X. Compare Figure 4.1-3 (Neg. 2235)

FIGURE 4.2-1b: Diffraction pattern corresponding to central portion of Figure 4.2-1a. 3.5 μm S.A. (Neg. 2236).

FIGURE 4.2-2a: Disc 32, 220 μm from tread surface, 25 000 X. (Neg. 2237)

FIGURE 4.2-2b: Diffraction pattern corresponding to central portion of Figure 4.2-2a. 3.5 μm S.A. (Neg. 2238)

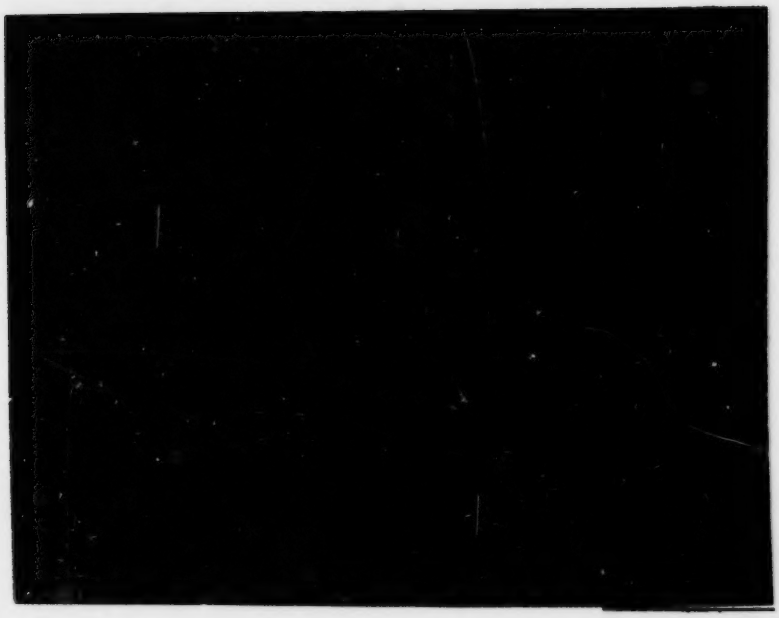

FIGURE 4.2-3a: Disc 32, 80 μm from tread surface, 50 000 X. (Neg. 1988)

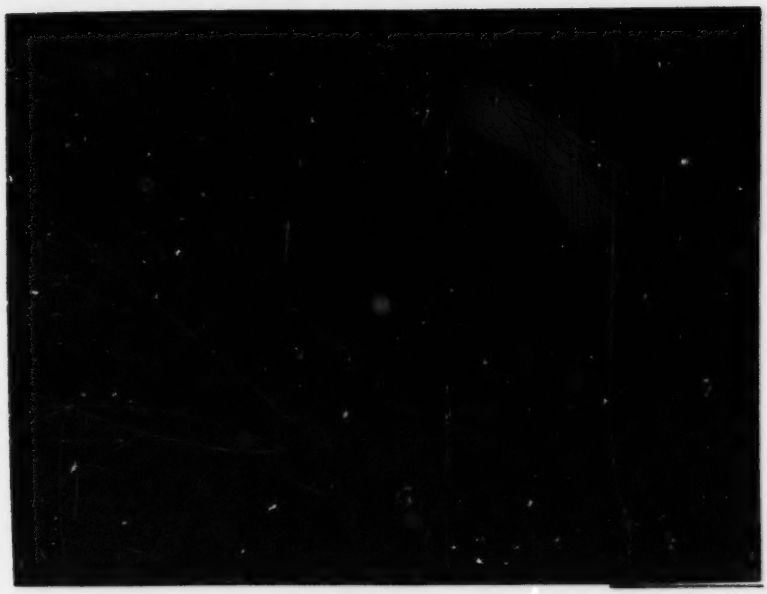

FIGURE 4.2-3b: Diffraction pattern corresponding to Figure 4.2-3a. 3.5 μm S.A. (Neg. 1989)

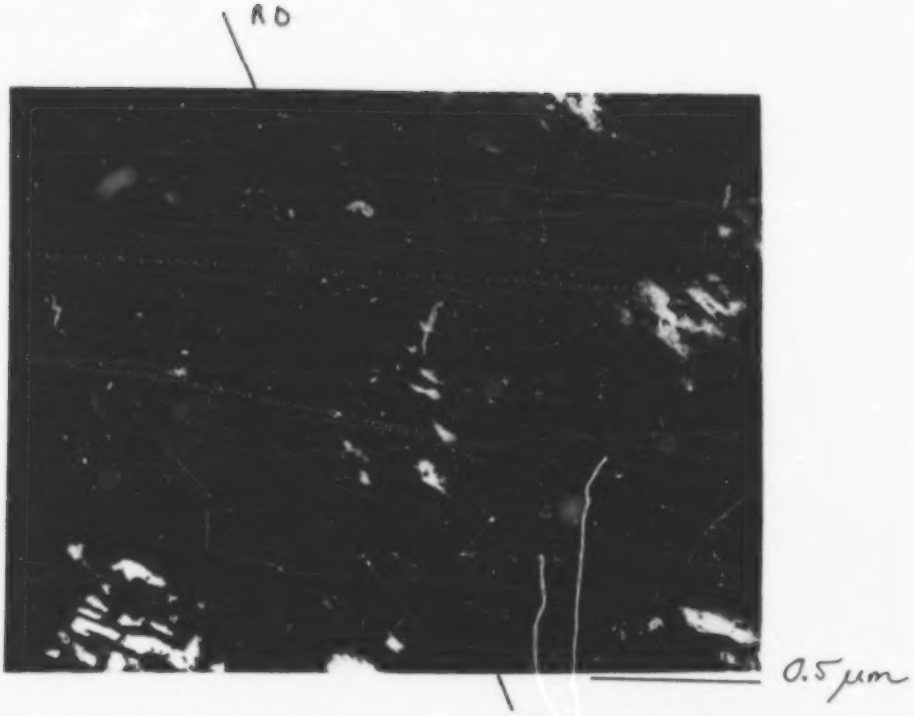

FIGURE 4.2-4a: Disc 32, 37 µm from tread surface. 50 000 X. (Neg. 2239).

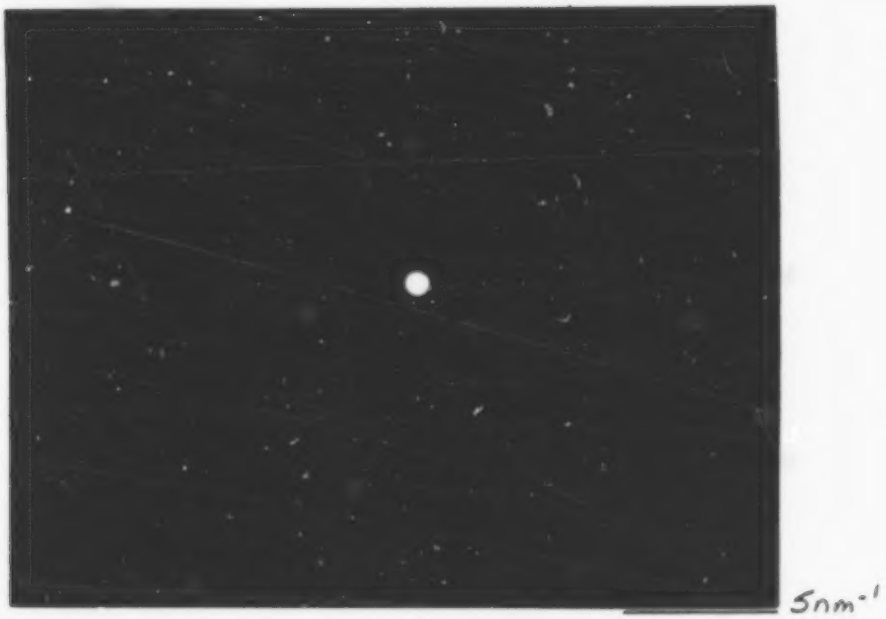

FIGURE 4.2-4b: Diffraction pattern corresponding to Figure 4.2-4a. 3.5 µm S.A. (Neg. 2240)

FIGURE 4.2-5a: Disc 33, 200 μm from gage surface. 50 000 X. (Neg. 1808)

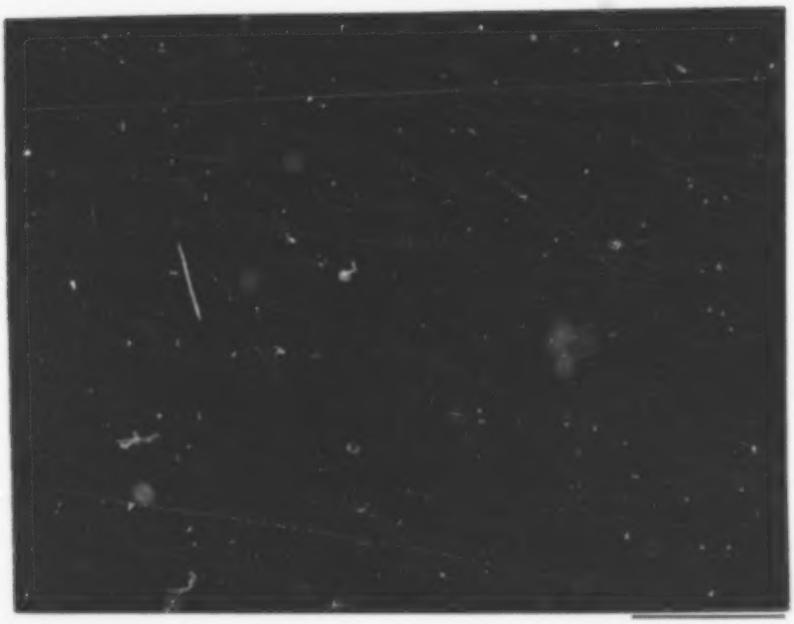

FIGURE 4.2-5b: Diffraction pattern corresponding to Figure 4.2-5a. 3.5 μm S.A. (Neg. 1810)

FIGURE 4.2-5c: Dark field image corresponding to Figure 4.2-5a. {110} reflection. (Neg. 1811)

FIGURE 4.2-6a: Disc 33, 200 μm from gage surface. 50 000 X. (Neg. 1812)

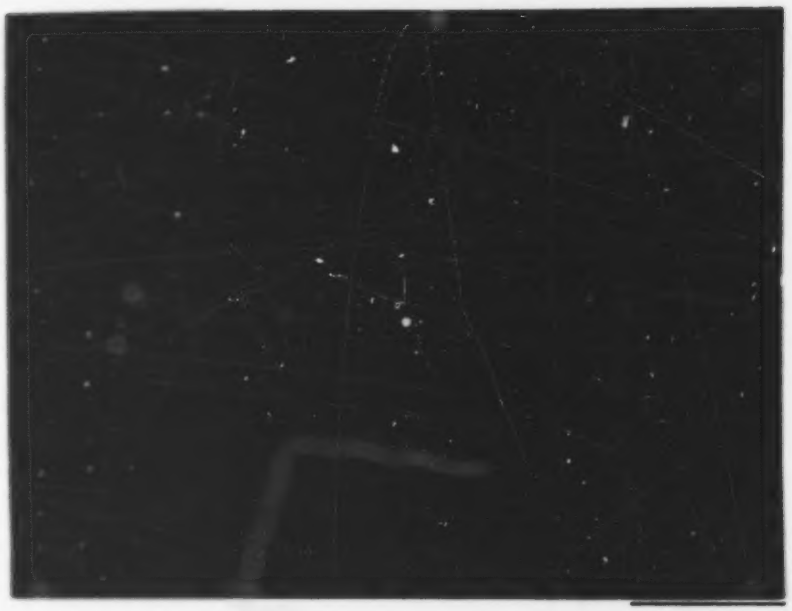

FIGURE 4.6-6b: Diffraction pattern corresponding to Figure 4.2-6a. 3.5 μm S.A. (Neg. 1813)

FIGURE 4.2-6c: Dark field image corresponding to Figure 4.2-6a. {110} reflection. (Neg. 1814)

FIGURE 4.2-7a: Disc 33, 170 μm from field surface. 25 000 X. (Neg. 1779)

FIGURE 4.2-7b: Diffraction pattern corresponding to central portion of Figure 4.2-7a. 3.5 μm S.A. (Neg. 1780)

FIGURE 4.2-8a: Disc 33, 60 μm from tread surface. 25 000 X. (Neg. 1794)

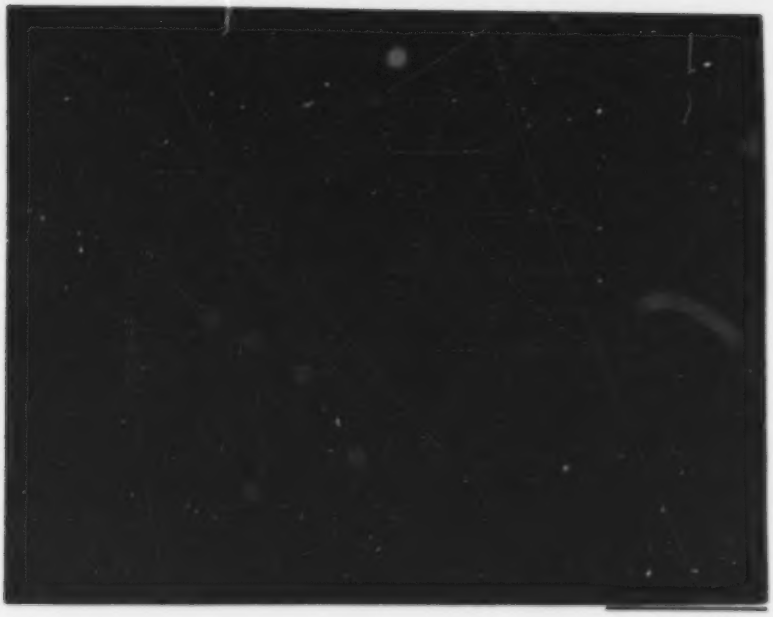

FIGURE 4.2-8b: Diffraction pattern corresponding to central region of Figure 4.2-8a. 3.5 μm S.A. (Neg. 1803)

FIGURE 4.2-9a: Disc 33, 60 µm from tread surface. 75 000 X. (Neg. 1822)

FIGURE 4.2-9b: Disc 33, 60 µm from tread surface. 75 000 X. (Neg. 1823).

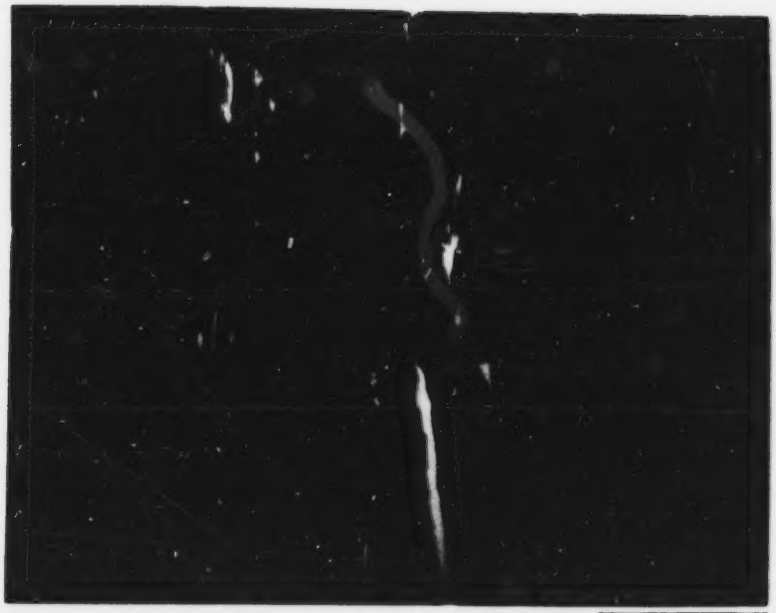

FIGURE 4.2-10a: Disc 33, 34 μm from tread surface, 25 000 X. (Neg. 1790)

FIGURE 4.2-10b: Diffraction pattern corresponding to Figure 4.2-10a. 3.5 μm S.A. (Neg. 1789)

FIGURE 4.2-11a: Disc 33, 24 μm below tread surface. 100 000 X. (Neg. 1805)

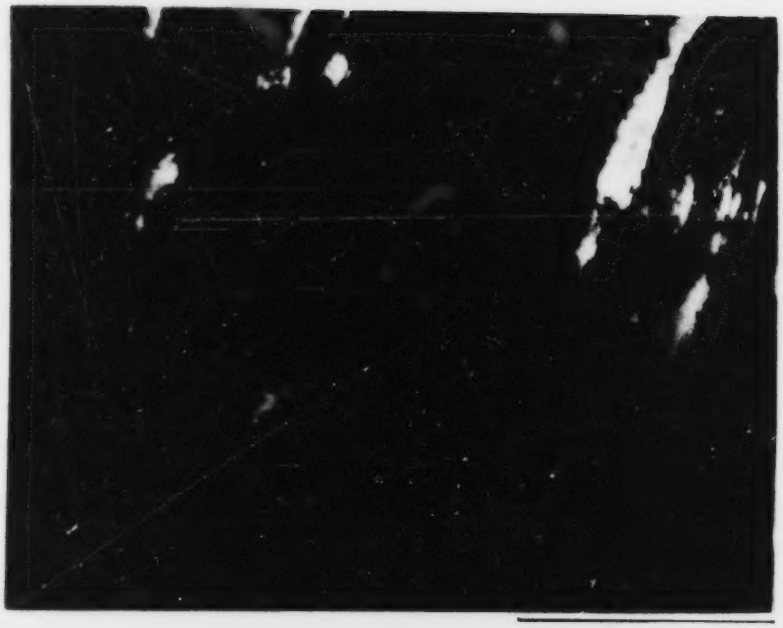

FIGURE 4.2-12a: Disc 33, 14 μm below tread surface. 75 000 X. (Neg. 1786).

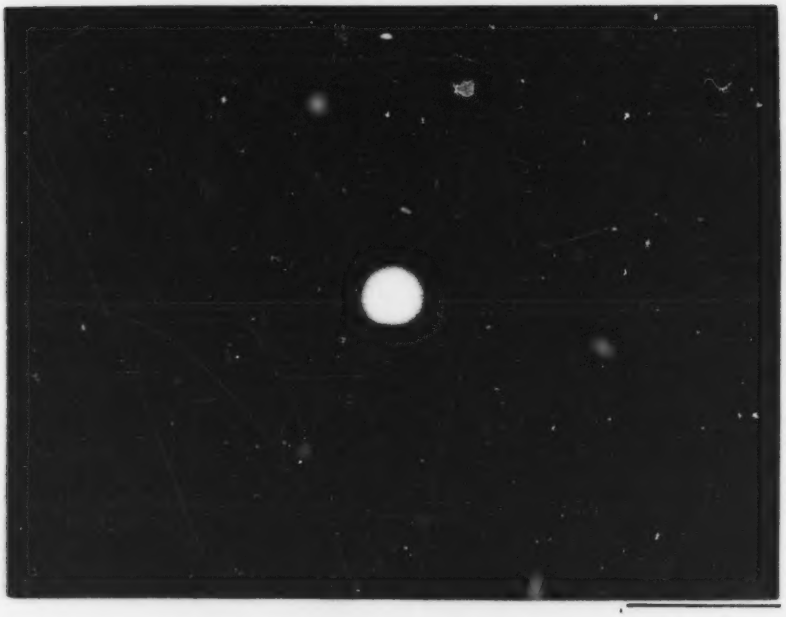

FIGURE 4.2-12b: Diffraction pattern corresponding to central region of Figure 4.2-12a. 0.9 μm S.A. (Neg. 1787).

FIGURE 4.2-13a: Disc 8, 240 μm below gage surface. 50 000 X (Neg. 1272)

FIGURE 4.2-13b: Diffraction pattern corresponding to central portion of Figure 4.2-13a. (Neg. 1273)

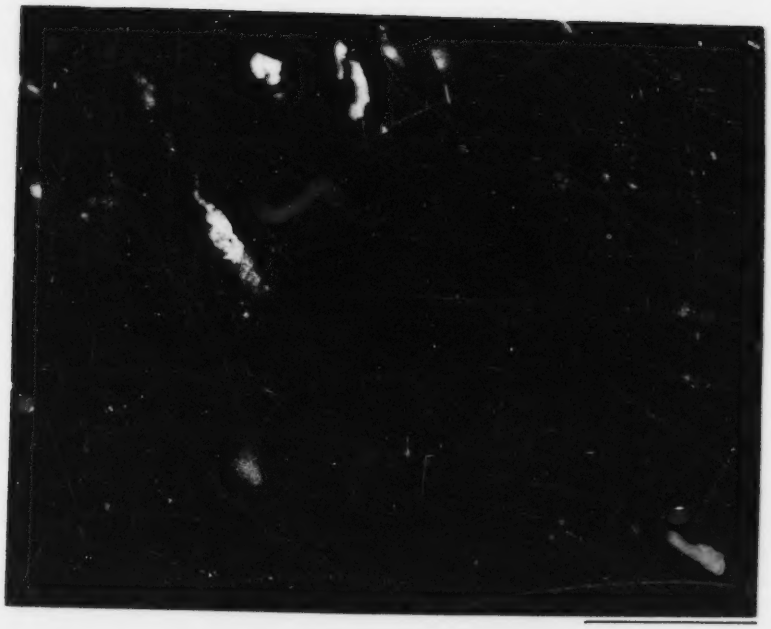

FIGURE: 4.2-14a: Disc 8, approximately 35 μm below gage surface. 50 000 X. (Neg. 1870)

FIGURE 4.2-14b: Diffraction pattern corresponding to Figure 4.2-14a. 3.5 μm S.A. (Neg. 1873).

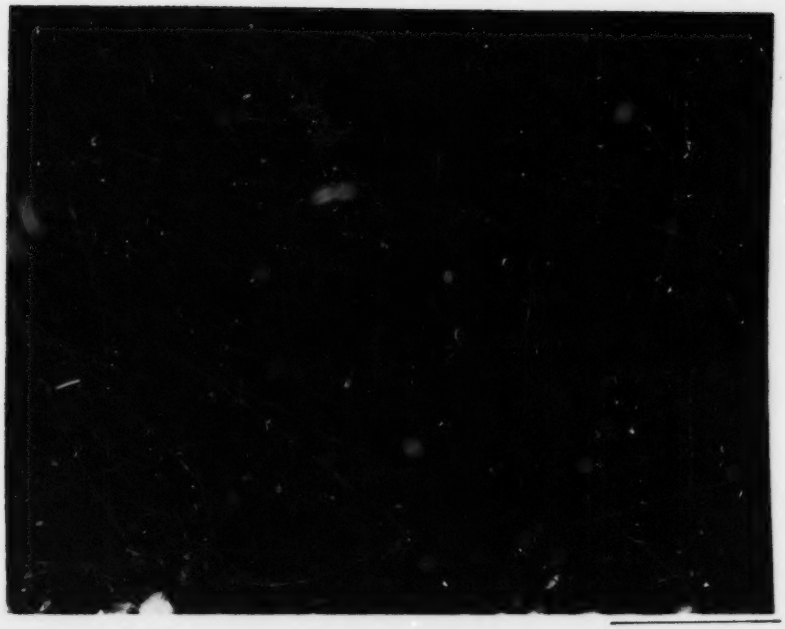

FIGURE 4.2-15a: Disc 8, approximately 8 μm below field surface. 50 000 X. (Neg. 1855)

FIGURE 4.2-15b: Diffraction pattern corresponding to central portion of Figure 4.2-15a. 0.9 μm S.A. (Neg. 1856).

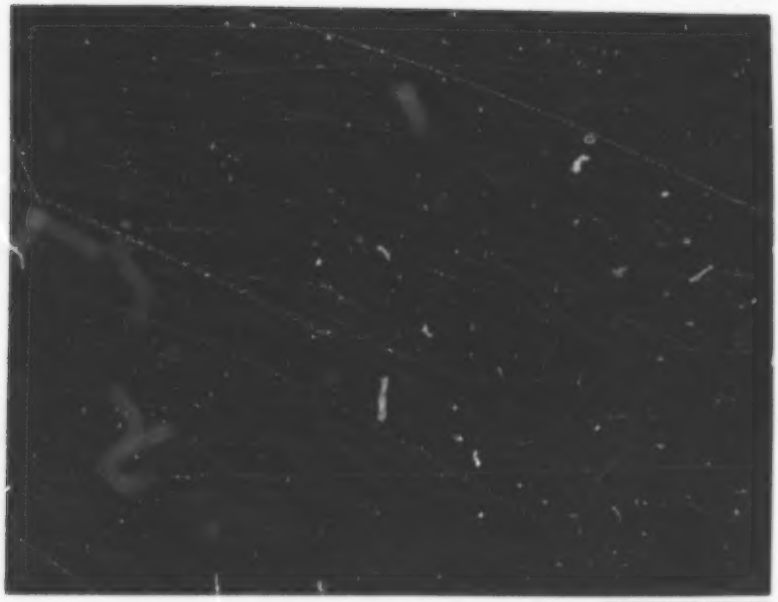

FIGURE 4.2-15c: Dark field image corresponding to Figure 4.2-15a. {100} reflection. (Neg. 1858)

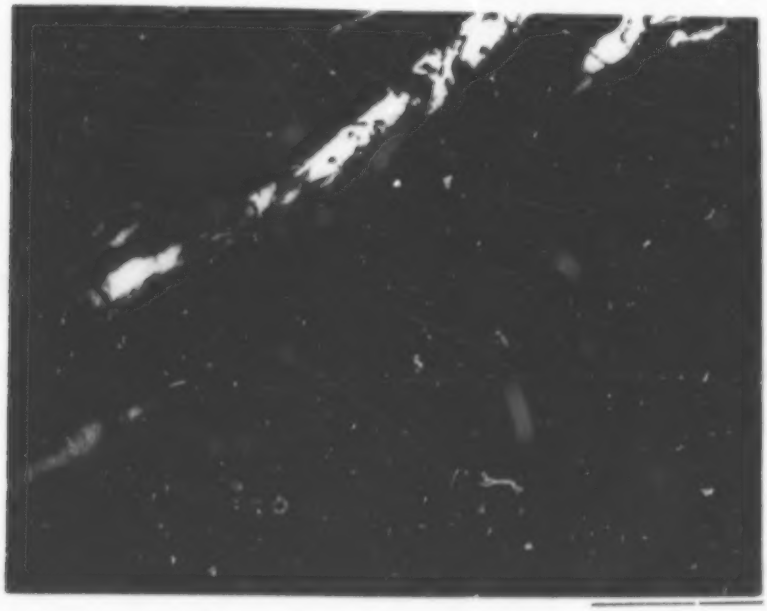

FIGURE 4.2-16: Disc **5**, approximately 8 μm below field surface, showing incipient crack. 50 000 X. (Neg. 1861)

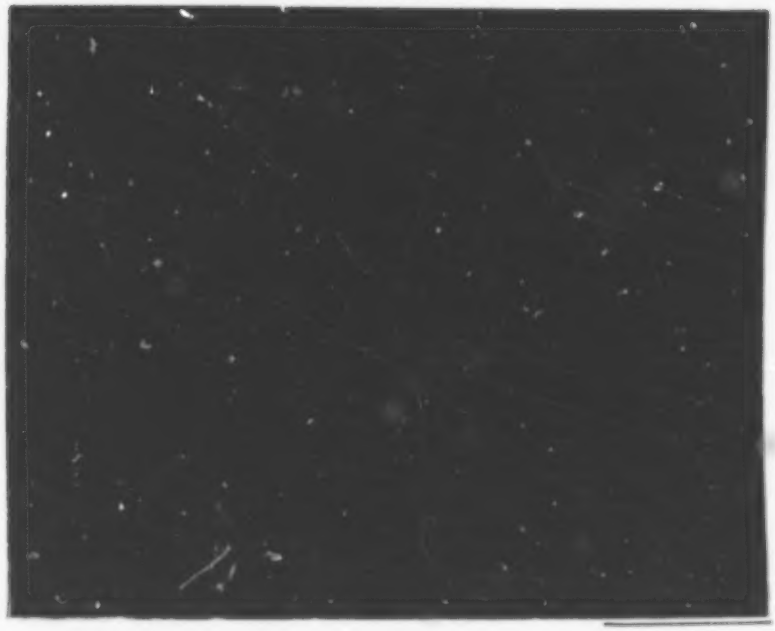

FIGURE 4.2-17: Disc 7, 640 μm below field surface. 50 000 X (Neg. 1532)

FIGURE 4.2-18: Disc 7, 300 μm below field surface. 100 000 X (Neg. 1364).

FIGURE 4.2-19a: Disc 7, 40 μm below field surface. 75 000 X (Neg. 1561)

FIGURE 4.2-19b: Diffraction pattern corresponding to central portion of Figure 4.2-19a. 0.9 μm S.A. (Neg. 1562)

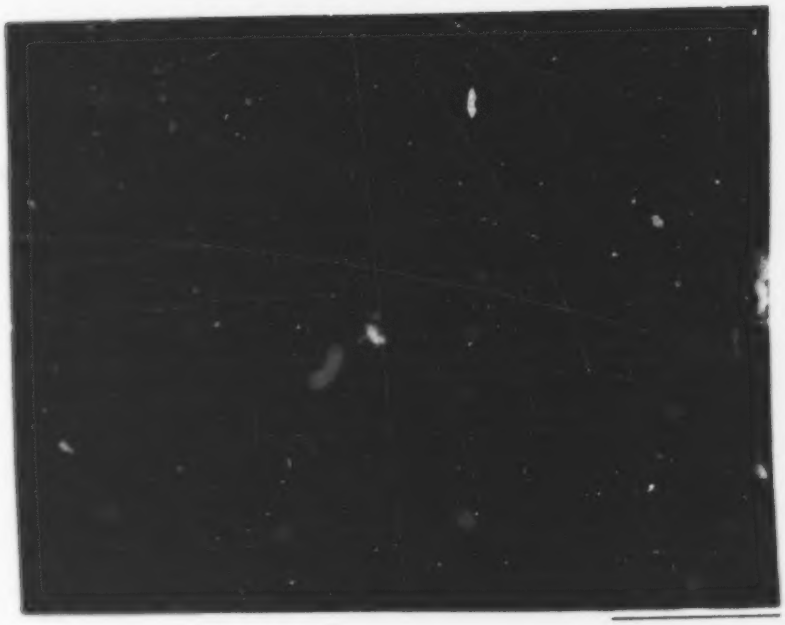

FIGURE: 4.2-20a: Disc 7, 58 μm below surface, 2 mm from gage corner. 100 000 X. (Neg. 1556)

FIGURE 4.2-20b: Diffraction pattern corresponding to Figure 4.2-20a. 0.9 μm S.A. (Neg. 1557)

FIGURE 4.2-21a: Disc 7, 30 μm below surface, 2 mm from gage corner. 100 000 X. (Neg. 1548)

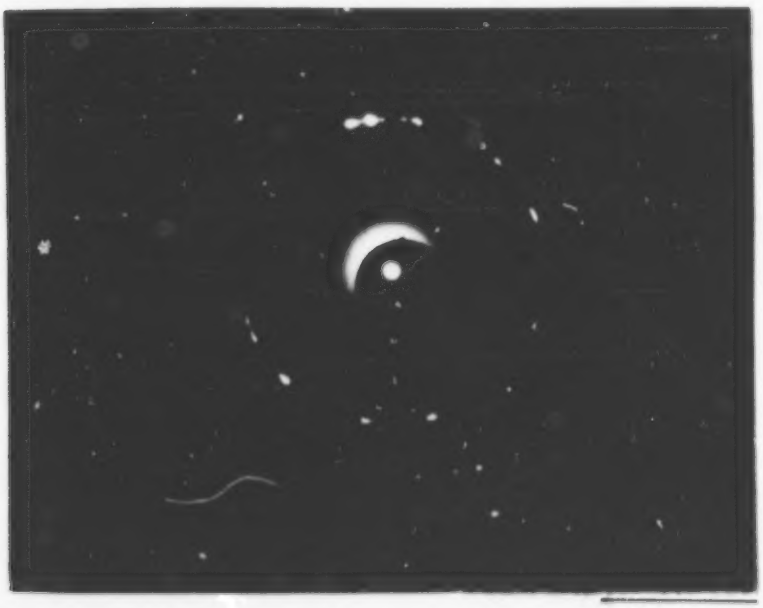

FIGURE 4.2-21b: Diffraction pattern corresponding to Figure 4.2-21a. 0.9 μm S.A. (Neg. 1550)

FIGURE 4.2-22a: Disc 7, at surface, 2 mm from gage corner. 50 000 X. (Neg. 1543)

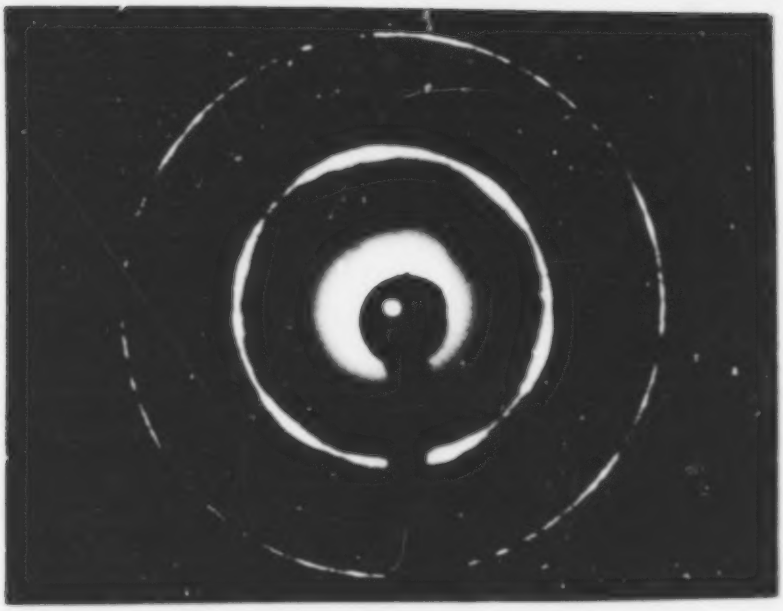

FIGURE 4.2-22b: Diffraction pattern of surface region of Figure 4.2-22a. 0.9 μm S.A. (Neg. 1537)

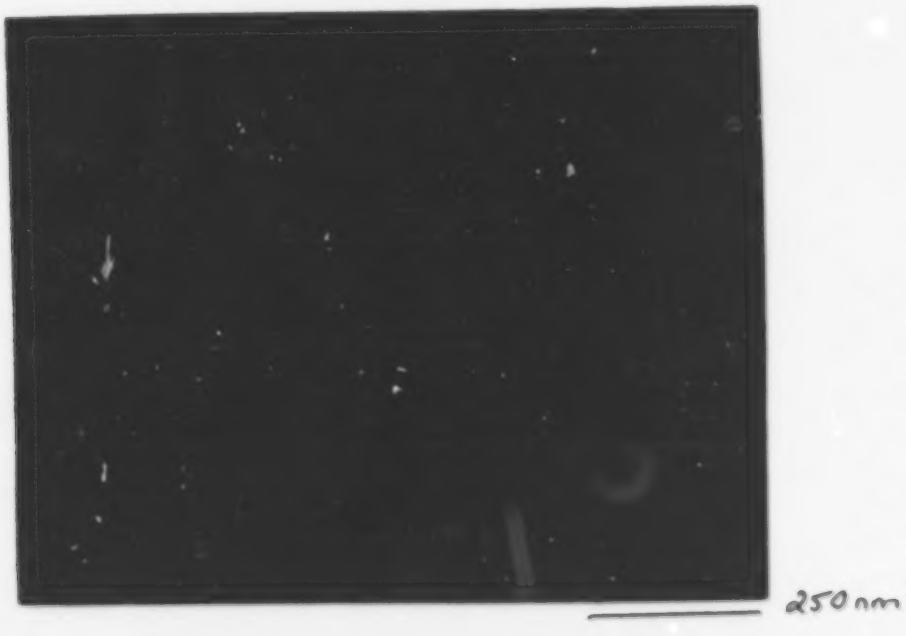

FIGURE 4.2-23: Dark field micrograph of part of Figure 4.2-22a. 100 000 X. (Neg. 1542).

FIGURE 4.2-24: Disc 30, 250 μm below tread surface.
50 000 X (Neg. 2349)

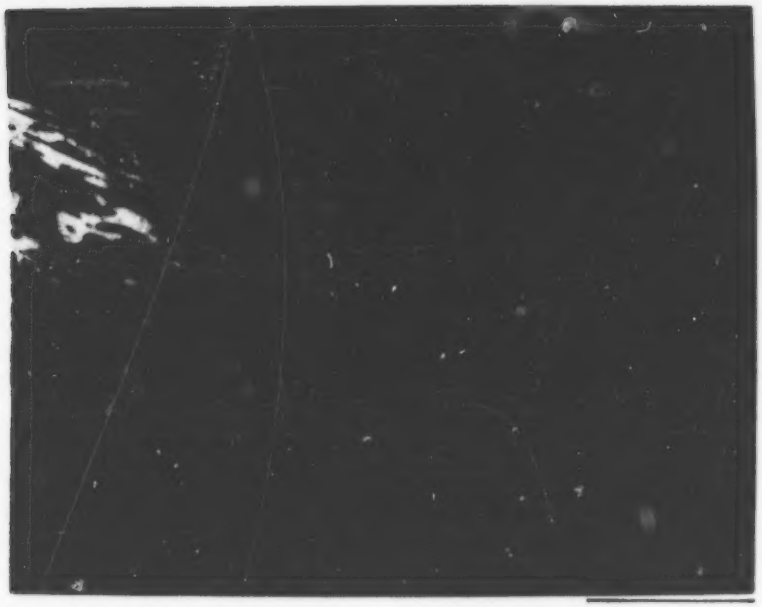

FIGURE 4.2-25a: Disc 30, 90 μm below field surface. 50 000 X (Neg. 2351).

FIGURE 4.2-25b: Diffraction pattern corresponding to Figure 4.2-25a. 3.5 μm S.A. (Neg. 2352)

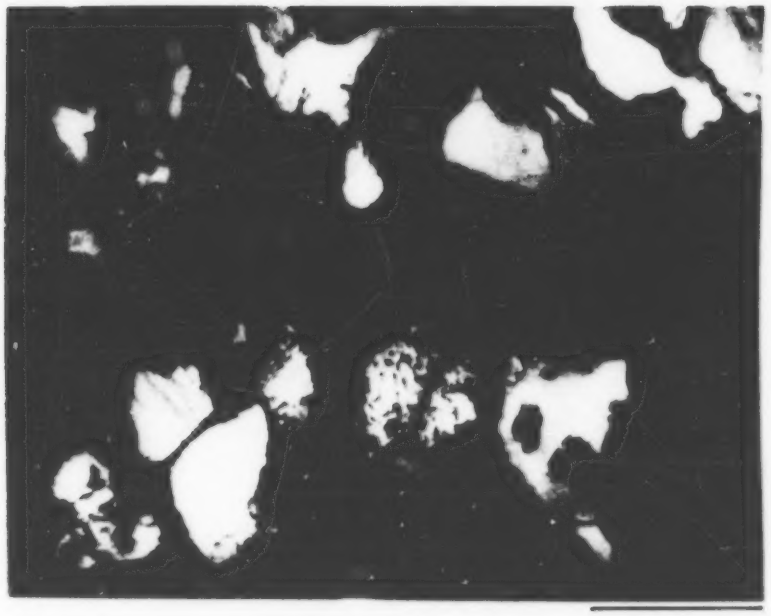

FIGURE 4.2-26a: Disc 31, 65 μm below field surface. 50 000 X (Neg. 2299)

FIGURE 4.2-26b: Diffraction pattern corresponding to Figure 4.2-26a. 3.5 μm S.A. (Neg. 2300)

FIGURE 4.2-27a: Disc 31, 50 μm below field surfaces. 25 000 X (Neg. 2304)

FIGURE 4.2-27b: Diffraction pattern corresponding to central portion of Figure 4.2-27a, 3.5 μm S.A. (Neg. 2307)

FIGURE 4.2-28a: Disc 31, 40 µm below field surface. 50 000 X (Neg. 2297)

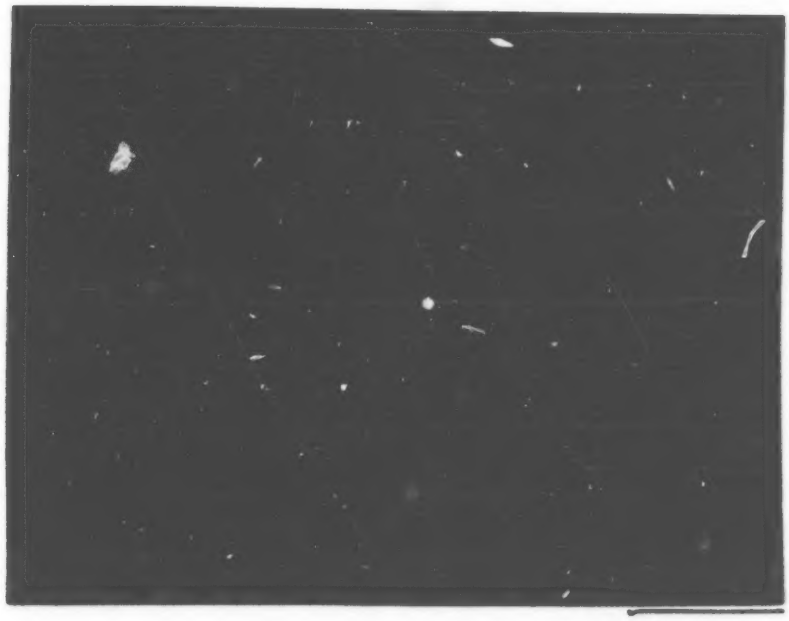

FIGURE 4.2-28b: Diffraction pattern corresponding to Figure 4.2-28a. 3.5 µm S.A. (Neg. 2298)

FIGURE 4.2-29a: Disc 31, 130 µm below tread surface. 25 000 X. (Neg. 2319)

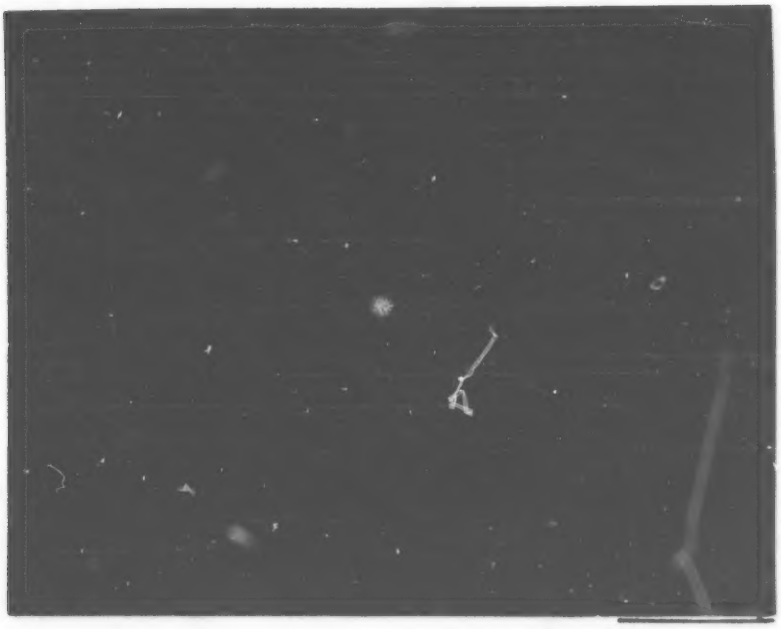

FIGURE 4.2-29b: Diffraction pattern corresponding to central portion of figure 4.2-29a. 3.5 µm S.A. (Neg. 2320)

FIGURE 4.2-30a: Disc 31, 80 μm below tread surface, 25 000 X (Neg. 2367)

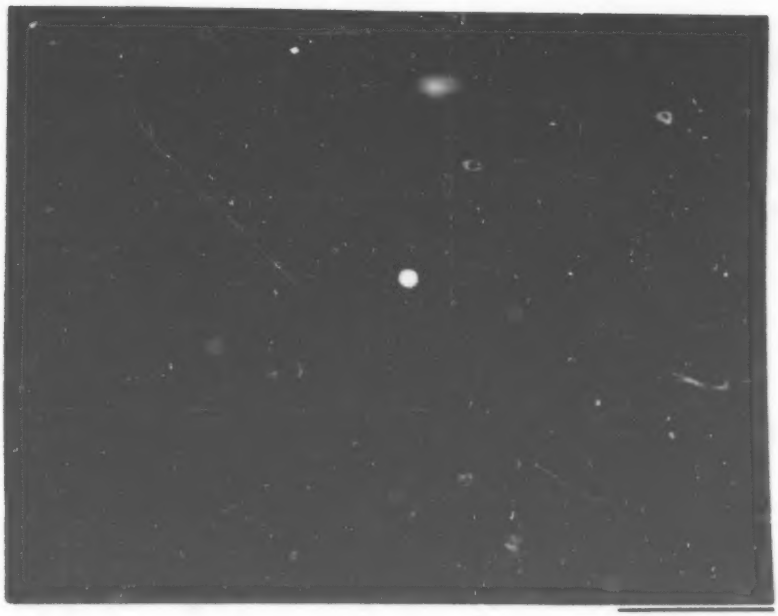

FIGURE 4.2-30b: Diffraction pattern corresponding to central portion of Figure 4.2-30a. 3.5 μm S.A. (Neg. 2318)

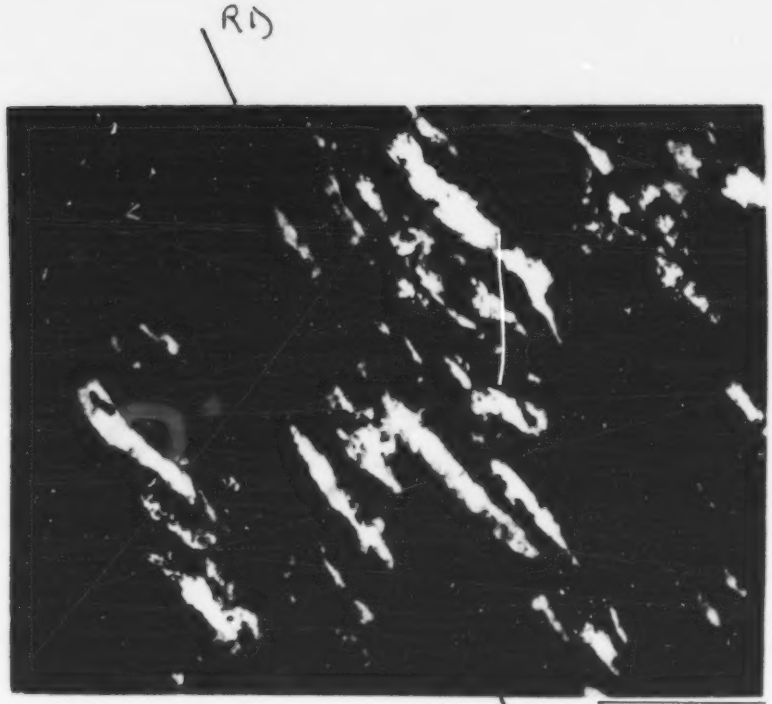

FIGURE 4.2-31a: Disc 31, 33 µm below tread surface, 50 000 X. (Neg. 2291)

FIGURE 4.2-31b: Diffraction pattern corresponding to Figure 4.3-31a. 3.5 µm S.A. (Neg. 2292)

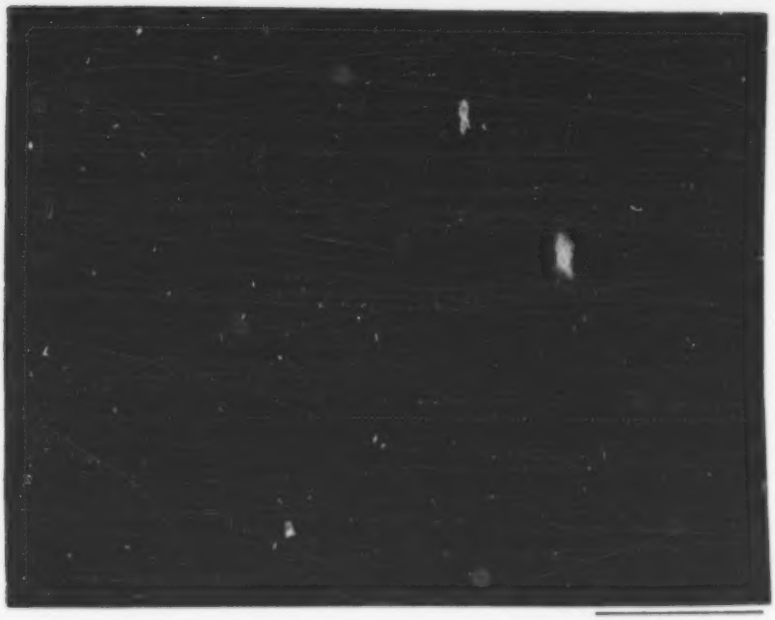

FIGURE 4.2-32a: Disc 31, 75 μm below gage surface. 25 000 X. (Neg. 2311)

FIGURE 4.2-32b: Diffraction pattern corresponding to central portion of Figure 4.2-32a. 0.9 μm S.A. (Neg. 2313).

FIGURE 4.2-33a: Disc 31, 30 μm below gage surface. 25 000 X. (Neg. 2314)

FIGURE 4.2-33b: Diffraction pattern corresponding to central portion of Figure 4.2-33a. 0.9 μm S.A. (Neg. 2316)

FIGURE 4.2-34a: Disc 29, 550 µm below tread surface. 50 000 X. (Neg. 2347)

FIGURE 4.2-34b: Diffraction pattern corresponding to Figure 4.2-34a. µm S.S. (Neg. 2348)

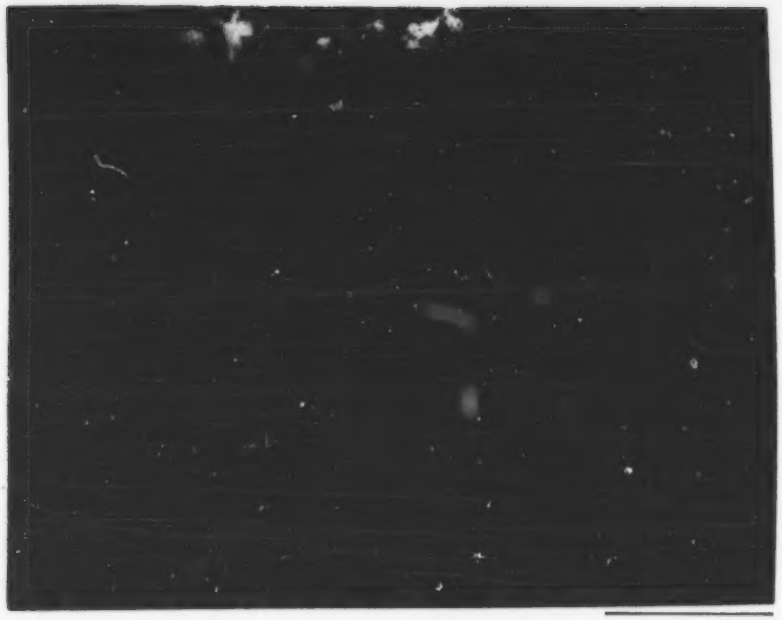

FIGURE 4.2-35a: Disc 29, 110 μm below tread surface. 25 000 X. (Neg 2343)

FIGURE 4.2-35b: Diffraction pattern corresponding to central portion of Figure 4.2-35a. μm S.A. (Neg. 2344)

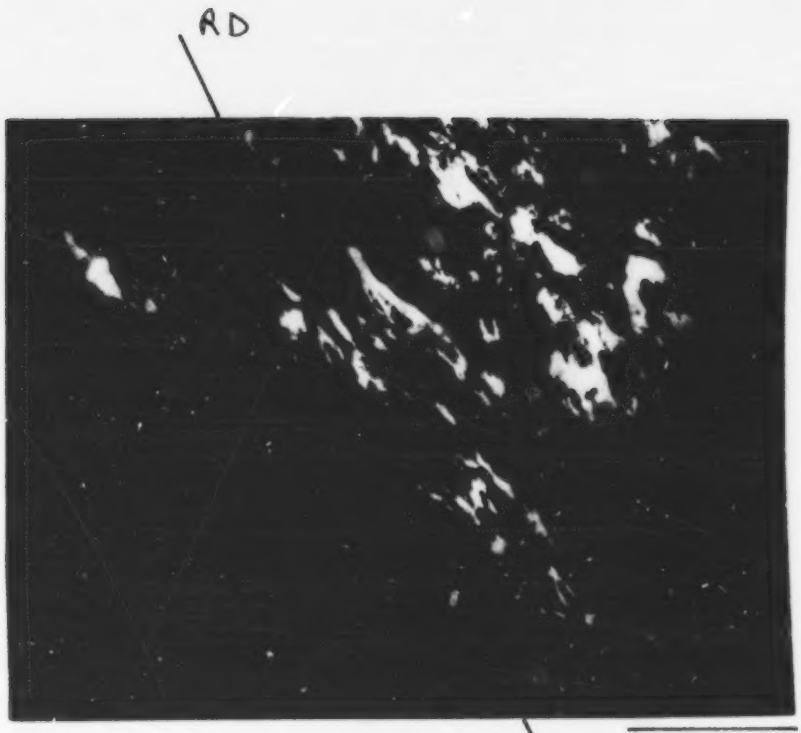

FIGURE 4.2-36a: Disc 29, 70 μm below tread surface. 25 000 X. (Neg. 2345)

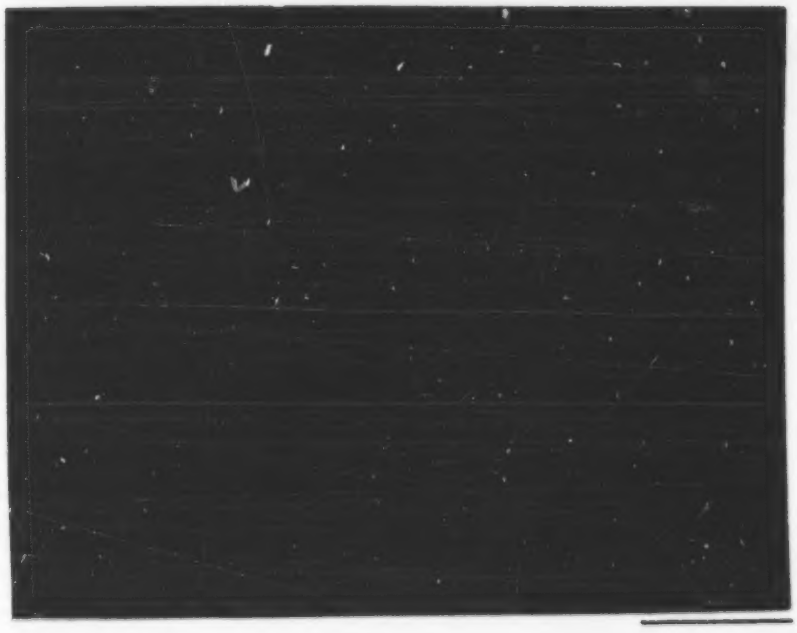

FIGURE 4.2-36b: Diffraction pattern corresponding to central portion of Figures 4.2-36a. μm S.A. (Neg. 2346)

FIGURE 4.2-37a: Disc 28, 100 μm below field surface. 50 000 X. (Neg 2353)

FIGURE 4.2-37b: Diffraction patterns corresponding to Figure 4.2-37a. μm S.A. (Neg. 2354)

FIGURE 4.2-38a. Disc 19, 110 μm below field surface. 75 000 X. (Neg. 2116)

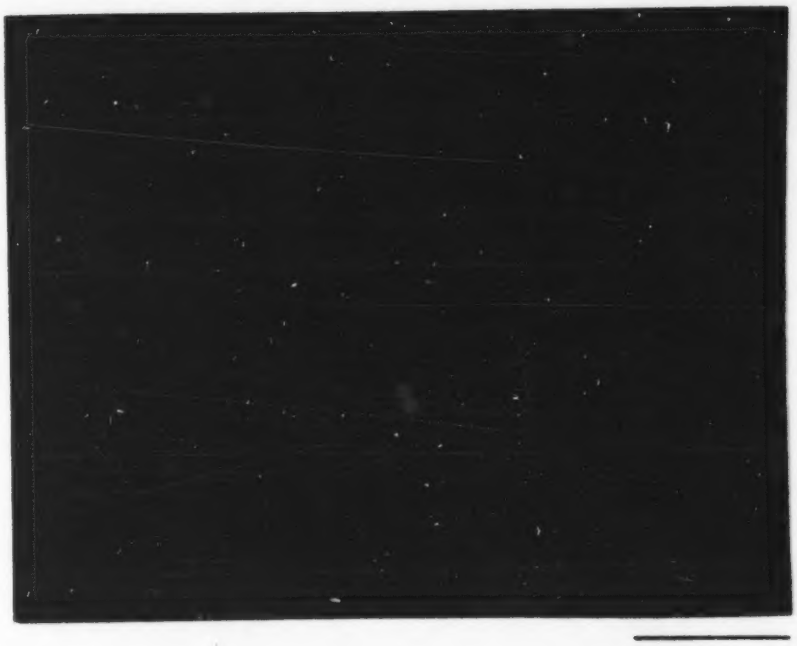

FIGURE 4.2-38b. Diffraction pattern corresponding to figure 4.2-38a. 3.5 μm S.A. (Neg. 2117)

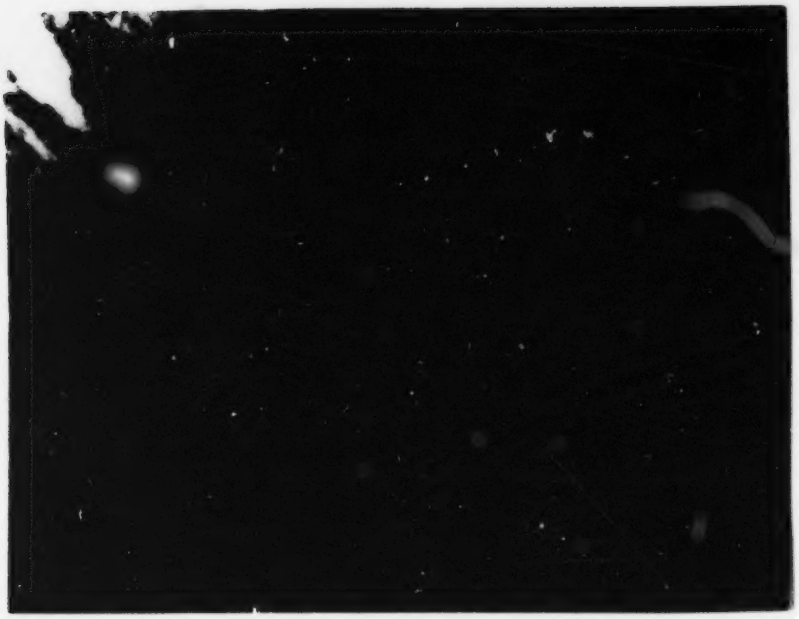

FIGURE 4.2-39a. Disc 19, 12 μm below field surface. 75 000 X. (Neg. 2110)

FIGURE 4.2-39b: Diffraction pattern corresponding to figure 4.2-39a. 3.5 μm S.A. (Neg. 2111)

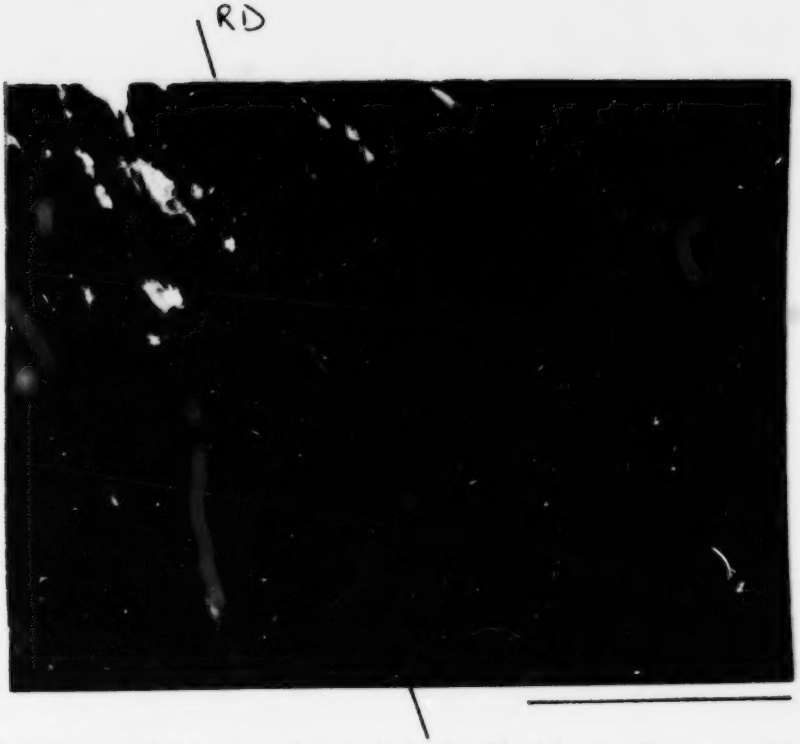

FIGURE 4.2-40a. Disc 19, 6 μm below field surface. 75 000 X, (Neg. 2106)

FIGURE 4.2-40b. Diffraction pattern corresponding to figure 4.2-40a. 3.5 μm S.A. (Neg. 2108)

FIGURE 4.2-41a. Disc 20, 130 μm below tread surface. 50 000 X. (Neg 2243)

FIGURE 4.2-41b. Diffraction pattern corresponding to Figure 4.2-41a. 3.5 μm S.A. (Neg 2244)

FIGURE 4.2-42a. Disc 20, 75 μm below tread surface. 50 000 X. (Neg. 2247)

FIGURE 4.2-42b. Diffraction pattern corresponding to figure 4.2-42a. 3.5 μm S.A. (Neg. 2248)

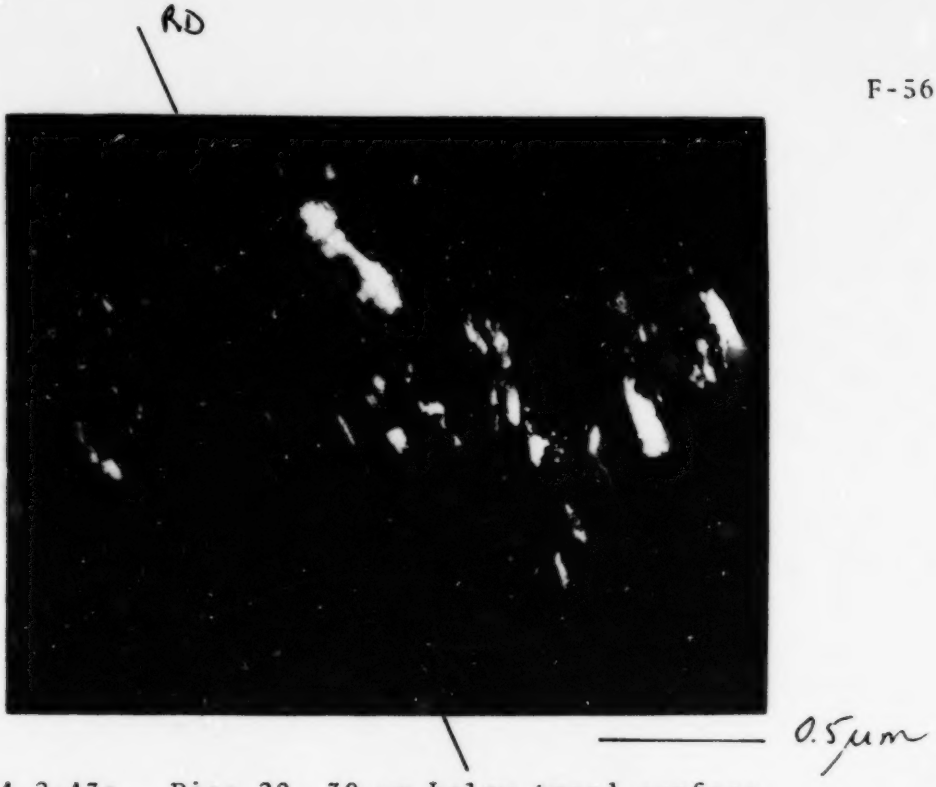

FIGURE 4.2-43a. Disc 20, 30 μm below tread surface. 50 000 X. (Neg 2245)

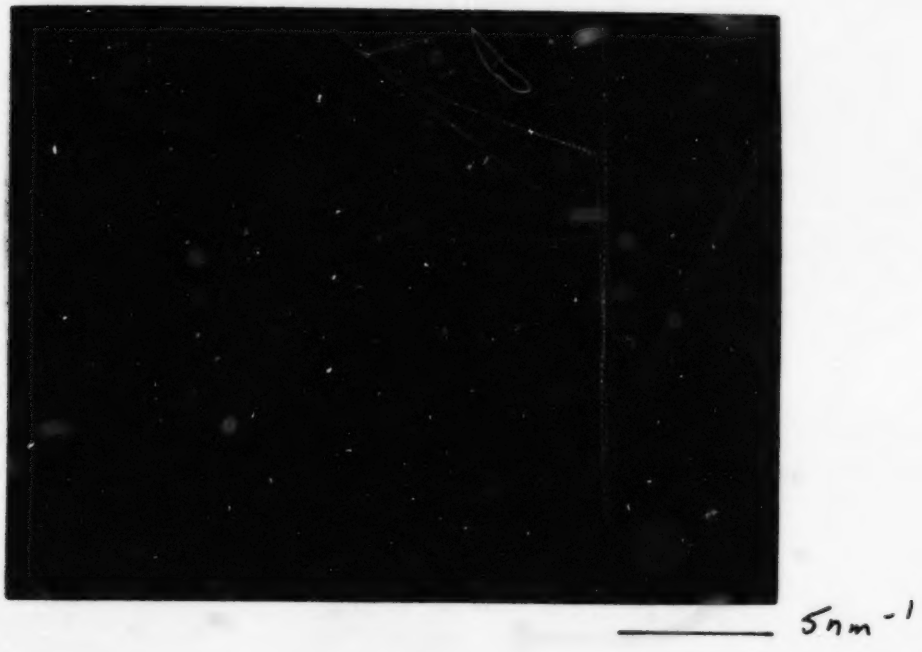

FIGURE 4.2-43b. Diffraction pattern corresponding to figure 4.2-42a. 3.5 μm S.A. (Neg. 2246)

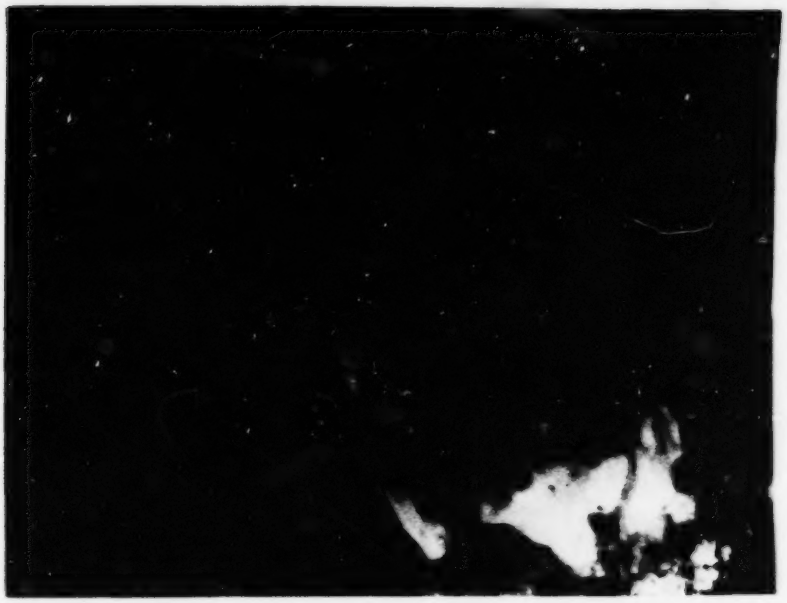

FIGURE 4.2-44a. Disc 14, 300 μm below tread surface. 75 000 X. (Neg. 1944).

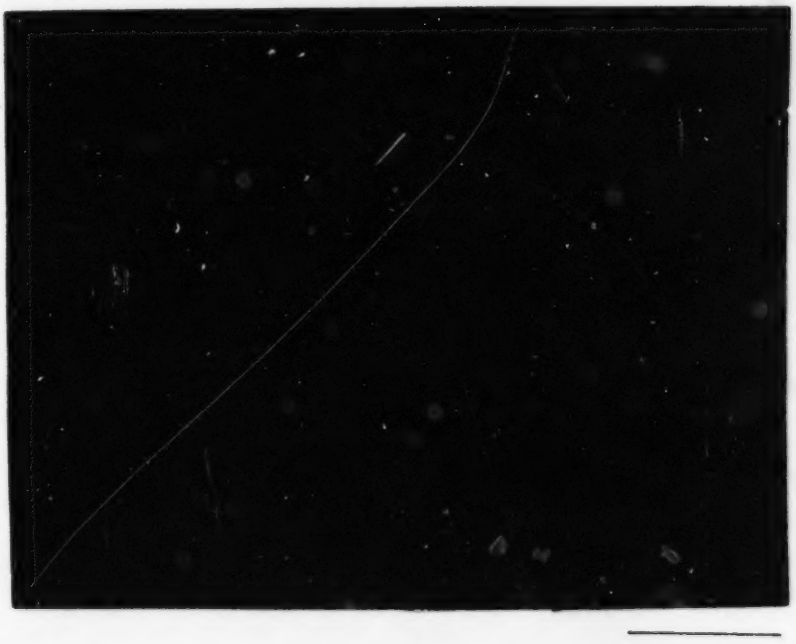

FIGURE 4.2-44b. Diffraction pattern corresponding to Figure 4.2-44a. (Neg. 1945)

FIGURE 4.2-45a: Disc 14, 75 μm below tread surface. 75 000 X. (Neg. 1941)

FIGURE 4.2-45b: Diffraction pattern corresponding to Figure 4.2-45a. (Neg. 1940).

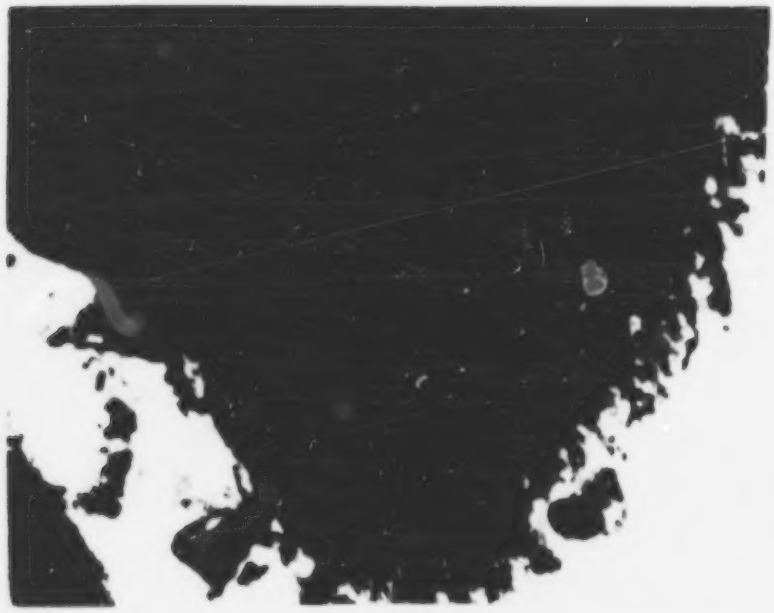

FIGURE 4.2-46a. Disc 14, at tread surface. 100 000 X. (Neg. 1746)

FIGURE 4.2-46b. Diffraction pattern corresponding to figure 4.2-46a. 0.9 μm S.A. (Neg. 1747)

FIGURE 4.2-47a. Disc 14, 72 μm below gage surface. 75 000 X. (Neg. 2426)

FIGURE 4.2-47b. Diffraction pattern corresponding to Figure 4.2-47a. 3.5 μm S.A. (Neg. 2427.

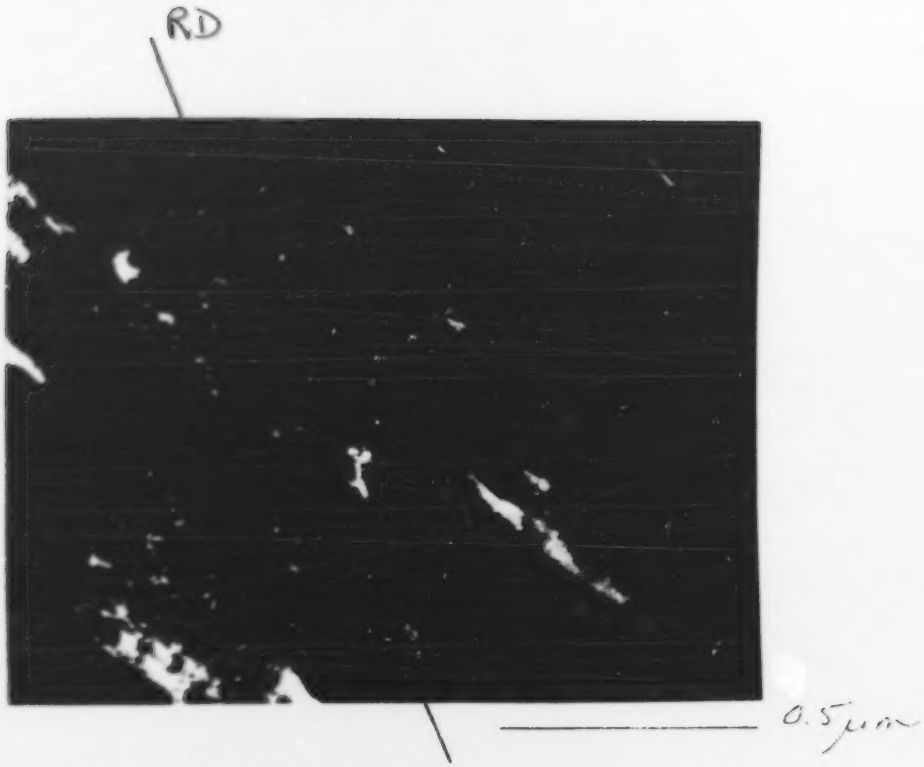

FIGURE 4.2-48a. Disc 14, 30 μm below gage surface. 75 000 X. (Neg. 2422)

FIGURE 4.2-48b. Diffraction pattern corresponding to figure 4.2-48a. 3.5 μm S.A. (Neg 2423)

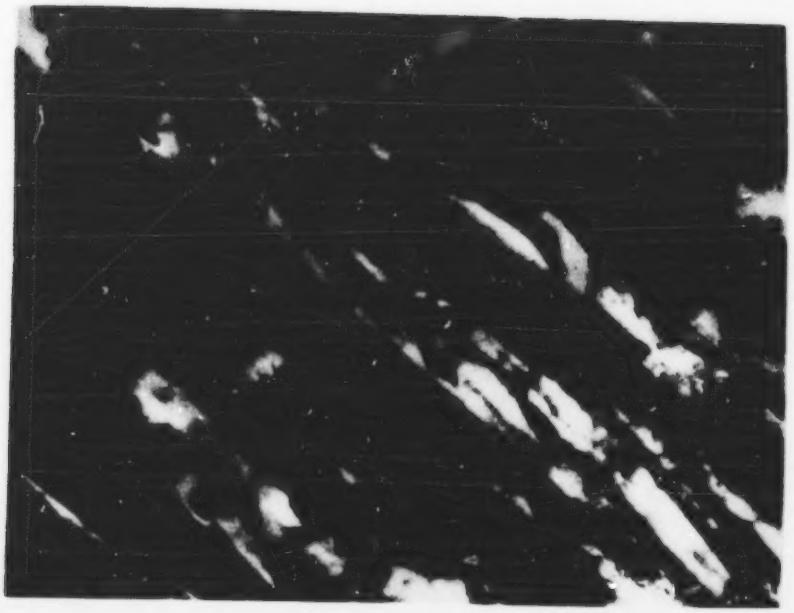

FIGURE 4.2-49a. Disc 15, 140 μm below tread surface. 50 000 X. (Neg. 2132)

FIGURE 4.2-49b. Diffraction pattern corresponding to Figure 4.2-49a. 3.5 μm S.A. (Neg. 2130)

FIGURE 4.2-50a. Disc 15, 55 µm below tread surface. 75 000 X. (Neg. 2122)

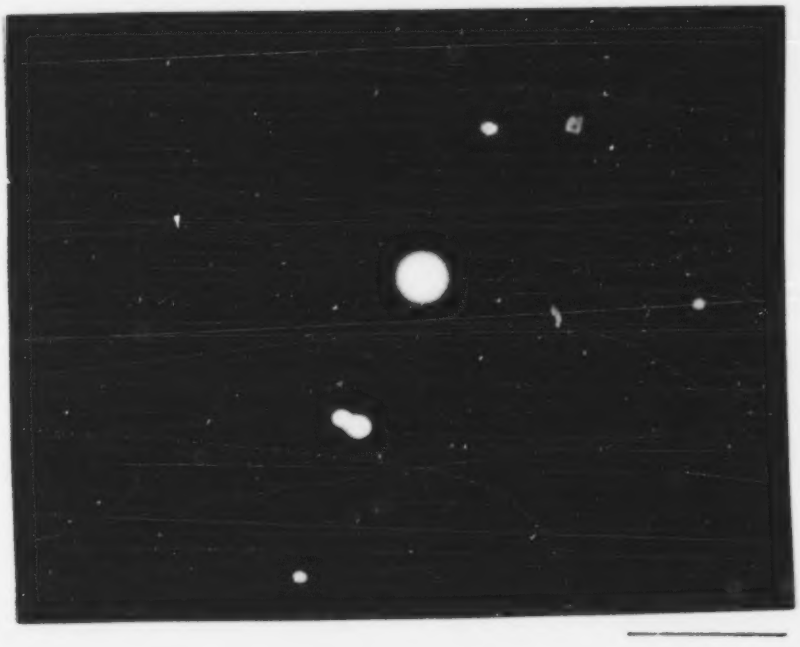

FIGURE 4.2-50b. Diffraction pattern corresponding to Figure 4.2-50a. 3.5 µm S.A. (Neg. 2123).

FIGURE 4.2-51a. Disc 15, 10 μm below tread surface. 75 000 X. (Neg. 2003).

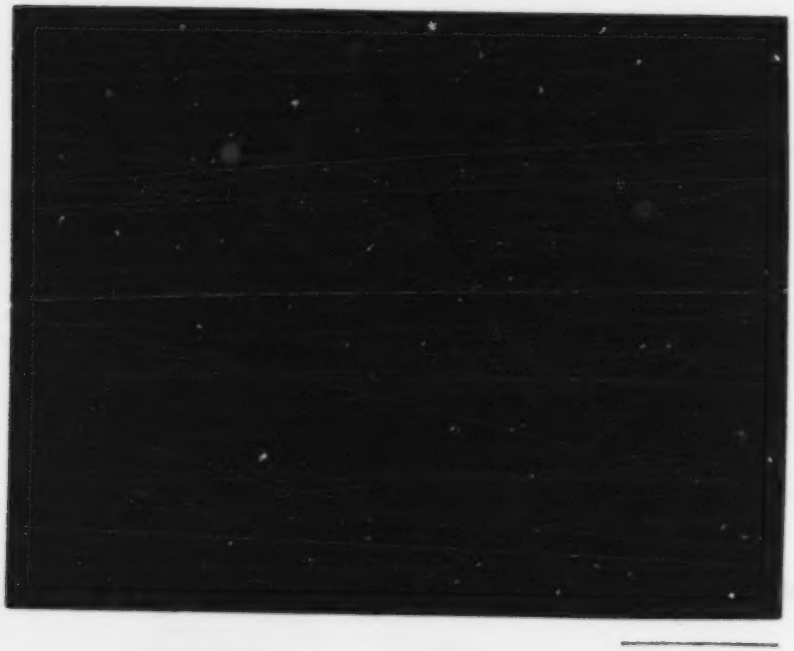

FIGURE 4.2-51b. Diffraction pattern corresponding to Figure 4.2-51a. 0.9 μm S.A. (Neg. 2004)

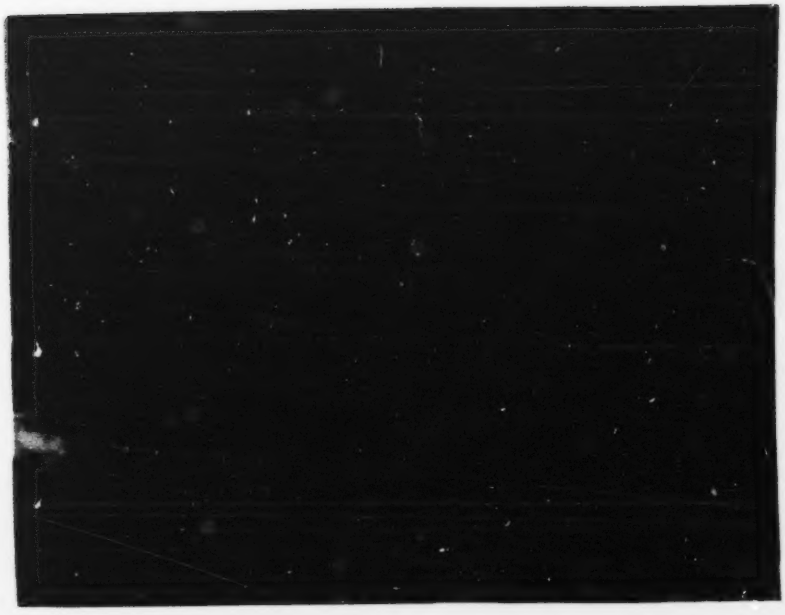

FIGURE 4.2-52a. Disc 36, 110 μm below gage surface. 50 000 X. (Neg. 2142)

FIGURE 4.2-52b. Diffraction pattern corresponding to Figure 4.2-52a. 3.5 μm S.A. (Neg. 2143)

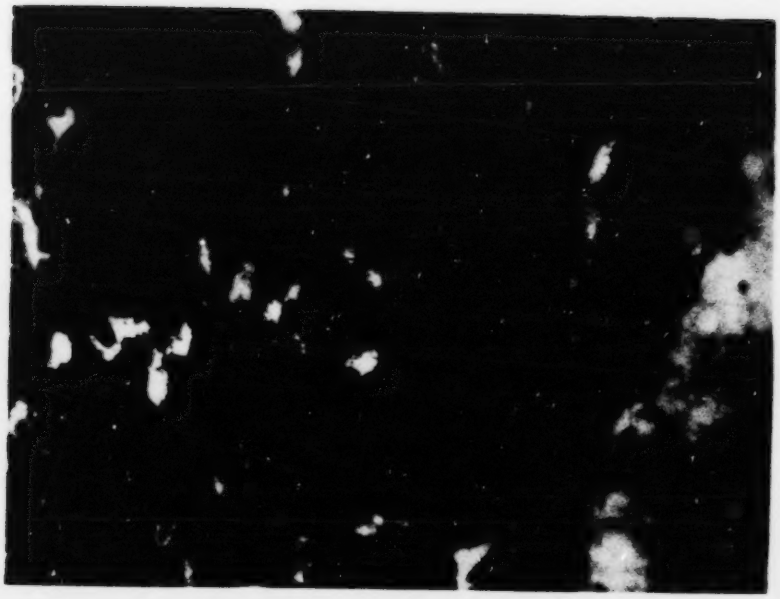

FIGURE 4.2-53a. Disc 36, 90 μm below gage surface. 75 000 X. (Neg. 2144)

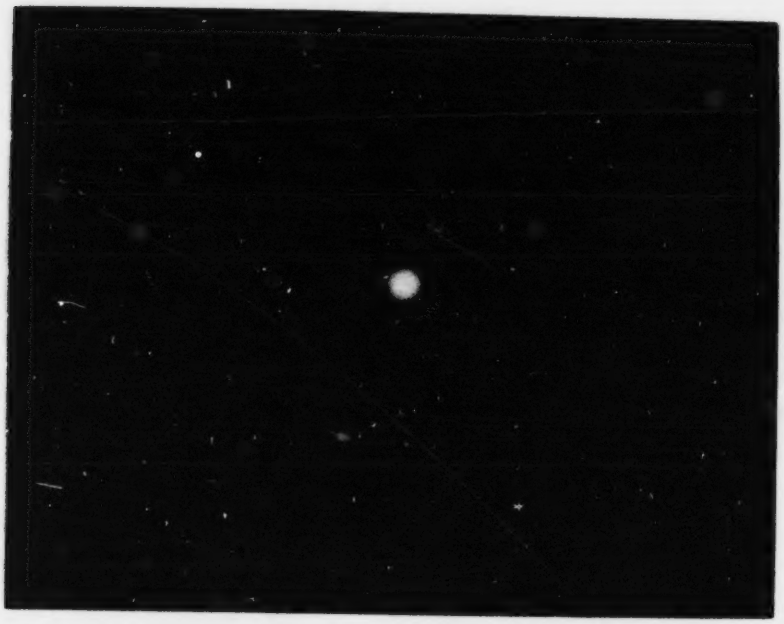

FIGURE 4.2-53b. Diffraction pattern corresponding to Figure 4.2-53a. 3.5 μm S.A. (Neg. 2145).

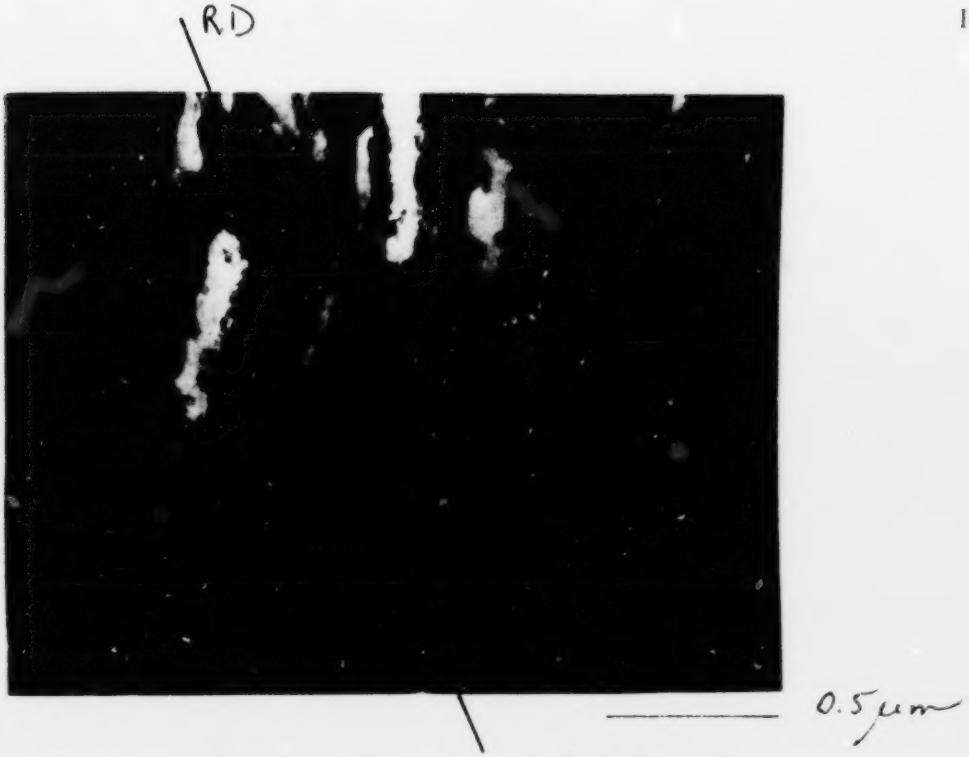

FIGURE 4.2-54a. Disc 36, 75 μm below field surface. 50 000 X. (Neg. 2150)

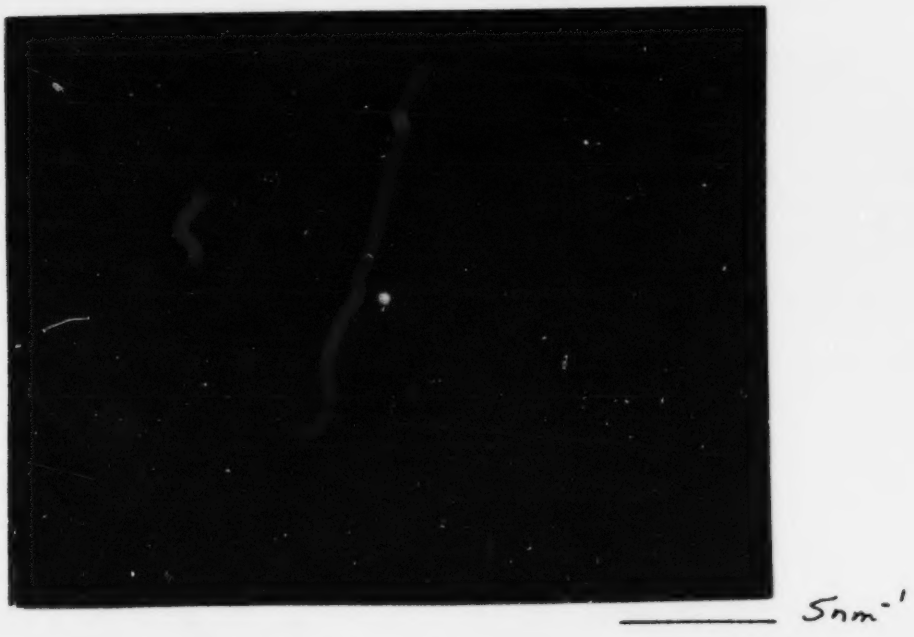

FIGURE 4.2-54b. Diffraction pattern corresponding to Figure 4.2-54a. 3.5 μm S.A. (Neg. 2151).

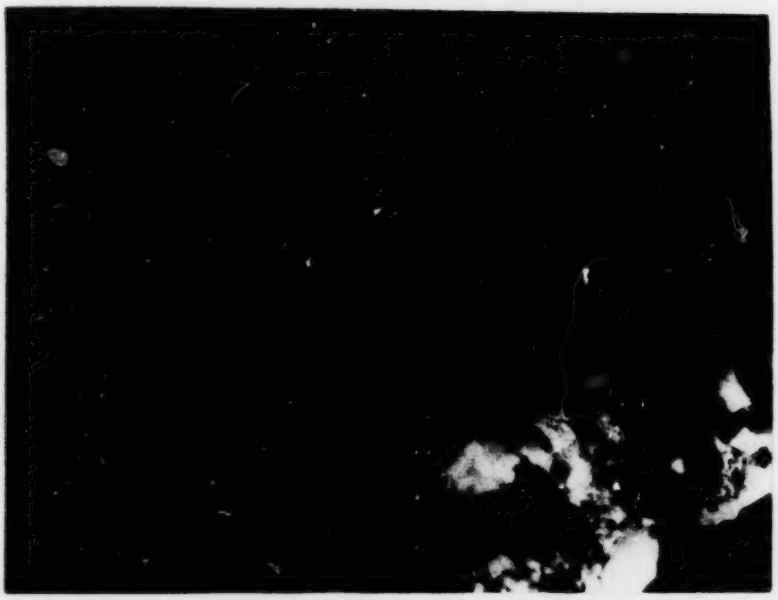

FIGURE 4.2-55a. Disc 36, 20 μm below field surface. 75 000 X. (Neg. 2015)

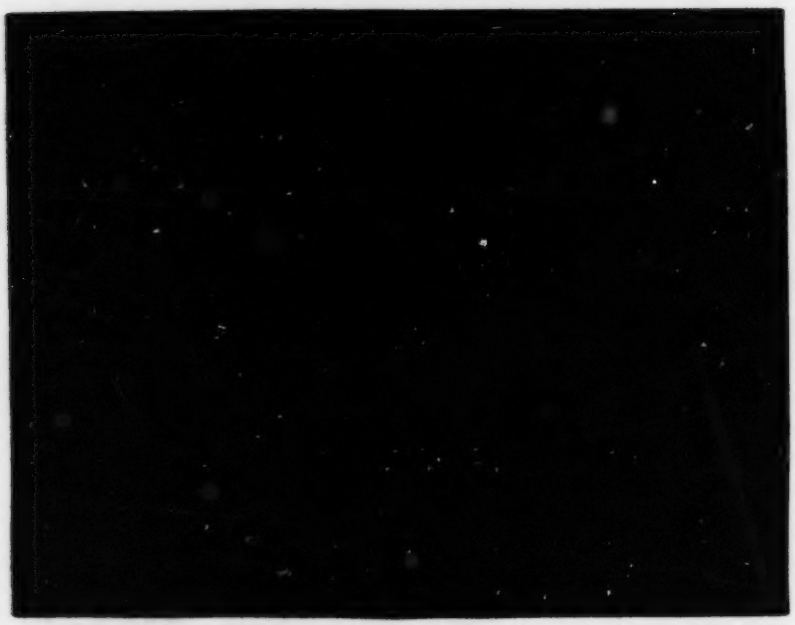

FIGURE 4.2-55b. Diffraction pattern corresponding to Figure 4.2-55a. (Neg. 2016)

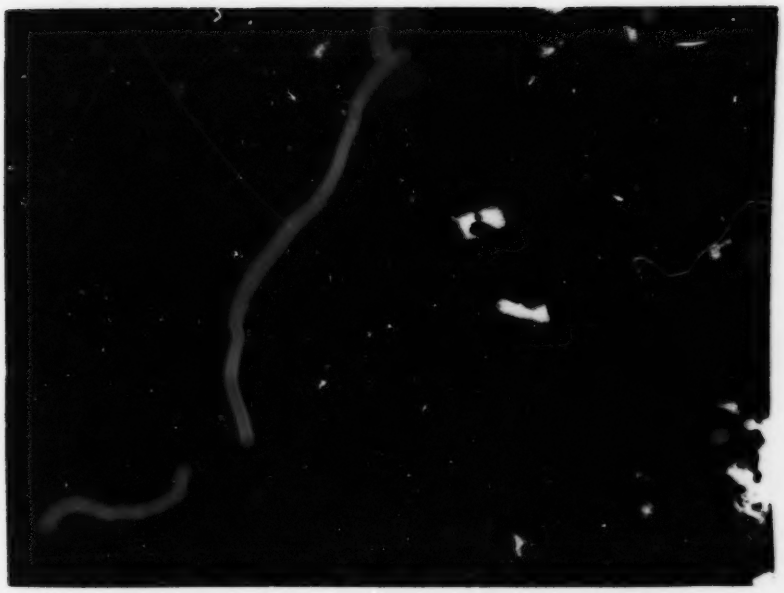

FIGURE 4.2-56a. Disc 37, 150 µm below tread surface. 75 000 X (Neg. 2084)

FIGURE 4.2-56b. Diffraction pattern corresponding to figure 4.2-56a. 3.5 µm S.A. (Neg. 2085)

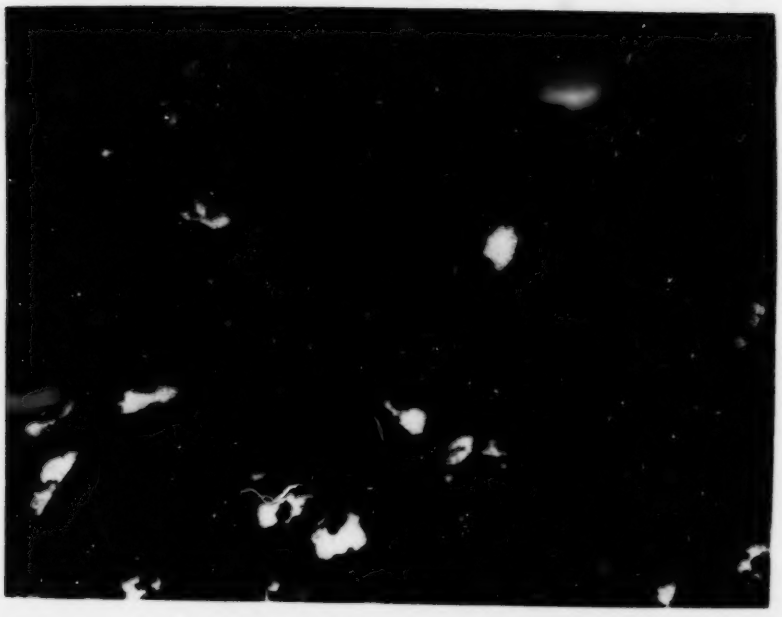

FIGURE 4.2-57a. Disc 37, 90 µm below tread surface. 75 000 X (Neg. 2080)

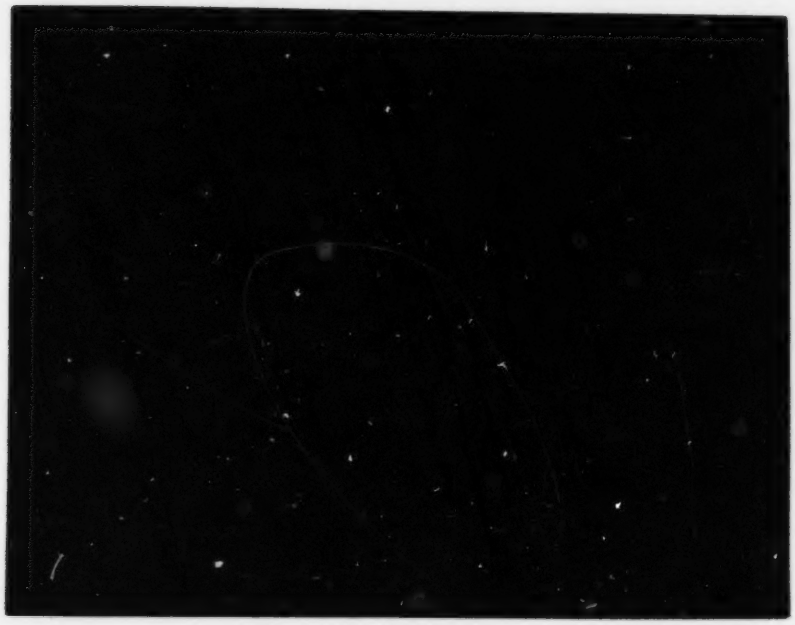

FIGURE 4.2-57b. Diffraction pattern corresponding to figure 4.2-57a. 3.5 µm S.A. (Neg 2081)

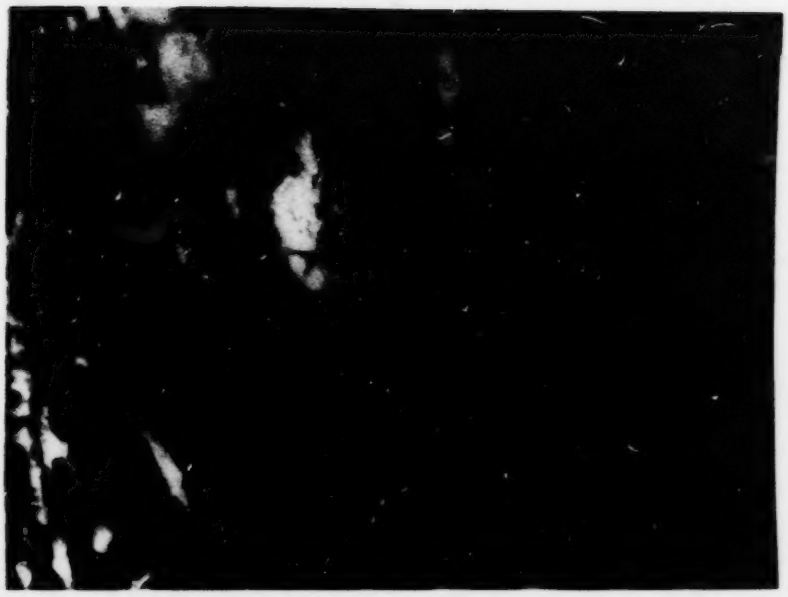

FIGURE 4.2-58a. Disc 37, 75 μm below tread surface. 75 000 X. (Neg. 2058)

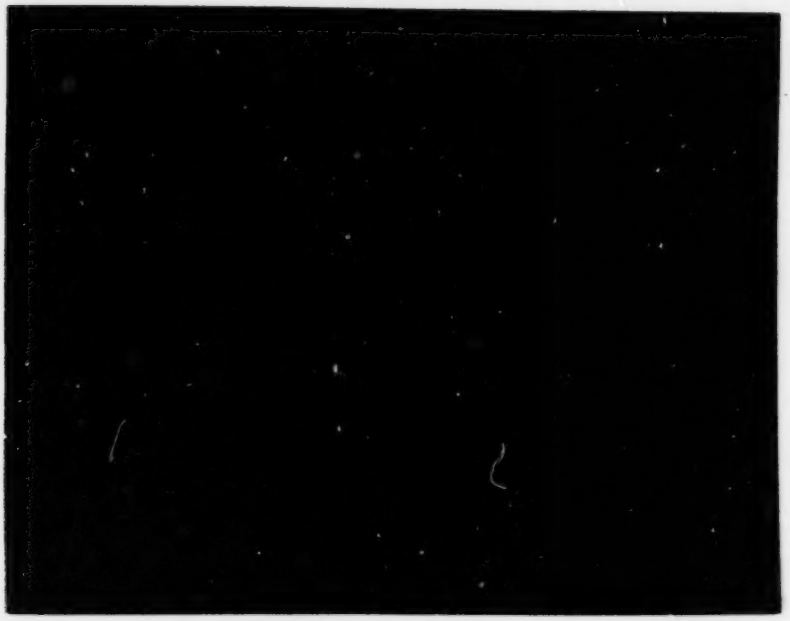

FIGURE 4.2-58b. Diffraction pattern corresponding to figure 4.2-58a. 3.5 μm S.A. (Neg. 2059)

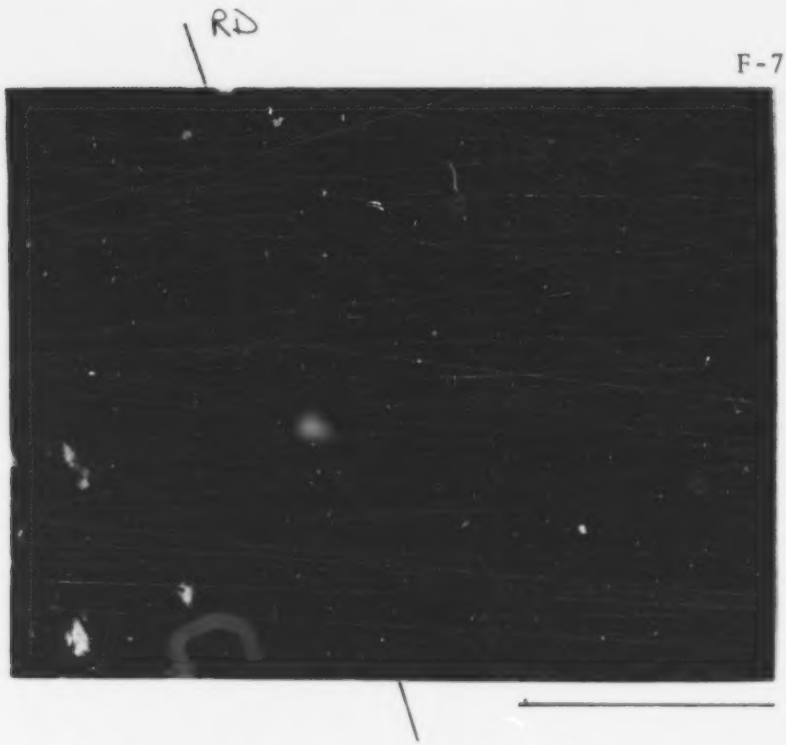

FIGURE 4.2-59a. Disc 37, 50 μm below gage surface. 75 000 X. (Neg 2041)

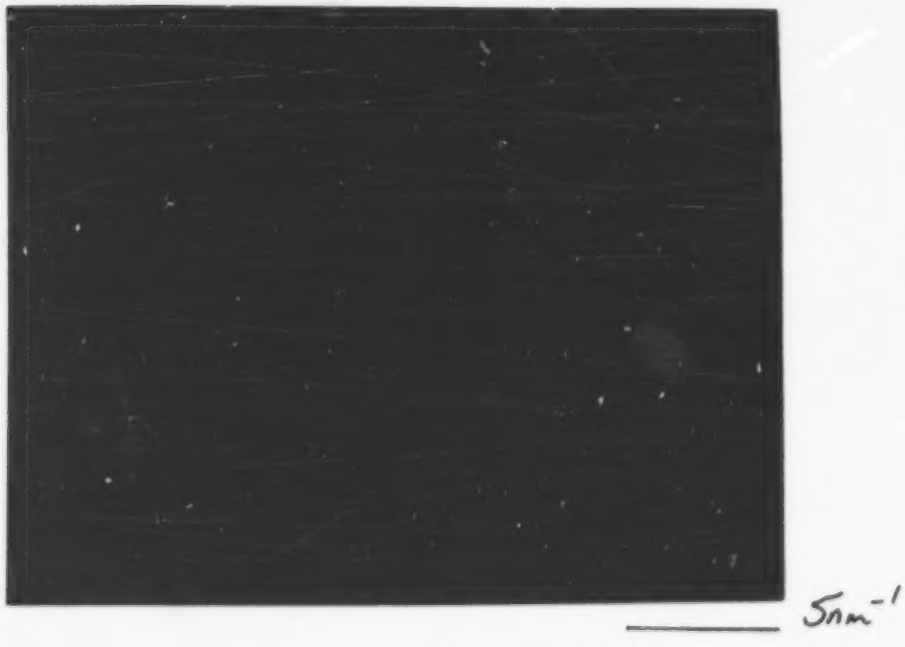

FIGURE 4.2-59b. Diffraction pattern corresponding to Figure 4.2-59a. 3.5 μm S.A. (Neg. 2040)

FIGURE 4.2-60a. Disc 38, 130 µm below field surface. 75 000 X (Neg. 2196)

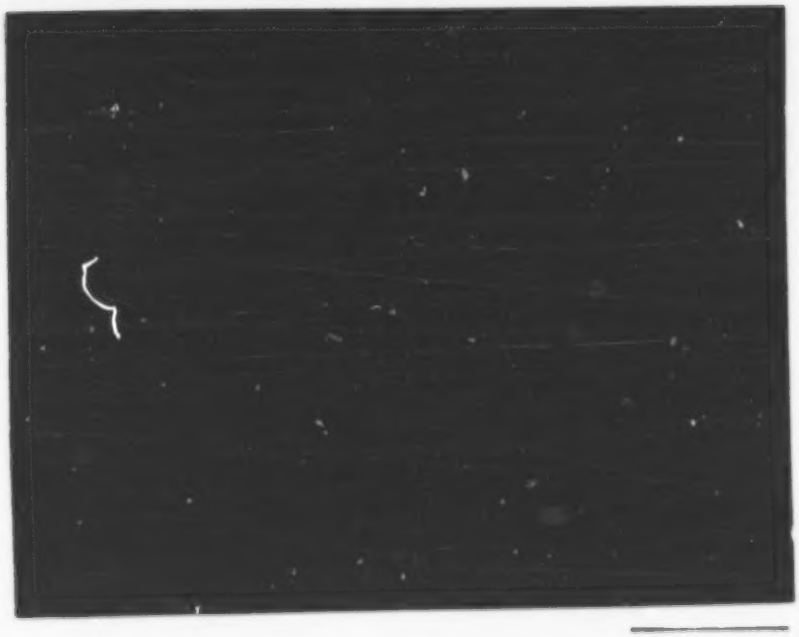

FIGURE 4.2-60b. Diffraction pattern corresponding to figure 4.2-60a. 3.5 µm S.A. (Neg. 2197)

FIGURE 4.2-61a. Disc 38, 35 μm below tread surface. 75 000 X. (Neg 2177)

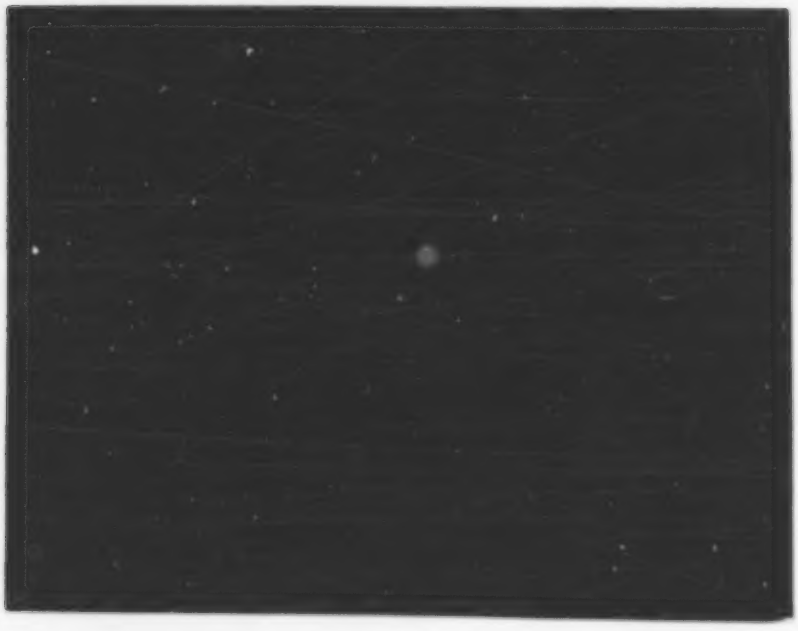

FIGURE 4.2-61b. Diffraction pattern corresponding to figure 4.2-61a. 3.5 μm S.A. (Neg. 2178)

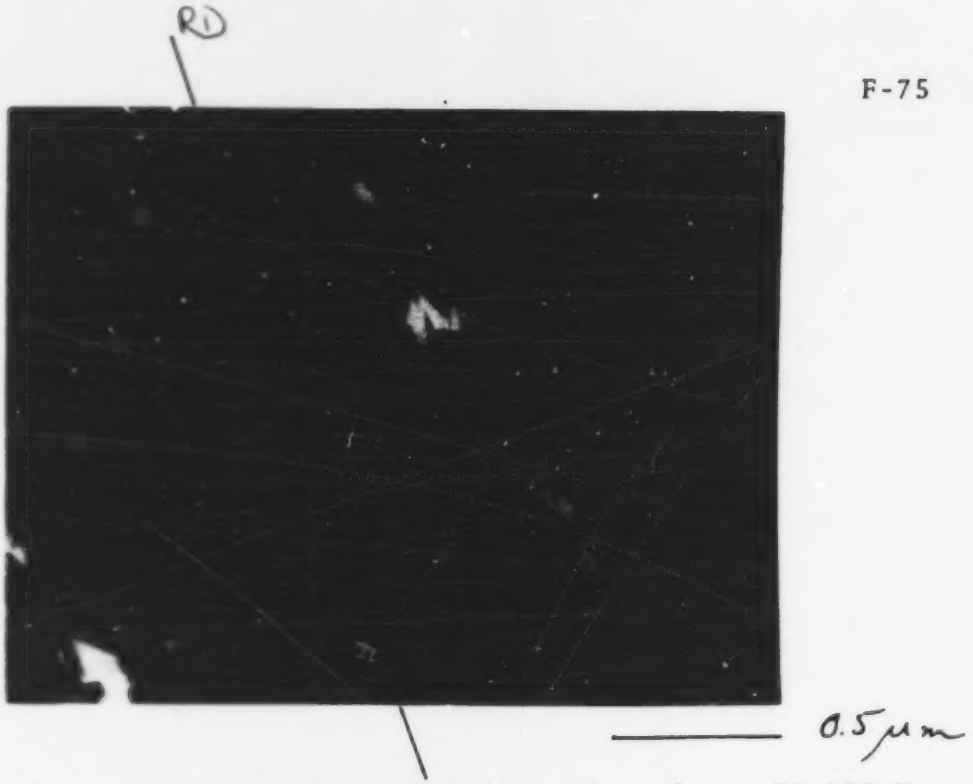

FIGURE 4.2-62a. Disc 38, 20 µm below tread surface. 50 000 X. (Neg. 2183)

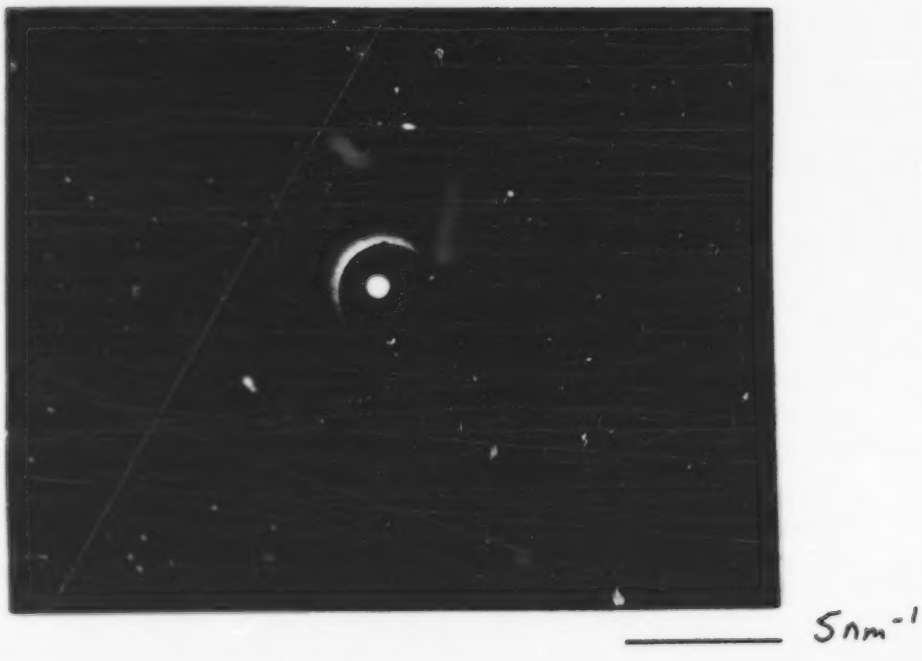

FIGURE 4.2-62b. Diffraction pattern corresponding to figure 4.2-62a. 3.5 µm S.A. (Neg. 2184)

1 µm

FIGURE 4.2-63a. Disc 39, 180 µm below the field surface. 25 000 X. (Neg. 2226)

FIGURE 4.2-63b. Diffraction pattern corresponding to figure 4.2-63a. 3.5 μm S.A. (Neg. 2227)

FIGURE 4.2-63c. Diffraction patterns corresponding to a single grain in figure 4.2-63a. 0.9 μm S.A. (Neg. 2228)

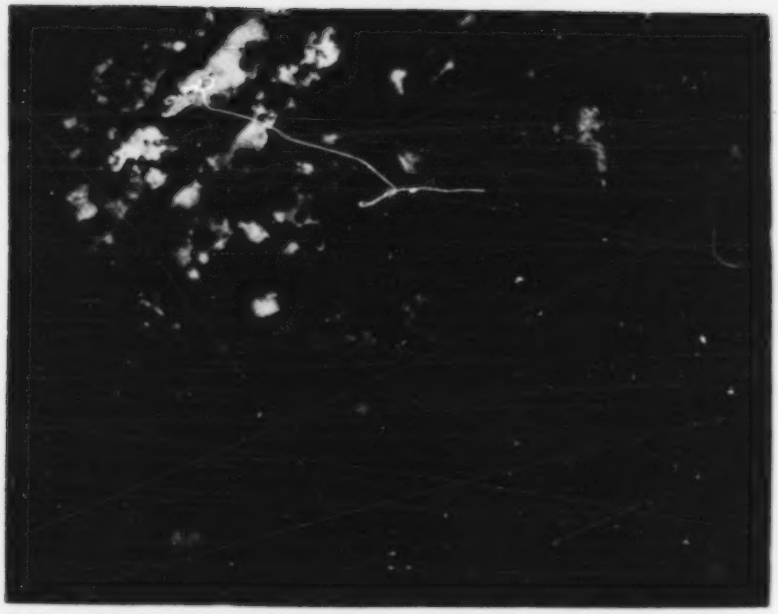

FIGURE 4.2-64a. Disc 39, 35 μm below field surface. 50 000 X. (Neg. 2133)

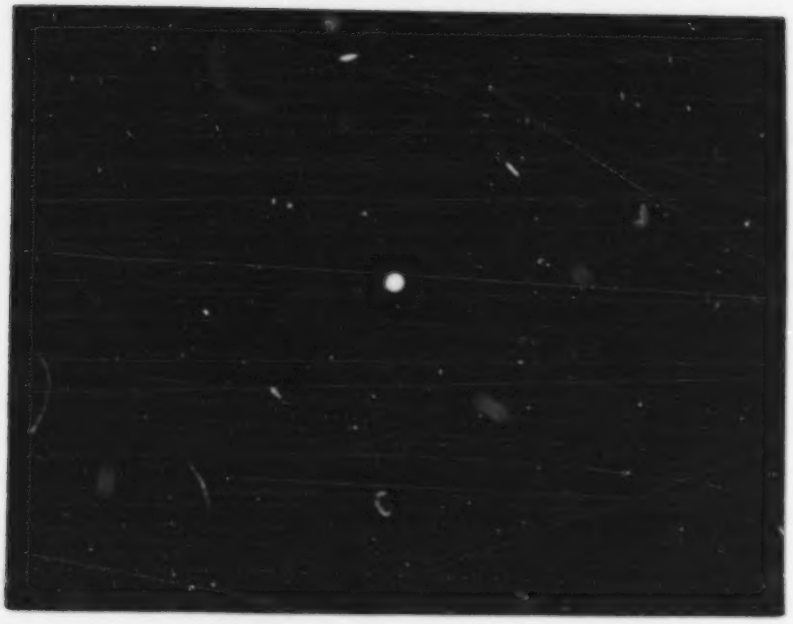

FIGURE 4.2-64b. Diffraction pattern corresponding to figure 4.2-64a. 3.5 μm S.A. (Neg. 2134)

FIGURE 4.2-65a. Disc 40, 260 µm below field surface. 50 000 X. (Neg. 2162)

FIGURE 4.2-65b. Diffraction pattern corresponding to figure 4.2-65a. 3.5 µm S.A. (Neg. 2163).

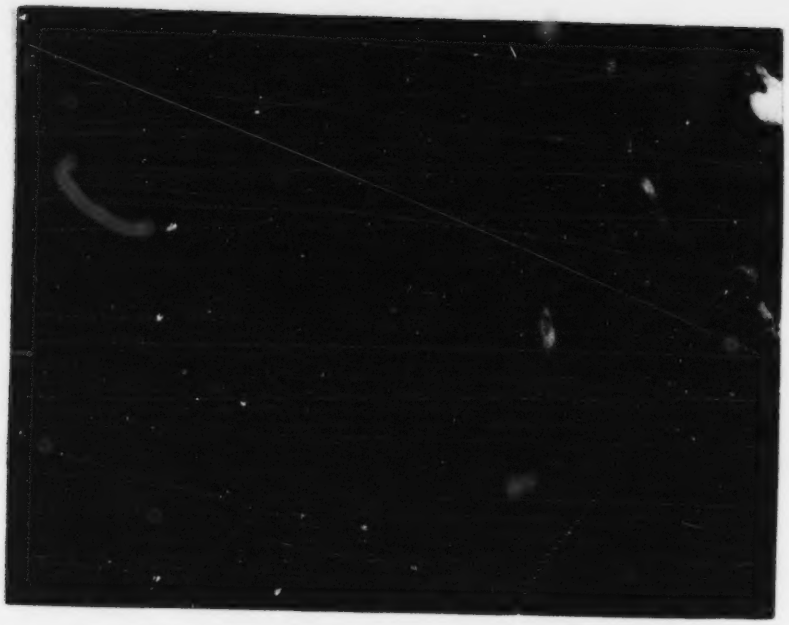

FIGURE 4.2-66a. Disc 40, 35 μm below tread surface. 50 000 X. (Neg. 2269).

FIGURE 4.2-66b. Diffraction pattern corresponding to Figure 4.2-66a. 3.5 μm S.A. (Neg. 2270)

FIGURE 4.2-67a. Disc 40, 10 μm below tread surface. 50 000 X. (Neg. 2263)

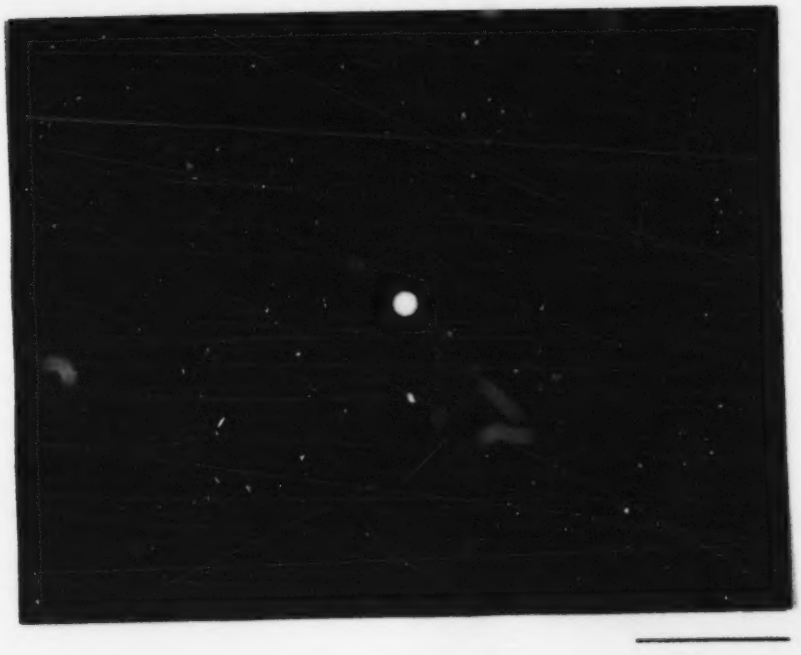

FIGURE 4.2-67b. Diffraction pattern corresponding to Figure 4.2-67a. 3.5 μm S.A. (Neg. 2264)

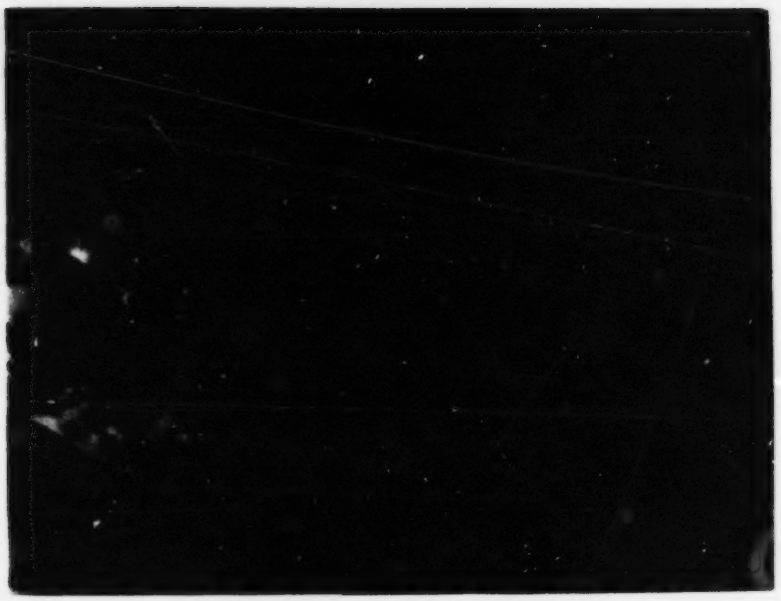

FIGURE 4.2-68a. Disc 41, 135 μm below field surface. 50 000 X. (Neg. 2278)

FIGURE 4.2-68b. Diffraction pattern corresponding to Figure 4.2-68a. 3.6 μm S.A. (Neg. 2279)

FIGURE 4.2-69a. Disc 41, 80 µm below field surface. 50 000 X. (Neg. 2276)

FIGURE 4.2-69b. Diffraction pattern corresponding to Figure 4.2-69a. 3.5 µm S.A. (Neg. 2277)

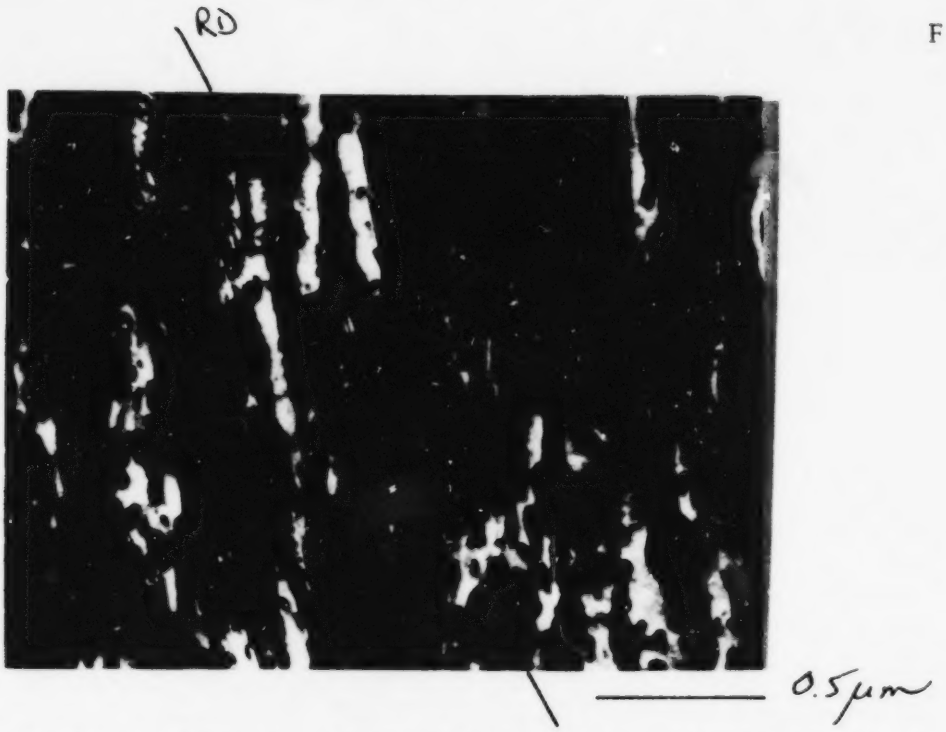

FIGURE 4.2-70a. Disc 41, 50 μm below tread surface. 50 000 X. (Neg. 2257)

FIGURE 4.2-70b. Diffraction pattern corresponding to Figure 4.2-70a. 3.5 μm S.A. (Neg. 2258)

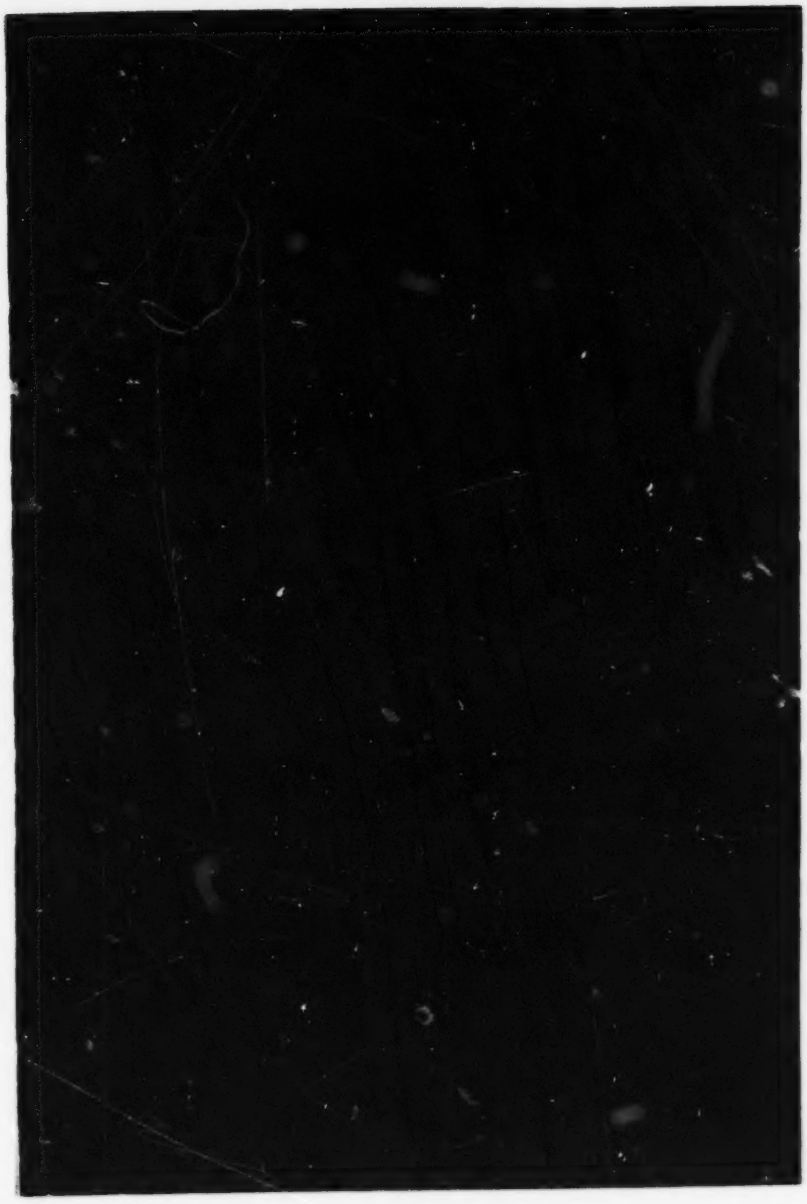

FIGURE 4.2-71. Disc 41, 70 μm below tread surface. Overview showing elongated grain structure. 15 000 X (Neg. 2284)

FIGURE 4.2-72. Disc 12, 160 μm below field surface. Opaque areas are martensite. 2000 X. (Neg. 2198)

FIGURE 4.2-73. Disc 12, 160 μm below field surface. Note increased deformation between martensite particles. 6000 X (Neg. 2199)

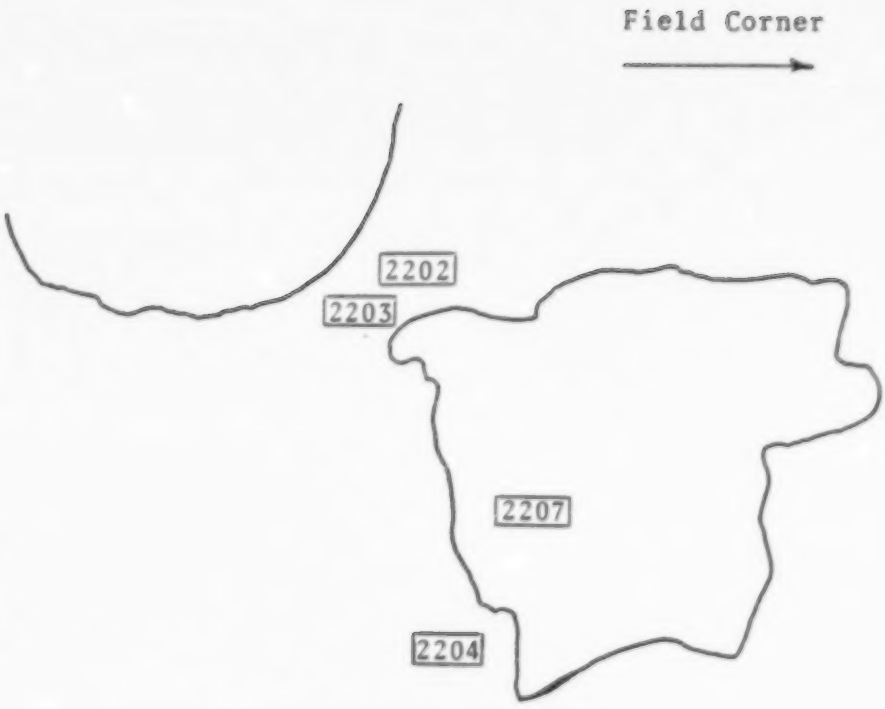

FIGURE 4.2-74. Sketch showing locations of figures 4.2-75 to 4.2-78. Compare Figure 4.2-73.

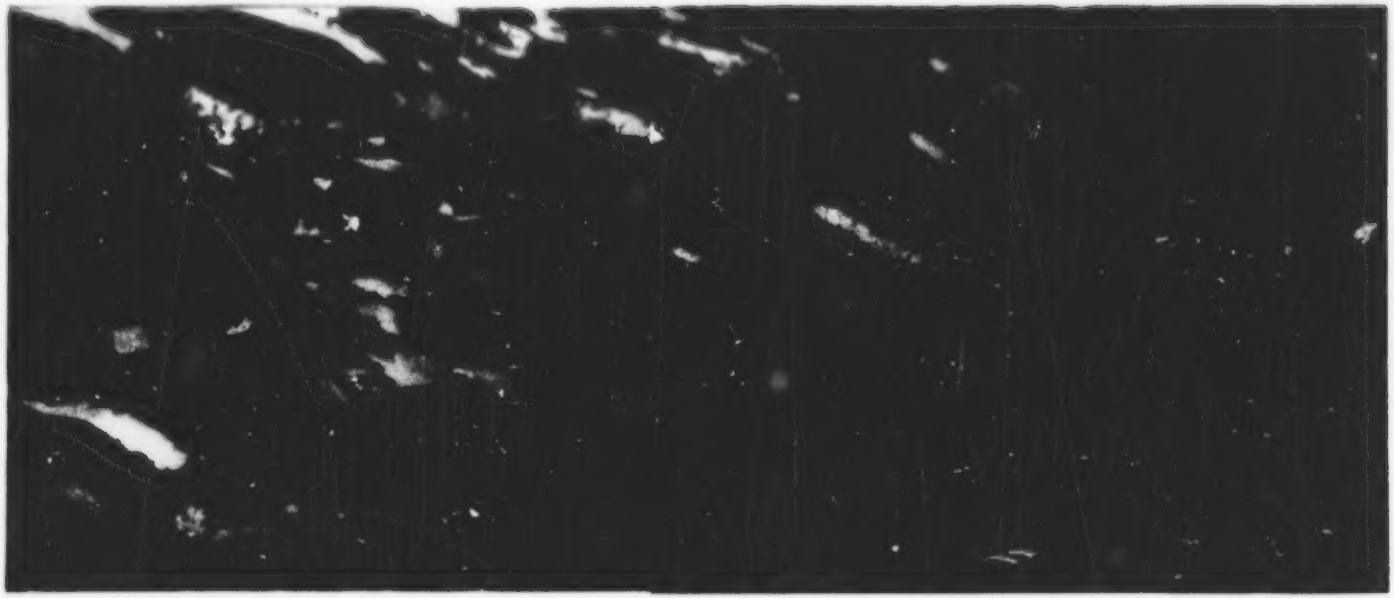

1 μm

FIGURE 4.2-75a. Disc 12, 160 μm below field surface, Augmented deformation near martensite. 25 000 X. (Negs. 2202, 2203)

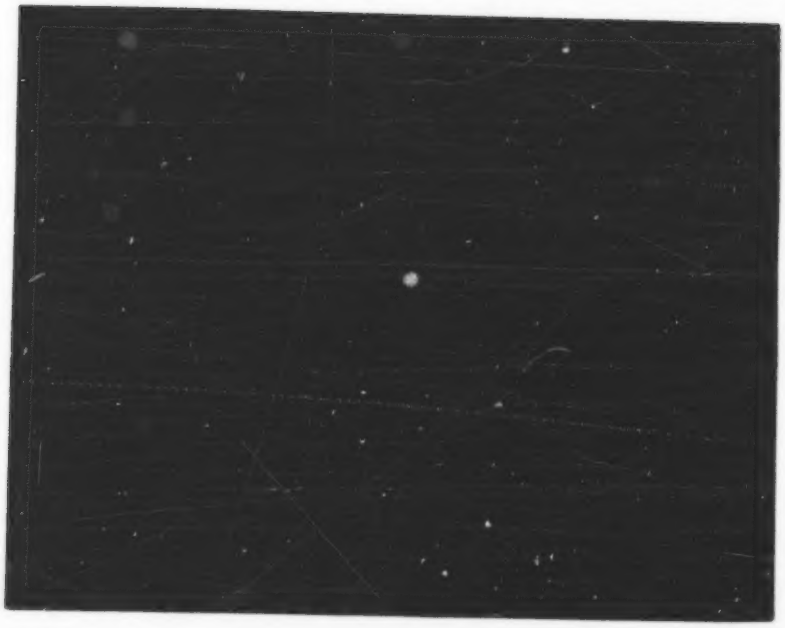

FIGURE 4.2-75b. Diffraction pattern corresponding to Figure 4.2-75a. 3.5 μm S.A. (Neg. 2333)

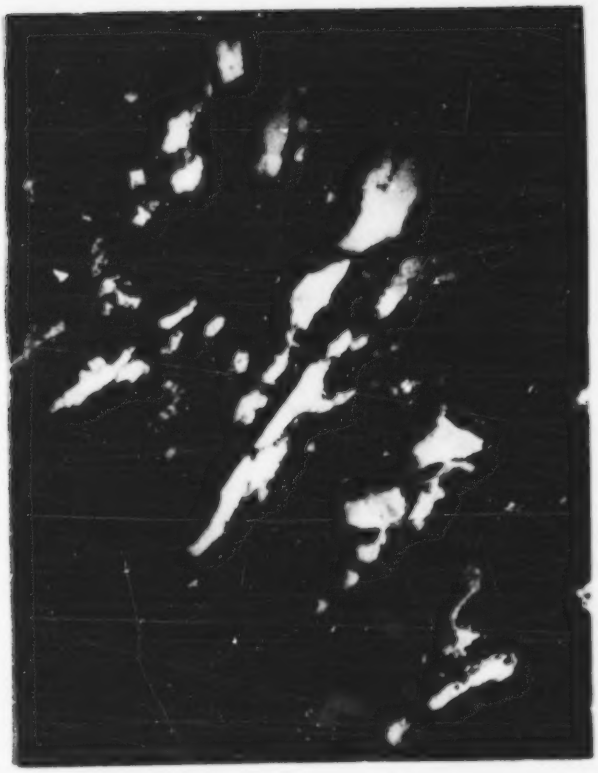

1 µm

FIGURE 4.2-76 Disc 12, 160 µm below field surface.
25 000 X (Neg. 2204)

FIGURES 4.2-77a. Disc 12, 160 μm below field surface, 20 μm from martensite. Compare figure 4.2-29. 25 000 X (Neg. 2208)

FIGURE 4.2-77b. Diffraction pattern corresponding to Figure 4.2-77a. 3.5 μm S.A. (Neg. 2209)

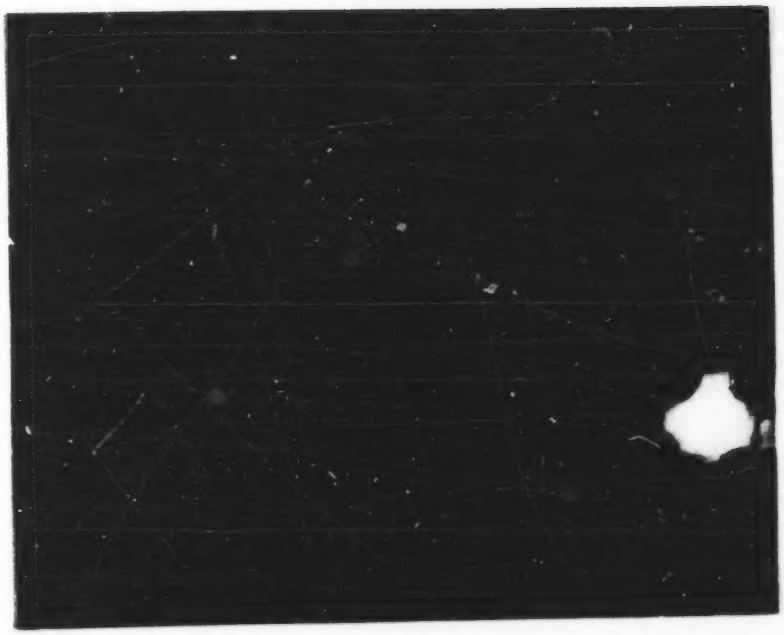

FIGURE 4.2-78. Disc 12, 160 μm below field surface, Detail of martensite particle. 25 000 X. (Neg. 2207).

WEAR of MATERIALS 1985

presented at

THE INTERNATIONAL CONFERENCE ON WEAR OF MATERIALS
VANCOUVER, B. C. CANADA
APRIL 14–18, 1985

sponsored by

THE AMERICAN SOCIETY OF MECHANICAL ENGINEERS
THE AMERICAN SOCIETY FOR TESTING AND MATERIALS
THE AMERICAN INSTITUTE OF MINING, METALLURGICAL AND PETROLEUM ENGINEERS
THE AMERICAN SOCIETY FOR METALS
THE AMERICAN CERAMIC SOCIETY
THE SOCIETY OF PLASTICS ENGINEERS

edited by

K. C. LUDEMA
UNIVERSITY OF MICHIGAN

OCT 23 1985
MICROMEDIA

21 pp

THE AMERICAN SOCIETY OF MECHANICAL ENGINEERS
United Engineering Center 345 East 47th Street New York, N.Y. 10017

THE WEAR RESISTANCE AND WORN METALLOGRAPHY OF PEARLITE, BAINITE AND TEMPERED MARTENSITE RAIL STEEL MICROSTRUCTURES OF HIGH HARDNESS

J. Kalousek
National Research Council of Canada
Vancouver, B.C., Canada

D. M. Fegredo
Physical Metallurgy Research Laboratories
Ottawa, Ontario, Canada

E. E. Laufer
Technical University of Nova Scotia, Mining and Metallurgy
Halifax, N.S., Canada

ABSTRACT

In order to find out if it is worthwhile to produce premium rail steels harder than HRC 36 to HRC 39, and to discover the best microstructure for wear-resistant rail, an experimental Cr-Mo alloy rail steel was heat treated to pearlite, bainite and tempered martensite. Each microstructure was prepared at hardness levels of HRC 38, 42 and 45. These were tested in a dual disk-on-disk machine that closely simulates wheel/rail contact in curves, at 1/10 scale. Wear rates were established for dry, grease-sand and pure grease environments. Dry wear rates decreased significantly with increasing hardness in high rails with tempered martensite or bainite microstructures, but were almost independent of hardness for pearlite in the range tested. Lubrication reduced the wear rates by up to two orders of magnitude for all microstructures. It is concluded that pearlite gives the best dry wear performance, and there is no advantage in increasing hardness beyond HRC 38-40. The superior performance of pearlite in dry wear appears to be due to a very pronounced work hardening near the wearing surface. Electron microscopy reveals a marked refinement in the pearlite microstructure near the wearing surface, and this may explain the high work hardening observed.

* National Research Council of Canada, 3904 West 4th Avenue, Vancouver, B.C., CANADA V6R 1P5

+ Physical Metallurgy Research Laboratories, 568 Booth Street, Ottawa, Ontario, CANADA K1A 0G1

** Technical University of Nova Scotia, Mining and Metallurgy, 1360 Barrington Street, Halifax, N.S., CANADA B3J 2X4

INTRODUCTION

It is generally believed that increasing rail hardness and strength increases rail wear resistance. This belief is substantiated by test data from N. American and Australian Railways[1-4] and is reflected in the many studies done to develop high strength steels for premium rail by the accelerated cooling[5-7] and alloying[8-10] of basically standard C-Mn eutectoid compositions. The most frequent cause of high (or outer) rail replacement on curves is gauge-face wear and this increases with increasing axle load and lateral creepage (decreasing curve radius). Thus Roney's[11] 1982 review on the economic aspects of wear on Canadian Railways states that:

i) the great majority of replacement rails scheduled for 1982 will be laid in the heavy tonnage, high curvature regions of main-line track and

ii) a significant percentage of replacement rails will have superior strength and hardness to rails replaced.

Current premium rails range in hardness from ~HRC 36-39 (HV 354-382). It is thought by some rail manufacturers and users that increasing the hardness to HRC 43-45 (HV 423-446) may further significantly reduce wear rate and be economically viable. However, preliminary, full-scale results[12] obtained under controlled conditions at the Facility for Accelerated Service Testing (FAST), Pueblo, Colorado, suggest that wear resistance only increases slowly with increasing hardness from HRC 37 (HV 363) to HRC 39.5 (HV387). Similar results were obtained by Hodgson et al[13]. It was therefore considered desirable to investigate the effects of three hardness levels, HRC 38, 42, 45 (HV 372, 412,

446) on the wear rate of one particular steel to determine whether the production of very hard rails is actually economically justifiable. Furthermore, although studies[14-16] of the effect of microstructure on wear resistance indicate that fine pearlite is superior to bainite or tempered martensite, the hardnesses examined were lower than those proposed in the present work. Hence, the scope of the experiments undertaken was expanded to include the testing of bainite and tempered martensite as well as pearlite.

EXPERIMENTAL PROCEDURE

Test Rig

Wear and contact fatigue tests were carried out on a disk-on-disk rail/wheel wear apparatus designed to simulate the interaction between a railway wheelset and a pair of rails. The rails were modelled by disks, 69.9 mm in diameter, fabricated from the heads of full size rail. The crown of each disk was machined to a new 67.5 $kg.m^{-1}$ (136 lb. yd^{-1}) AREA profile using a numerically controlled lathe. The wheelset was modelled by disks 120.7 mm in diameter at the centre of the tread, machined to a worn wheel profile designated "CN Profile A", and rigidly mounted on a shaft. Both rail and wheel profiles were reduced ten times in cross section. The test rig has been described in detail by Kalousek (18, 23).

The orthogonal components of the load vector transmitted to the rail disks were measured by load cells. The distribution of forces between flange and tread contacts, occurring between disks representing the high (outer) wheel and rail in a curve was determined by computation[17]. The wheelset loading was selected to yield Hertzian contact stresses of a magnitude representative of field conditions. The maximum Hertzian pressure P_o between worn rail statically loaded by a laden car with worn wheels, on a tangent track, is approximately 830 MPa. However, the contact stresses which occur in curves are much higher. Considering the contact between the wheel's flange root and the gauge side of the high rail or between the wheel's false flange and the field side of the low rail, the calculated range for P_o is between 1 500 and 3 000 MPa. To simulate these high values of P_o, the wheelset load during all tests was 7 000 N (1 570 lbf) yielding P_o = 1 800 MPa (261 ksi) for the case of two symmetrically loaded contact areas. This load and the resulting P_o produced a work hardened layer in the rail disk equivalent to that observed in a full scale rail.

Materials

All wear blanks were machined from the rail-head of an experimental Cr-Mo rail, austenitized at 1 025°C and isothermally transformed in a salt bath. The steel was of composition 0.72% C, 0.81% Mn, 0.28% Si, 0.022% S, 0.79% Cr, 0.21% Mo and transformation temperatures were 625°C (HRC 38), 595°C (HRC 42) and 575°C (HRC 45) for pearlite and 460°C (HRC 38), 415°C (HRC 42)and 375°C (HRC 45) for bainite. Transformation details are given by Fegredo et al[19] and the isothermal transformation temperature diagram of this steel is also given by Stone[1]. However, because of random Mo segregation and the corresponding localized increase in hardenability, some martensite streaks appeared in the upper bainite disks of hardness HRC 38 (HV 372). This occurred even though longer transformation times were generally imposed than those determined by the isothermal transformation experiments[1,19].Tempered martensite microstructures were obtained by austenitizing at 1025°C, oil-quenching and then tempering the blanks for 1 hour at 510°C (HRC 45), 566°C (HRC 42) and 616°C(HRC 38).

All wheel disks were made from AAR Class C wheel steel, having the same chemical composition as plain carbon rail (similar to 1070 steel) and hardness HRC 38 (HV 372).

Wear Tests

"Full sequence" tests consisted of sixty periods of 40 000 revolutions of the rail disks. Within each period, the yaw misalignment was altered to apply angles of attack of 10', 18', 32' and 40' successively, for 2 500 revolutions each. These angles represent the mean yaw misalignment measured on the trailing and leading axles, of trailing and leading freight car trucks, respectively, in a curve of 235 m radius (8° curve)[20]. The angles of attack were next decreased successively, to complete a total of 20 000 revolutions. The machine was then stopped, the direction of disk rotation reversed and the yaw angles changed from positive to negative values to maintain the same orientation of curvature. A second sequence of 20 000 revolutions was run in this manner to complete a period of 40 000 revolutions. Each period was roughly equivalent to 10^6 gross tons (1MGT) of service for rails laid in a 235 m radius curve in single main line track and experiencing heavy axle load traffic in both directions. The sixty periods were applied as follows:

1) One period run dry at an ambient temperature of 18°C and 45% relative humidity. The disk surfaces were contaminated by oxidized wear debris generated during the course of this period. Rail disk speed, 250 RPM.

2) Nineteen periods, lubricated by a calcium soap base grease containing mineral oil, having a viscosity at atmospheric pressure of 0.02 Nsm^{-2}, 11% graphite and 2.5% MoS_2, added by the manufacturer as an EP additive. In addition, 20% of sand was added during the test to simulate the dispensation of sand by locomotives. The limiting coefficient of friction for this type of boundary lubrication was typically 0.18. Rail disk speed, 500 RPM.

3) Disks were cleaned and step 1 repeated.

4. The final 39 periods were run as in step 2, but with pure grease (no sand). It was found by experience that a small quantity of grease, when transferred from a reservoir, to each rail/wheel pair every 4 000 revolutions, remained from application to application. The grease was, however, contaminated by wear particles, yielding a boundary lubrication regime with a limiting coefficient of friction in the range 0.09 - 0.12. This grease-only lubrication regime, although less typical of field conditions than the grease/sand lubrication, was used to enhance the rate of contact fatigue damage to the rail disk.

Wear was measured by removing both rail disks periodically and weighing them. At the same time, disk profiles were obtained with a precision of ± 2 µm using an electronic profilometer. The superposition of profiles taken before, during and after the test helped to identify the locations from which metal was removed and the locations to which metal was displaced due to plastic flow.

In addition to full-sequence tests as described, one pair of pearlite disks and one pair of tempered martensite disks were subjected to two periods of dry wear only. Table 1 summarizes the materials and the test sequences used.

Metallography

Transverse sections were cut from the worn disks, nickel plated for edge retention, and polished and etched using standard techniques for both optical and SEM observations. Microhardness measurements were made with a diamond pyramid indentor at a load of 100 grams (0.98 N).

An image analyser (Cambridge Instruments Quantimet 900) was employed to measure the number and length of "cracks" within 150 µm depth from the Ni-steel interface on transverse sections from four high-rail disks. The features counted by the Quantimet were surface cracks and cracks at deformed inclusions, principally MnS, within the disk. Features less than 10 µm were not counted and a horizontal amender was used so that features within 10 µm of each other in the same length direction were joined and considered as one feature. However, only a few were joined.

To obtain thin foils for TEM at the worn surfaces and at known distances below the surface, transverse samples were again cut from the worn disks, and electroplated with nickel for edge preservation.

Disks were cut from the plated samples, mechanically thinned and finally jet-polished, to obtain a perforation and thin area as close as possible to the sample/Ni interface.

OBSERVATIONS

Wear Tests

Wear Rates. Wear rates of the different microstructures and hardnesses are given in Figure 1 for the three environments employed. The following points are apparent:

i) The wear rate of the high rail disk decreases with increasing hardness in dry wear for tempered martensite and bainite structures but not significantly for pearlite.

ii) The high rail disk microstructures can be rated in the following order of decreasing dry wear resistance: pearlite, bainite, tempered martensite. In particular, tempered martensite of hardness HRC 38 wears roughly 10 times faster in dry wear than pearlite of HRC 38.

iii) All low rail disks have similar dry wear rates which are significantly lower than those for high rail disks. Thus, microstructure and hardness appear to have little effect on low rail dry wear rates.

iv) Wear rates are markedly lower in a grease-20% sand environment than in dry wear for both high and low rail disks (note the different wear rate scales on figures 1a, b and c) with low rail disks wearing somewhat faster than corresponding high rail disks. Microstructure and hardness do not appear to have a significant effect on wear rate. (Note - it should be mentioned that the disks representing wheels had to be changed after the first dry wear test (1st period) for the upper bainite disks "D" of hardness HRC 38. This may account for the relatively high wear rate shown in Figure 1a.

v) Wear rates in a pure grease (fully lubricated) environment are considerably lower than in grease-sand. Again, microstructure and hardness do not play significant roles in deciding wear performance but high rail disks consistently wear faster than corresponding low rail disks. The wear rate of the tempered martensite high rail disk A-HR is almost 3 orders of magnitude lower in fully lubricated than in dry wear.

Wear Profiles. The wear profiles determined after each of the four wear stages are shown in Figure 2 for the high and low rail disks of the three microstructures of hardness HRC 38 (A, D, G). Very little change is visible between the end of the second "no lub.run" (step 3) and the end of the "grease only" run (step 4), consistent with the very low wear rates shown in Figure 1c. All low rail disks appear to behave similarly but a marked difference occurs between the pearlite (G-HR) and the bainite and tempered martensite (D-HR and A-HR) profile changes. The latter develop pronounced shoulders through wear-attrition at the lower end of the gauge-face while the

TABLE 1

Summary of Materials and Test Sequences

Specimen Code	Micro-Structure	Approx. Hardness (HRC)	Type of Test
A-HR (high rail) -LR (low rail)	Tempered Martensite	38	Full sequence (2,400,000 revs)
B-HR -LR	" "	42	" "
C-HR LR	" "	45	" "
D-HR -LR	Bainite	38	Full sequence (2,400,000 revs)
E-HR -LR	" "	42	" "
F-HR -LR	" "	45	" "
G-HR -LR	Pearlite	38	Full sequence (2,400,000 revs)
H-HR -LR	" "	42	" "
I-HR -LR	" "	45	" "
J-HR -LR	Pearlite	38	Dry (80 000 revs)
K-HR -LR	Tempered Martensite	38	Dry (80 000 revs)

pearlite disk develops a shear lip which forms by metal flow. The large profile change for disk D-HR in grease-sand is connected with the relatively high wear rate mentioned above. Comparable profile changes are seen in the region between the centre of the running surface and field corner.

Profile changes for disks of higher hardness were similar to those seen for the tempered martensite and pearlite disks of hardness HRC 38. Thus, shoulders and shear lips developed in the tempered martensite (B-HR and C-HR) and pearlite (H-HR and I-HR) disks respectively although the extent of the profile changes reflected the respective wear rates. However, the bainitic disks E-HR and F-HR developed shear lips on the gauge-face instead of shoulders possibly reflecting their improved dry wear resistances.

Metallography

Optical and SEM. A survey of transverse sections shows that a severely deformed sheared layer exists at the wear surface of all disks. The deformation pattern indicates that high lateral creep forces are imposed, as expected, which produce a pattern of deformation very similar to that observed in full-scale rails on curves (cf Ghonem et al.[21]). The approximate depths of gross shear deformation, at different locations, are given in Table 2 for all high rail disks and these increase from 0 μm at the field corner to several hundred μm at and near the gauge corner. The values obtained for J-HR (dry wear) are similar to those of G-HR (full sequence) but much higher values are obtained for K-HR (dry wear) than for A-HR (full sequence). Note that these values are somewhat subjective, and vary with the precise location chosen around the worn surface periphery. Similarly, microhardness values obtained on worn disks depend on the precise location of the traverse (cf. Figures 9 and 10). Only relatively shallow shear layers were observed on low-rail disks, of the same order as those given in Table 2 for the centre of the running surface, and deepest at the centre of the running surface.

The SEM micrographs presented herein concentrate on typical pearlitic and tempered martensite microstructures which gave the extreme wear rates.

Figure 3 shows the gauge corner deformation observed in disks K-HR and J-HR. Note the shoulder which has developed on disk K-HR, compared to the shear lip on disk J-HR (arrows). The depth of gross deformation is more easily seen in the pearlite sample, J-HR.

TABLE 2

Approximate Depth (μm) of Grossly Deformed Shear Zone in High Rails From the Worn Surface to Where the Grains Become Just Recognisable

Disk	Centre of gauge face	Centre of gauge corner	Junction of running surface & gauge corner	Centre of running surface	Junction of running surface & field corner
A-HR	25	270	250	70	0
B-HR	25	225	250	40	0
C-HR	15	315	340	50	0
D-HR	25	450	450	55	10
E-HR	25	280	405	55	0
F-HR	15	270	180	55	0
G-HR	40	260	295	80	0
H-HR	45	205	215	55	10
I-HR	35	150	160	45	0
J-HR	25	280	295	75	0
K-HR	25	495	675	235	0

Figures 4a-4d show gauge corner deformation typical of all high-rails tested. The numerous cracks which are apparent in these micrographs were usually associated with MnS inclusions. Both the numbers and lengths of the cracks observed varied systematically with the microstructure and with the test conditions, although all samples were fabricated from the same steel, and should thus have the same number of MnS inclusions. Figure 5 shows image analyser data giving feature (crack) frequency vs. length of feature. These data were obtained from fields covering the gauge face, gauge corner and about a quarter of the width of the running surface, where most wear takes place. The measurements confirm what is seen qualitatively in the micrographs, that more and longer cracks are generated in dry wear in tempered martensite than in pearlite, and that subsequent lubricated service (eg. the full sequence tests) results in fewer cracks. Presumably, some of the cracked surface layers are worn off, and then fewer cracks are generated due to the lower lateral creepage forces in lubricated operation.

Figure 6 shows the association of cracks with inclusions in more detail. Figure 6c shows that un-deformed oxide inclusions (Al, Si, Ca, Mn oxide) were also associated with micro-cracks, although these were much less frequently observed.

At higher magnifications, the effect of deformation on the microstructure, and especially on the carbide morphology and spacing, becomes more apparent. Figure 7 shows the original microstructures which developed. The very fine carbide spacing developed in the pearlite samples, J-HR and G-HR, compared to that resulting in the tempered martensite samples, is remarkable. The microstructure developed in the bainite disk, D-HR, is intermediate between the pearlite and tempered martensite full-sequence disks. A bainitic microstructure was not subjected to a dry-wear-only test.

Low rail disks showed much shallower regions of gross deformation, and fewer cracks.

Microhardness Measurements. All high-rail and low-rail disks tested were subjected to microhardness tests, and the results shown in Figure 9 are typical. As mentioned above, the microhardness values obtained are quite sensitive to the location of the microhardness traverse. A second set of microhardness values was taken at the gauge corners of samples K-HR and J-HR to correlate with TEM observations (see below). These data are shown in Figure 10, where it can be seen that higher hardnesses are observed near the surface of disk J-HR than those shown in Figure 9. The values obtained for disk K-HR are comparable. In general, the following points are observed:

i) The specimens are hardest at and very close to the worn surface. Hardness decreases with increrasing depth and generally approaches the hardness of the undeformed microstructure at between 50 and 250 μm.

ii) The highest values are obtained at the gauge corner.

iii) The specimens subjected to dry wear only, i.e. J-HR and K-HR, have the highest hardness and the pearlitic specimen J-HR is consistently harder than the tempered martensite specimen K-HR at and near the worn surface. In particular, extremely high values of HV_{100} 750-919 (HRC 62-67) are obtained for J-HR at the worn surface in the centre of the gauge corner and this level of hardness persists for at least 50 μm.

iv) The bainite disk D-HR consistently hardens less than the tempered martensite (A-HR) and pearlite (G-HR) disks for full sequence test specimens.

Hardness values are given in Table 3(a) for high rail disks of undeformed hardness HRC 45. Their hardness pattern parallels that in Figure 9 as higher hardness values are obtained at the running surface and gauge corner than at the gauge-face. A comparison between Table 3(a) and Figure 9 shows that it is only at the centre of the running surface that C-HR (tempered martensite) and F-HR (bainite) are much harder than A-HR and D-HR respectively at depths between 0 and 25 μm. Otherwise, hardness values shown in Table 3(a) appear to reflect the higher intrinsic hardness of these disks and indeed, gauge-face values are quite low for disk 1-HR (pearlite) in Table 3(a), lower than the corresponding pearlite disk G-HR (Figure 9) at the worn surface.

Table 3(b) shows that the hardest values of the low rail disks are produced at the worn surface for the dry wear specimens J-LR and K-LR, but these disks have similar hardness values to the others beneath the surface. Comparisons between disks of similar microstructure but different undeformed hardness, i.e. A-LR and C-LR, D-LR and F-LR, G-LR and I-LR show that they undergo more or less the same degree of work hardening.

TEM. Thin foils for transmision electron microscopy were prepared from all disks subjected to the full-sequence wear test, and in addition, 2-stage carbon replicas were prepared from polished and etched sections of samples J-HR and K-HR. A much lighter etch was used for the samples to be replicated than for the samples examined in the SEM (above). The principal results are:

i) there is significant deformation of the cementite in the bainitic and pearlitic disks, near the surface, but little if any deformation of the cementite in the tempered martensite disks.

ii) in agreement with SEM results, significant refinement of the carbide spacing is observed near the worn surface, especially for the pearlite (cf. Figure 8).

iii) there is a very great refinement of ferrite grain size near the worn surface.

iv) a texture is observed in the near-surface region of all specimens. This is manifested by a weak or absent 200 ferrite diffraction ring, suggesting a <111> wire texture.

Figure 11 shows a region of disk H-HR, 30 μm below the running surface. Very fine, unbroken cementite lamellae are seen, with individual spacings as small as 20 nm, demonstrating that there has been deformation of the cementite. The rings on the diffraction pattern, from a region 3.5 μm in diameter, show that the grain size is much finer than 3.5 m, and the weak 200 ring suggests texture.

Figure 12 shows a thin foil from disk E-HR, between the gauge corner and the centre of the running surface. The interface between the sample surface and the Ni electrodeposit is clear. The dark field micrograph, Figure 12b, shows the extremely fine grains which have developed, as does the smoothness of the diffraction rings in Figure 12c, where an aperture defining a selected area of only 0.9 μm was used. Again, there is the suggestion of texture, both in the weakness of the {200} ring, and in the presence of thickened regions on the {110} and {211} rings.

Figure 13 shows a region of disk A-HR, 70 μm below the running surface. A definite cell or fine grain structure has again developed in the ferrite, but not so fine as seen in the pearlitic (H-HR) or bainitic (E-HR) samples. Also, there is little suggestion of deformation of the cementite.

Figure 14 shows the refinement of the carbide spacing near the surface, as well as some break-up of cementite lamellae in the pearlite sample, near the surface. Very little deformation of the carbides in the tempered martensite is seen. Inter-particle spacings were measured on numerous such micrographs, and the results are plotted in Figure 15. For interlamellar spacings in the pearlite, a simple linear intercept measure was used, since the structure was well aligned near the surface. At greater depths, below the region of gross deformation referred to above, the test line was maintained normal to the lamellae as seen on the replica, and the narrowest spacings only were measured, to ensure that only lamellae nearly perpendicular to the replicas were considered. This procedure was adopted since, at the high magnification required to clearly resolve the lamellae, insufficient colonies were seen in any one field to permit the use of statistical techniques such as suggested by Underwood[22]. For the tempered martensite carbide spacings, the formula:

$$\lambda = \frac{(1 - V_V)}{N_L}$$

TABLE 3

Hardness (HV_{100}) at various depths (μm) below the worn surface for different locations

(a) High Rail Disks

Disk	Hardness for 0 to 250 μm depths						
	0	5	10	15	25	50	250
Centre of running surface							
C-HR	650	608	608	608	590	425	363
F-HR	590	590	590	496	420	378	360
I-HR	470	410	380	370	350	354	376
Centre of gauge corner							
C-HR	579	640	590	579	540	483	446
F-HR	500	530	530	549	510	560	371
I-HR	608	608	510	510	470	519	417
Centre of gauge face							
C-HR	470	490	450	430	410	405	405
F-HR	450	530	400	390	360	380	370
I-HR	390	360	350	350	350	394	376

(b) Low Rail Disks

Disk	Hardness at centre of running surface for 0-250 μm depths						
	0	5	10	15	25	50	250
A-LR	540	540	540	540	480	405	351
C-LR	590	579	608	590	590	437	433
D-LR	530	510	490	480	450	394	376
F-LR	530	530	530	490	460	387	370
G-LR	608	590	579	579	450	425	370
I-LR	560	579	579	560	540	405	345
J-LR	620	572	623	604	509	441	371
K-LR	627	567	528	539	538	442	360

given by Underwood[22] was used. Here,

λ is inter-particle distance

V_v is volume fraction of particles (obtained from point counts on the replicas)

N_L is the number of interceptions of particles, per unit length of test line

Comparing Figures 10 and 15, it is apparent that high hardness is associated with fine carbide spacing.

DISCUSSION

Full-scale rail wear tests are enormously expensive and time consuming. Thus, a laboratory-scale test which correlates well with field data is of particular interest. The tests used in the present work are similar to those done by Kalousek et al[24] on specimens machined from seven different commercially available standard and premium rails. The rails had also been subjected to full-scale tests[12,15] on the FAST track. Using the Figure of Merit (FM) criterion proposed by Steele and Reiff[24] as a measure of gauge face wear resistance, very similar FM ratios were obtained in both laboratory- and full-scale tests of head-hardened, fully heat-treated and standard rail steels indicating a a good correlation between laboratory an field results.

In the present work, tempered martensite, bainite and pearlite have been examined in the hardness range HRC 38-45. Both tempered martensite and bainite show improved dry wear resistance with increasing hardness but the dry wear resistance of pearlite is esentially independent of hardness. Furthermore, pearlite has the highest wear resistance, Fig. 1(a). Since increasing hardness decreases fracture toughness these results satisfy both experimental objectives, i.e., to determine the best microstructure and the maximum useful hardness. We conclude that (a) fine pearlite should continue to be used in premium rails in preference to tempered martensite or bainite and (b) no useful purpose is served in achieving a hardness beyond HRC 38-40.

The reduction of friction coefficients to 0.18 and 0.09-0.12 by grease-sand and pure grease lubrication respectively, markedly decreases wear rates in all microstructures. The pure grease run follows one period (40k revs) of dry wear in the full sequence tests. This means that stress systems in the lubricated environment are imposed on a cracked surface characteristic of dry wear.

The maximum shear stress occurs at or below the surface, depending on whether the friction coefficient is greater or less than 0.32[25]. Beagley[26] has pointed out that fatigue cracking and rail shelling result when the maximum shear stress occurs below the surface and the loads are sufficiently high. The examination of wear debris released during the pure grease run in similar full sequence tests on pearlitic steels by Kalousek et al.[23] has shown that most of the flakes were over 1 000 times the weight loss/cycle. Thus, slow sub-surface fatigue crack propagation and crack amalgamation of the pre-cracked (by dry wear) specimens must occur over many revolutions before large flakes drop off. However, the results shown in Table 3 do imply an absence of deep shelling in our disks under the test conditions.

Low rails have significantly smaller wear rates than corresponding high rails under dry wear or pure grease regimes. The hardness/dry wear rate relations of the three microstructures somewhat parallel those of the high rails. The analysis of wheel/rail contact conditions is outside the scope of this paper, however, Kalousek et al. concluded[23] from an examination of wear profiles and wear debris that the difference in dry wear rates between low and high rails can be attributed to difference in wear in the vicinity of the gauge corner. Thus, since gauge face wear does not occur in low rails, Fig. 2, and the depth of the grossly deformed shear layer at the centre of the running surface is fairly similar to that in high rails, Table 2, wear rates observed in low rails are much less than those observed in high rails.

High work hardening occurs at and near the surface of the worn high rail disks, as shown in Figures 9 and 10, and Table 3. The greatest hardness values are found in dry wear and at the gauge corner, where the greatest amount of gross deformation is observed. Many surface and subsurface cracks are seen within the deformed subsurface layer, especially in the vicinity of the gauge corner (Fig. 4), so that measured hardness values may in fact be conservative if cracks are near the indentor.

The deformability of MnS is well known together with its adverse effect on toughness and Bolton and Clayton[27] have recently postulated that flaking in their Type 1 dry wear mode is due to deformed MnS inclusions. Using XES, we have observed that MnS is associated with many or most of the thin subsurface cracks, suggesting that these cracks mainly initiate at deformed MnS within the grossly deformed shear layer. The MnS inclusion/steel interface is very weak so that the inclusion periphery is basically a crack whose aspect ratio increases with increasing deformation on repeated cycling and as the inclusion moves nearer to the surface. Interfacial cracks are also seen at comparatively undeformed oxide inclusions, Fig. 6(c). These are less common and the cracks formed have lower aspect ratios.

Now consider the disks of hardness HRC 38 for which the greatest differences were found in dry wear rate. Quantimet measurements, which were made to a depth of 150 μm, show that the total crack length in dry wear is much greater in tempered martensite than in pearlite, Fig. 5.

Further, comparing data from Table 2 and from Figures 1, 9 and 10 we see that for dry wear (or also for the full sequence tests), we may associate on the one hand, good dry wear performance with a high degree of work hardening, a shallow depth of gross deformation and low total crack length. On the other hand, we correlate inferior dry wear performance with lesser work hardening, greater depth of gross deformation and longer total crack length. Thus, we conclude that it is not so much the initial hardness, but rather the degree of work hardening exhibited by the rail which controls its dry wear performance.

The reason for the higher degree of work hardening exhibited by the pearlite would appear to lie in the different morphology of the carbides in the two microstructures. In the pearlite, the cementite is present as lamellae with a high aspect ratio, or a large surface to volume ratio. Thus, shears in the ferrite are effectively transferred to the cementite, which deforms with the ferrite to produce a very fine lamellar structure, as shown in figures 11 and 14. Langford[28] has studied the refinement of pearlite in wire drawing, and the correlation between pearlite spacing and strength. He concluded that:

$$\sigma = \sigma_0 + 0.35\,\alpha G \left(\frac{b_{cm}}{d}\right)^{\frac{1}{2}} + \alpha G \left(\frac{b}{d}\right)$$

where G is the geometric mean of the shear moduli of ferrite and cementite, 7.7×10^4 MPa, b_{cm} is the Burgers vector in cementite, 0.225 nm, b is the Burgers vector in ferrite, 0.248 nm, α is a constant approximately equal to 0.7, and d is the pearlite spacing. If d is set equal to 20 - 30 nm, the finest spacings observed in figure 13, then Langford's equation allows us to estimate a maximum microhardness of HV 900 - 1000, as observed (figure 10).

In the tempered martensite, on the other hand, the cementite occurs as spheroidal particles, with relatively small surface areas. Thus, shear stresses in the ferrite are not transferred effectively to the cementite, which does not then deform. Although a refinement of the microstructure occurs, including a refinement of the grain size, the carbides are

unable to reinforce the ferrite matrix as they do in pearlite, so that the same degree of work hardening is not observed. Thus, the pearlite hardens more effectively, leading to a smaller zone of gross shear deformation, smaller total crack length, and better wear properties. The bainite, where the carbide morphology is intermediate between that of pearlite or tempered martensite, gives an intermediate wear performance.

SUMMARY AND CONCLUSIONS

1. In the hardness range HRC 38-45, the wear rate depends strongly on initial hardness for tempered martensite, moderately so for bainite and very little, if at all, for pearlite. Lower wear rates are obtained for all pearlites than for tempered martensite or bainite of hardness HRC 45. The dry wear rates of low rails are significantly less than those for corresponding high rails. Their dependence on hardness is relatively small.

2. Lubrication, particularly with pure grease, decreases the wear rates of high rails very significantly but has a lesser effect for low rails. In general, little correlation exists between lubricated wear rates and either hardness or microstructure, however, the wear rate of pearlite appears to increase with increasing hardness.

3. A highly sheared layer is produced at the worn surface, whose depth is a maximum (> 250 m) at the gauge corner. High microhardness values are obtained at and within 50 m of the worn surface, particularly in dry wear. The hardest values occur at the surface of the gauge corner and for pearlite. These microhardness values rather than the initial hardness of the steel, appear to control dry wear resistance.

4. Surface and sub-surface cracks occur in the deformed shear zone and are intimately associated with inclusions, particularly MnS.

5. TEM examination of worn surfaces shows a considerable refinement of the inter-carbide spacing, especially for pearlite, and the formation of very fine, poly-crystalline ferrite grains. Diffraction patterns show that a strong possibility exists of texture formation.

On the basis of the above results it appears that pearlite of hardness HRC 38-40 is the optimum microstructure for this steel. Lowering the sulphur content should markedly lower dry wear rate and this aspect is being investigated. All wear rates decrease drastically under lubrication to insignificant values. With the present test conditions, deep contact fatigue cracks or severe shells were not obtained but their possibility does exist for longer lubricated testing.

ACKNOWLEDGEMENTS

It is a pleasure to acknowledge the assistance of the following: Mr. L. Clements heat-treated the wear blanks, Mr. E.F. Connors prepared metallographic specimens, Mr. V. Chartrand took the SEM micrographs and Dr. M.T. Shehata and Mr. B. Casault did the Quantimet analysis. Mrs. C. MacDonald prepared thin foils for TEM and the replica work was done by Mr. P. LeBlanc during his tenure of a NSERC Undergraduate Summer Research Award at the Technical University of Nova Scotia. Financial support of the Transportation Development Centre towards machining of rail disks is greatfully acknowledged.

REFERENCES

1. Stone, D.H., Canadian Metallurgical Quarterly 21(1), 1982, pp. 17-24.
2. Kalousek, J., and Bethune, A.E., "Vanadium in Rail Steels," Proceedings of Seminar in Chicago: Organized by VANITEC, London, UK, EC1N 2NE, 1979, p. 63.
3. Gardiner, P.M., et al., "Evaluation of premium rail on 8° curves in the B.C. South Line," C.N. Rail Research Centre Report 152, St. Laurent, Quebec H4T 1K2, 1979.
4. Bramwell, S., and McElroy, T.F., Paper B6, 1st Internl. Heavy Haul Railways Conference Proc., Perth, Australia, Paper A4, Sept. 1978
5. United States Steel (1975) Railroad Facts, Technical Report No. 3.
6. Gino, T., et al., Iron and Steel Engineers, June 1975, pp. 25-31.
7. Ichinose, H., et al., Second International Heavy Haul Railways Conf. Proceedings, Paper 82-HH-19, Colorado Springs, USA, 1982, pp. 178-186.
8. Marich, S., and Curcio, P., Rail Steels, Development, Processing and Use, ASTM STP 644, Philadelphia, Pa., 1978, p. 167.
9. Smith, Y.E., and Fletcher, F.B., ibid. p. 212.
10. Vandium in Rail Steels: Proceedings of a Seminar In Chicago, Nov. 1979, VANITEC, London EC1M 2NE. See papers by H. Schmedders, p. 3; A.M. Sage et al., p. 12; S. Marich, p. 23; F.B. Fletcher et al., p. 41; P. Dilewijns et al., p. 48.
11. Roney, M.D., Contact Mechanics and Wear of Rail/Wheel Systems, Kalousek/Dukkipata/Gladwell (eds.), University of Waterloo Press, 1983, p. 271.
12. Steele, R.K., Canadian Metallurgical Quarterly 22(3), 1983, pp. 353-367.
13. Hodgson, W.H., et al., 2nd international Heavy Haul Railway Conference Proceedings, Colorado Springs 1982, Paper 82-HH-22, pp. 207-215.
14. Koerfer, E., written discussion to paper in Ref. 8, p. 202.
15. Musumoto, H., et al., 1st International Heavy Haul Railways Conference Proceedings, Perth, Australia, Session 212, Paper H.1.
16. Ichinose, H. et al., Ibid., Session 307, Paper 13.

17. Bradley, J., and Kalousek, J., "Modelling of Roller Ring Contact Forces for Three-Point Contact-Based on Kalkers Simplified Non-Linear Creep Theory for Single Point Contact," NRC Report LTR-WE-29 (in preparation).
18. Kalousek, J., Canadian Metallurgical Quarterly, 21, 1982, pp. 67-72.
19. Fegredo, D.M., et al., Canadian Metallurgical Quarterly, 22(3), 1983, pp. 385-395.
20. Kalousek, J. Rosval, G. and Ghonem, H., "Lateral Creepage and its Effect on Wear in Rail Wheel Interface," in Contact Mechanics and Wear of Rail/Wheel Systems. Kalousek, Dukkipata and Gladwell, eds., University of Waterloo Press, 1982.
21. Ghonem, H. Kalousek, J. Stone, D.H. and Dibble, D.W. "Observations of Rail Wear on Heavy Haul Railway Lines," in Contact Mechanics and Wear of Rail/Wheel Systems, Kalousek, Dukkipata and Gladwell, eds., University of Waterloo Press, 1982.
22. Underwood, E.E., "Application of Quantitative Metallography," in Metals Handbook, Vol. 8, 8th edition, ASM, 1973.
23. Kalousek, J., Ghonem, H., and Steele, R.K., "Wear and Lubrication Effect on Subsurface Failure of Several Steels," submitted to the 11th Leeds-Lyon Symposium on Tribology: Mixed Lubrication and Lubricated Wear.
24. Steele, R.K. and Reiff, R.P., Second International Heavy Haul Railway Conference Proceedings, Colorado Springs 1982, Paper 82-HH-24, pp. 115-161.
25. Johnson, K.L., and Jeffries, J.A., Symposium on Fatigue in Rolling Contact, Inst. Mech. Eng., London, 1963.
26. Beagley, T.M., Wear, 36, 1976, pp. 317-335.
27. Bolton, P.J., and Clayton, P., Wear 93(2) 1984 pp. 145-165.
28. Langford, G., Metallurgical Transactions A, 8A, 1977, pp. 861-875.

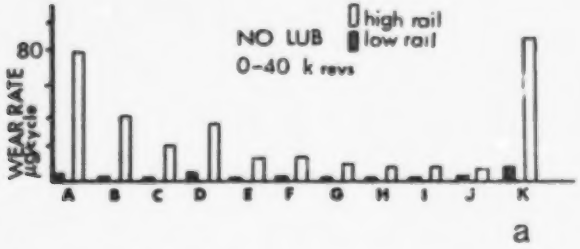

(a) no lubrication

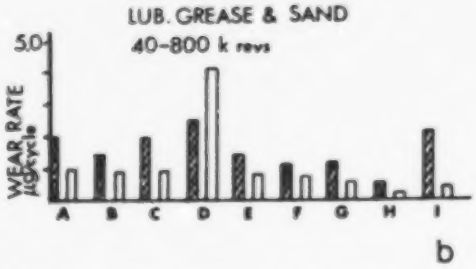

(b) grease/20% sand lubrication

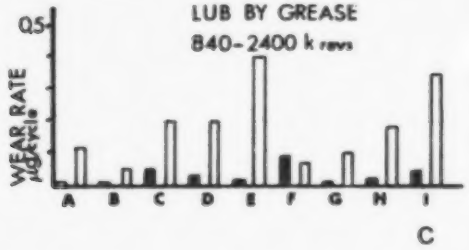

(c) pure grease lubrication

Figure 1: Wear rates observed.
Note scale changes in a, b and c.

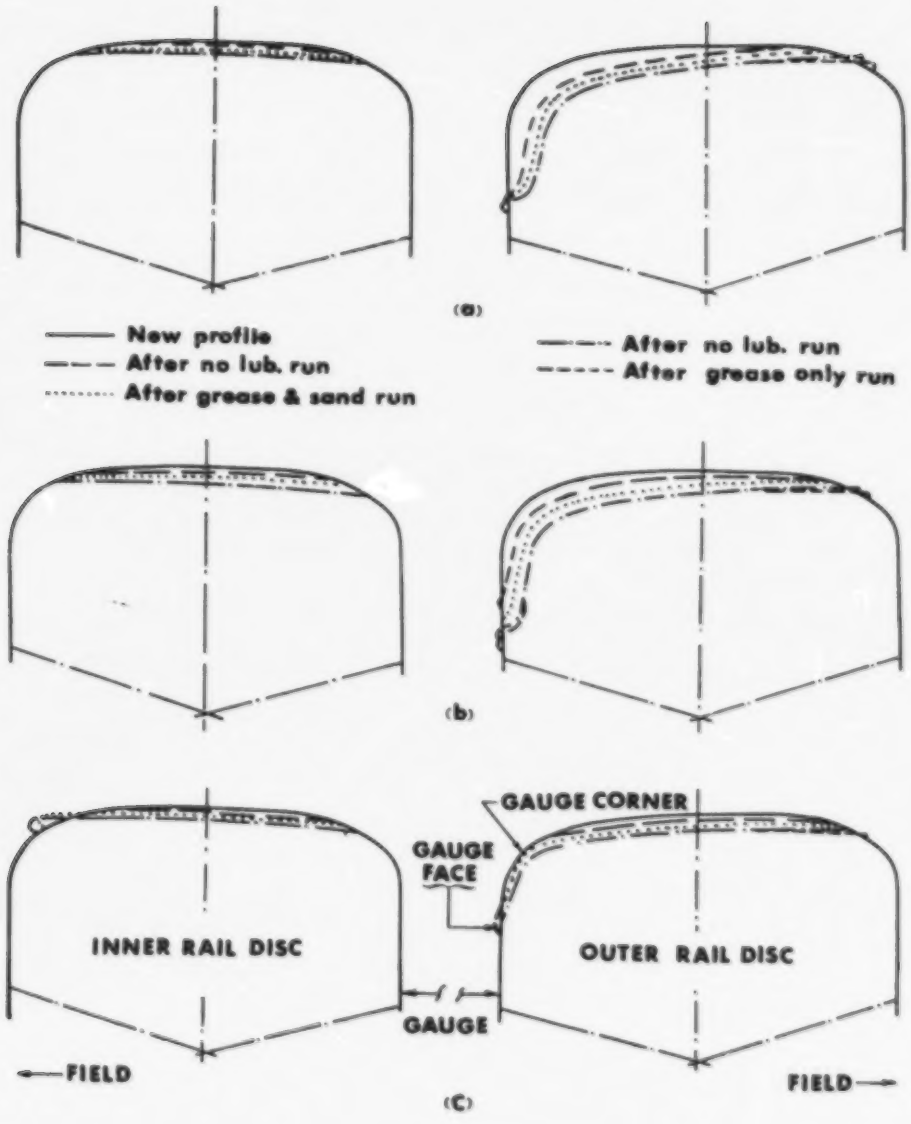

Figure 2: Wear profiles after each of the four test stages:
(a) disks A, tempered martensite
(b) disks D, bainite
(c) disks G, pearlite

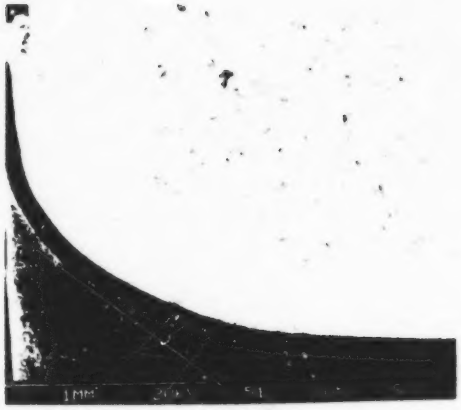

(a) disk K-HR, tempered martensite

(b) disk J-HR, pearlite

Figure 3: Gauge corner and gauge face wear after 2 periods of dry wear resulting in development of shoulder (a) or shear lip (b).

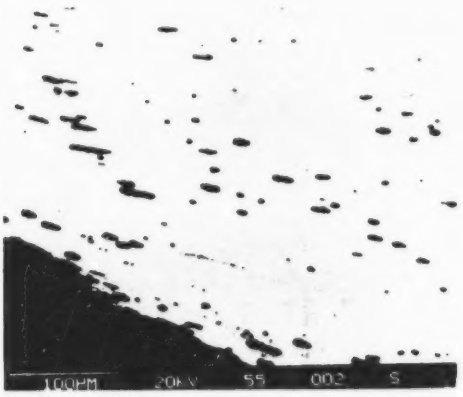

(a) Disk K-HR

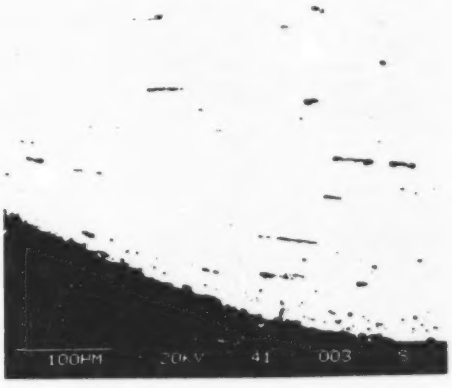

(b) Disk A-HR

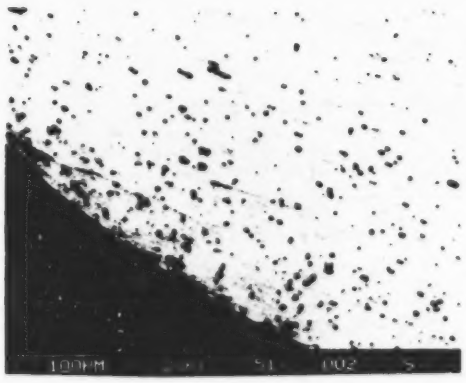

(c) Disk J-HR

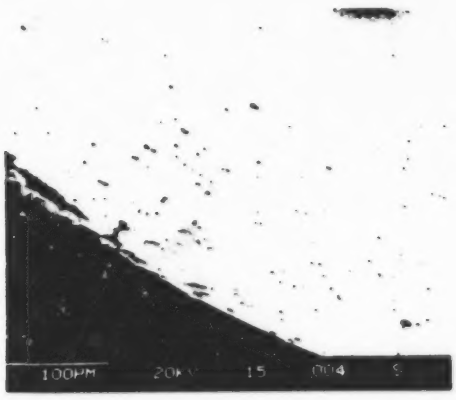

(d) Disk G-HR

Figure 4: Gauge corner deformation with surface and sub-surface cracks.

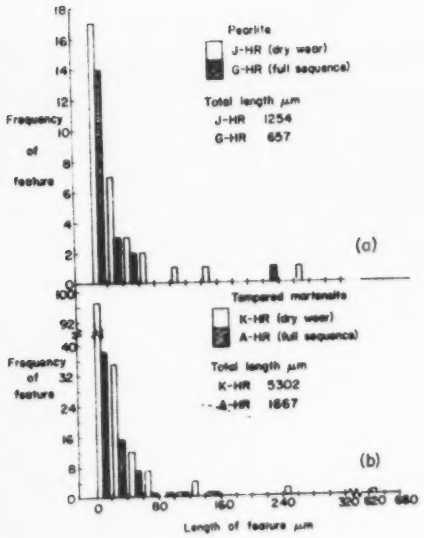

Figure 5: Crack frequency vs. length, image analyser data.

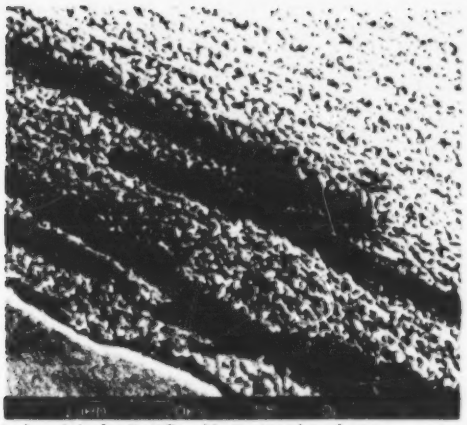

(a) Disk K-HR, MnS inclusions.

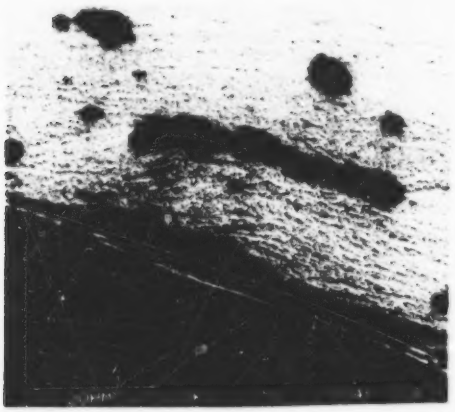

(b) Disk J-HR, MnS inclusions.

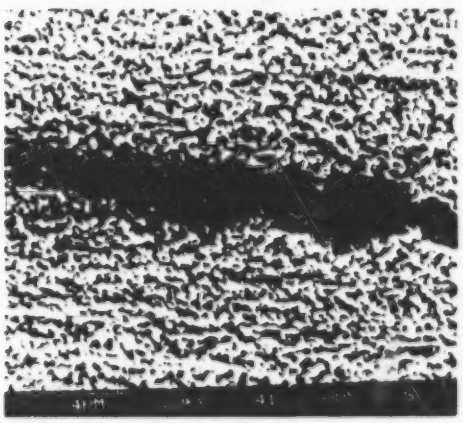

(c) Disk A-HR, undeformed oxide inclusions.

Figure 6: Association of cracks with inclusions.

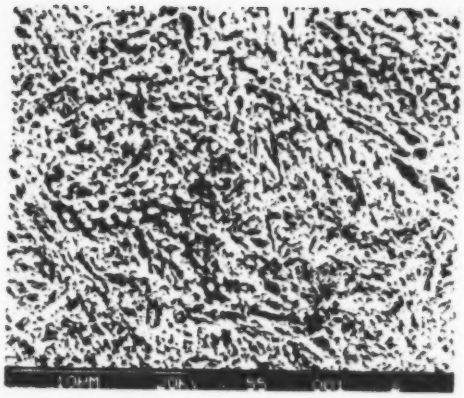

(a) Tempered martensite (Disk K-HR)

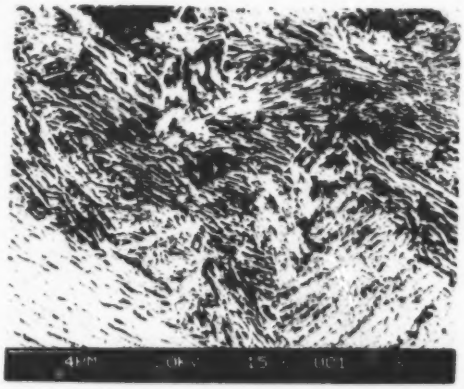

(b) Pearlite (Disk G-HR)

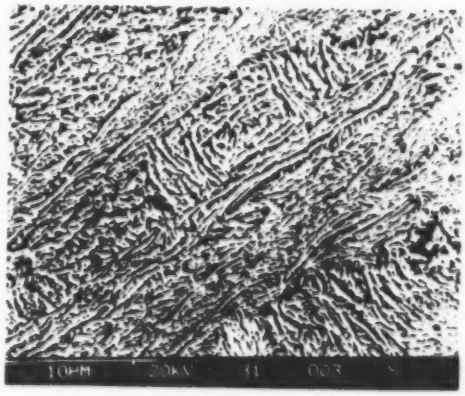

(c) Bainite (Disk D-HR)

Figure 7: Undeformed microstructures.

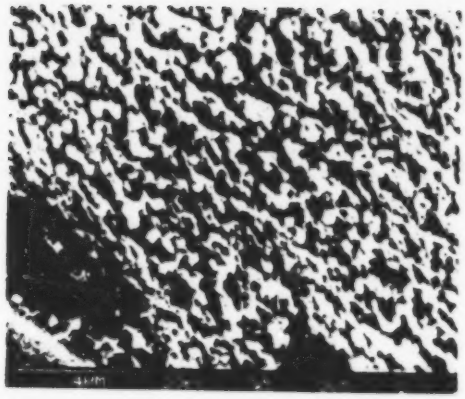

(a) Disk K-HR, dry wear

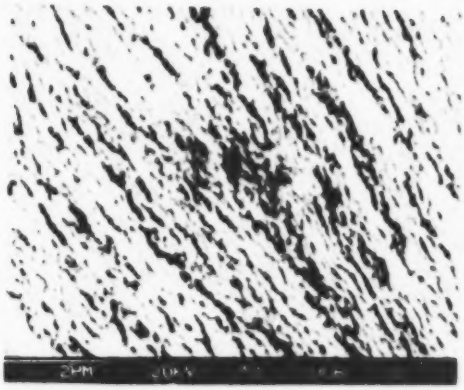

(b) Disk J-HR, dry wear

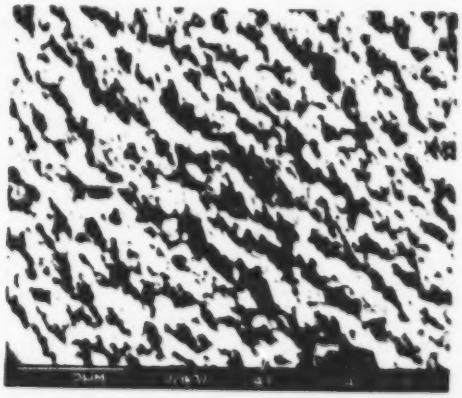

(c) Disk A-HR, full sequence.

Figure 8: Continued.

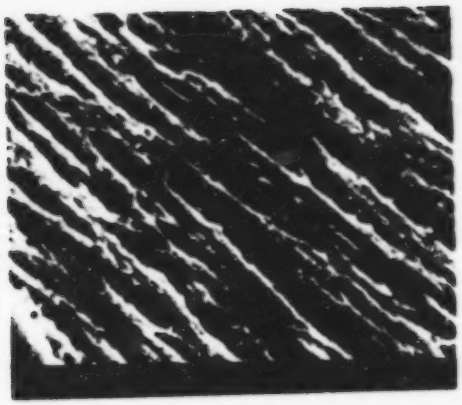

(d) Disk G-HR, full sequence

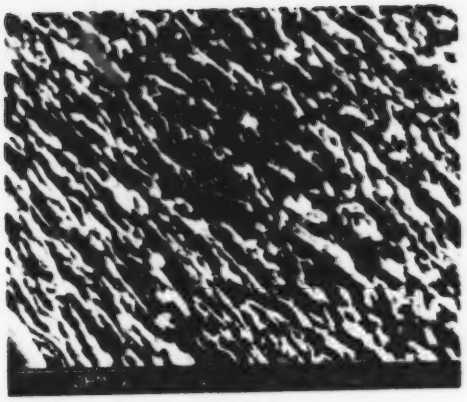

(e) Disk D-HR, full sequence

Figure 8: Worn near-surface microstructure.

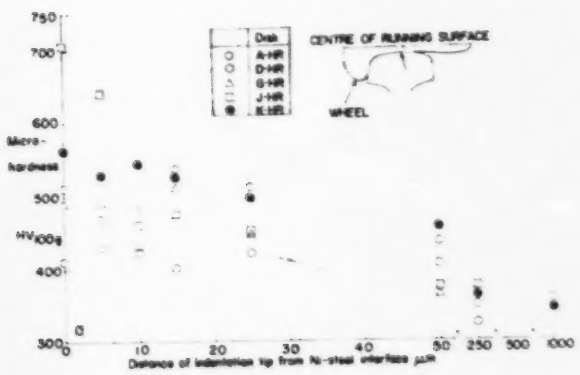

(a)

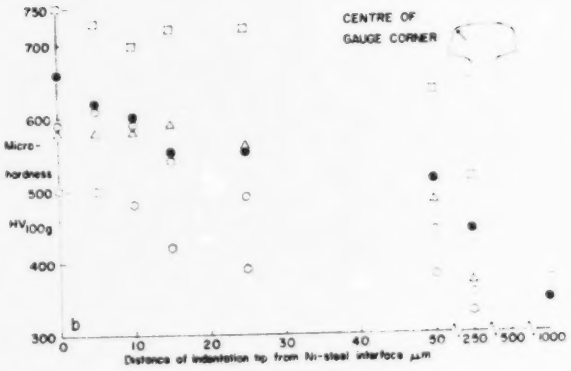

(b)

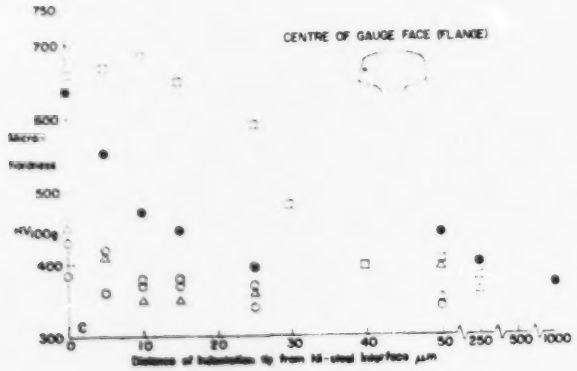

(c)

Figure 9: Typical microhardness traverses.

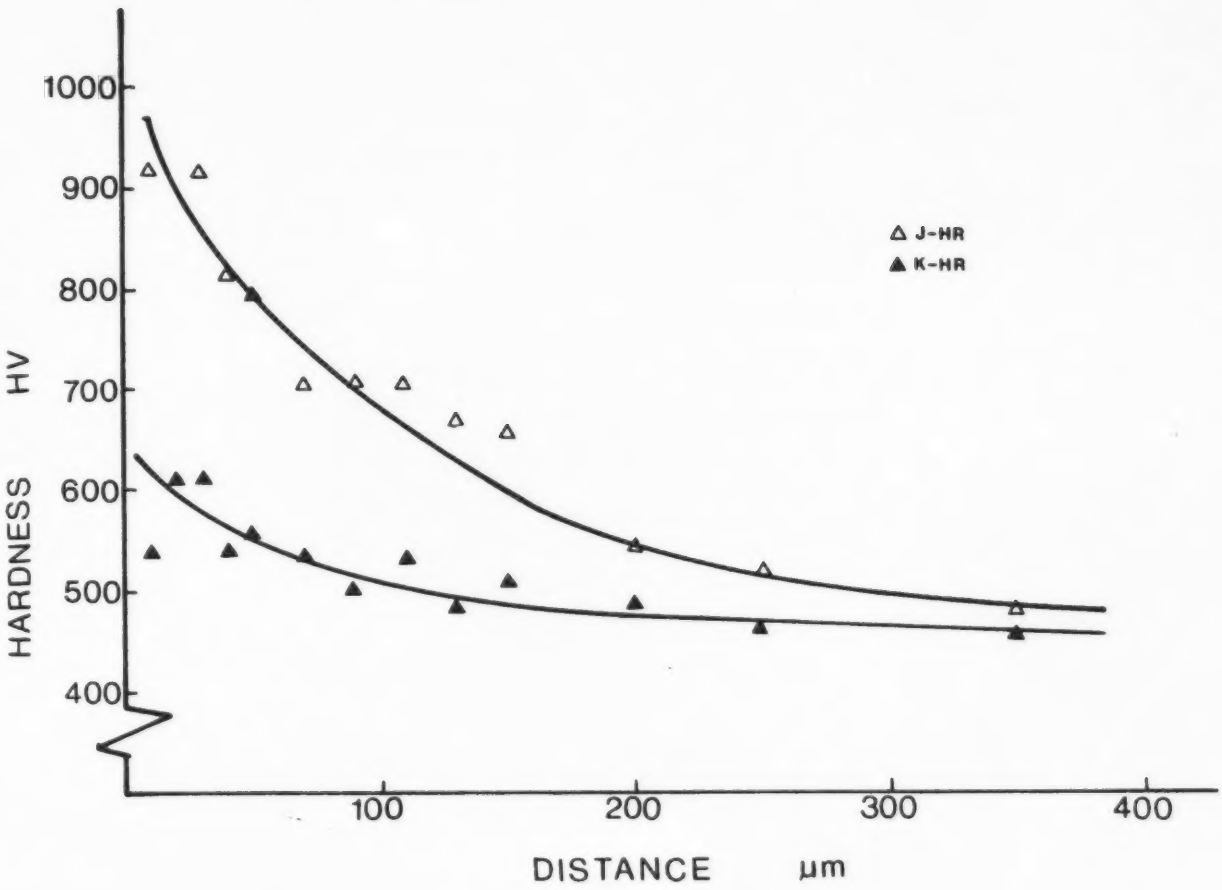

Figure 10: Gauge corner microhardness traverses, sample J-HR, and K-HR.

(a) Disk H-HR, 30 m below running surface

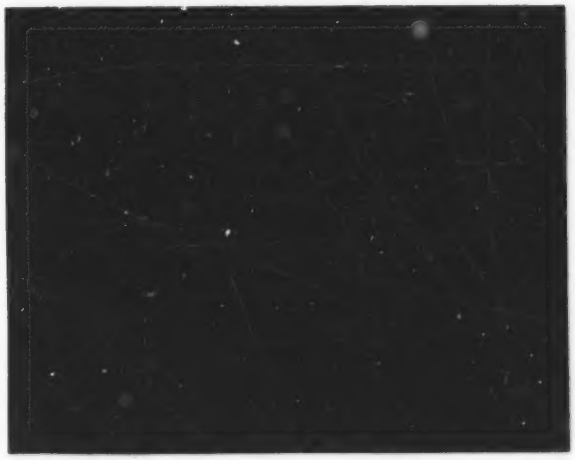

(b) Diffraction pattern corresponding to (a)

Figure 11: TEM, thinned foil.

(a) Bright field

(b) Dark field, 110 reflection

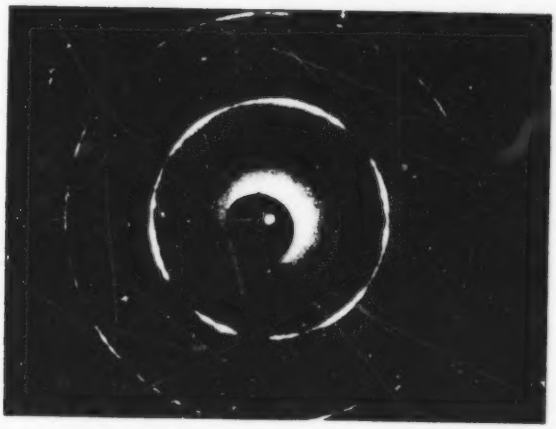

(c) Diffraction pattern

Figure 12: Disk I-HR, between gauge corner and centre of running surface. TEM, thinned foil.

(a) Disk A-HR, 70 m below running surface

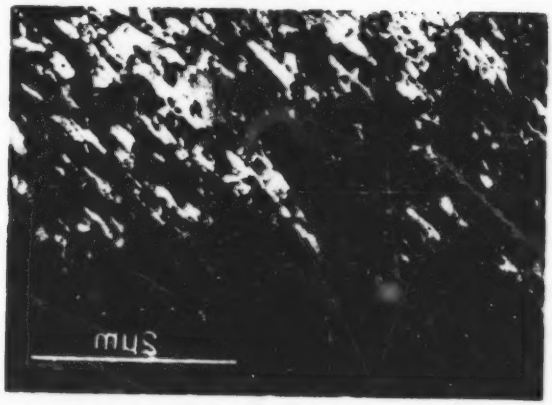

(b) Diffraction pattern corresponding to (a)

Figure 13: TEM, thinned foil.

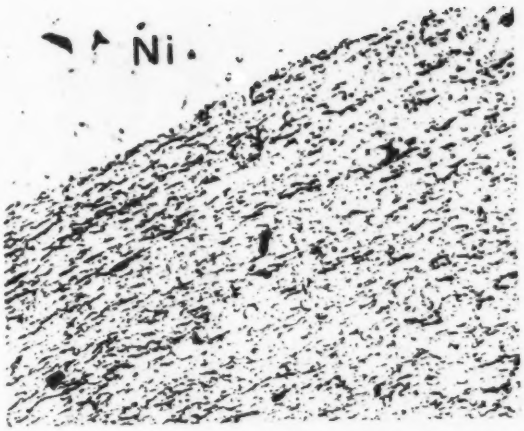

(a) J-HR, gauge corner surface

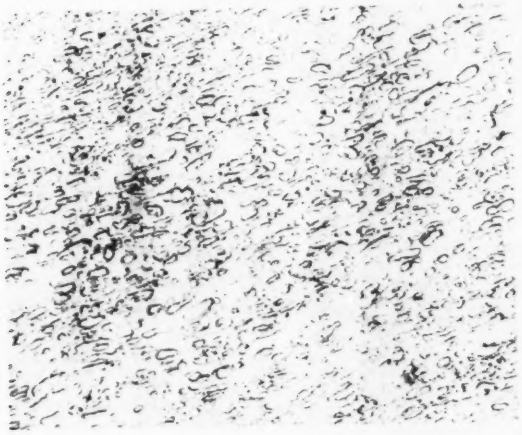

(b) J-HR, 50 μm below surface

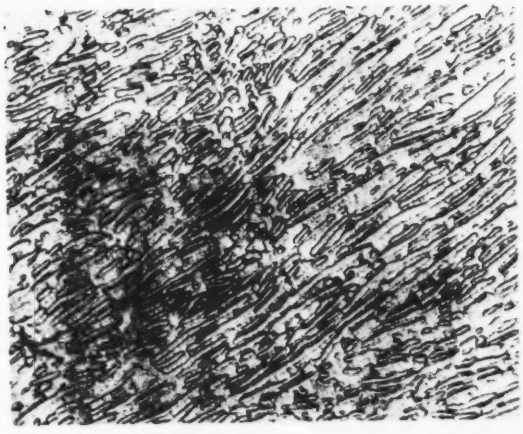

(c) J-HR, 500 μm below surface

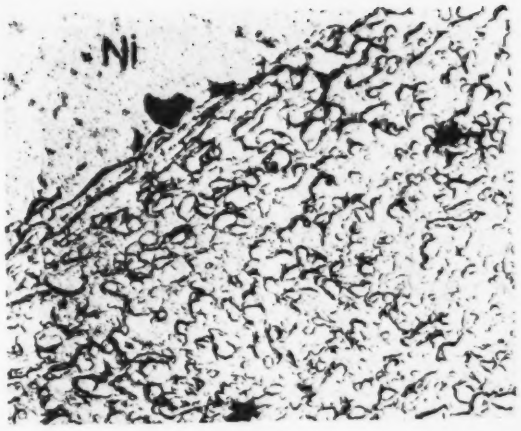

(d) K-HR, gauge corner surface

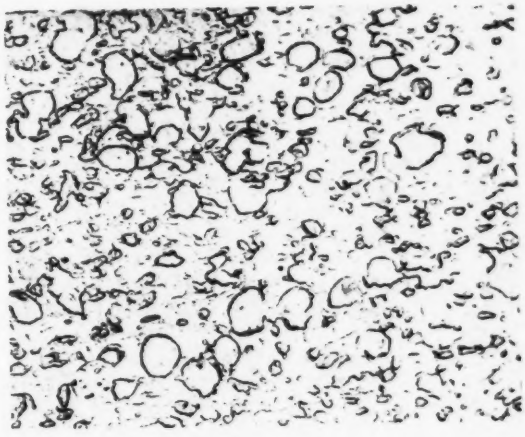

(e) K-HR, 50 μm below surface

(f) K-HR, 500 μm below surface

2 μm

Figure 14: Two-stage carbon replica, TEM.

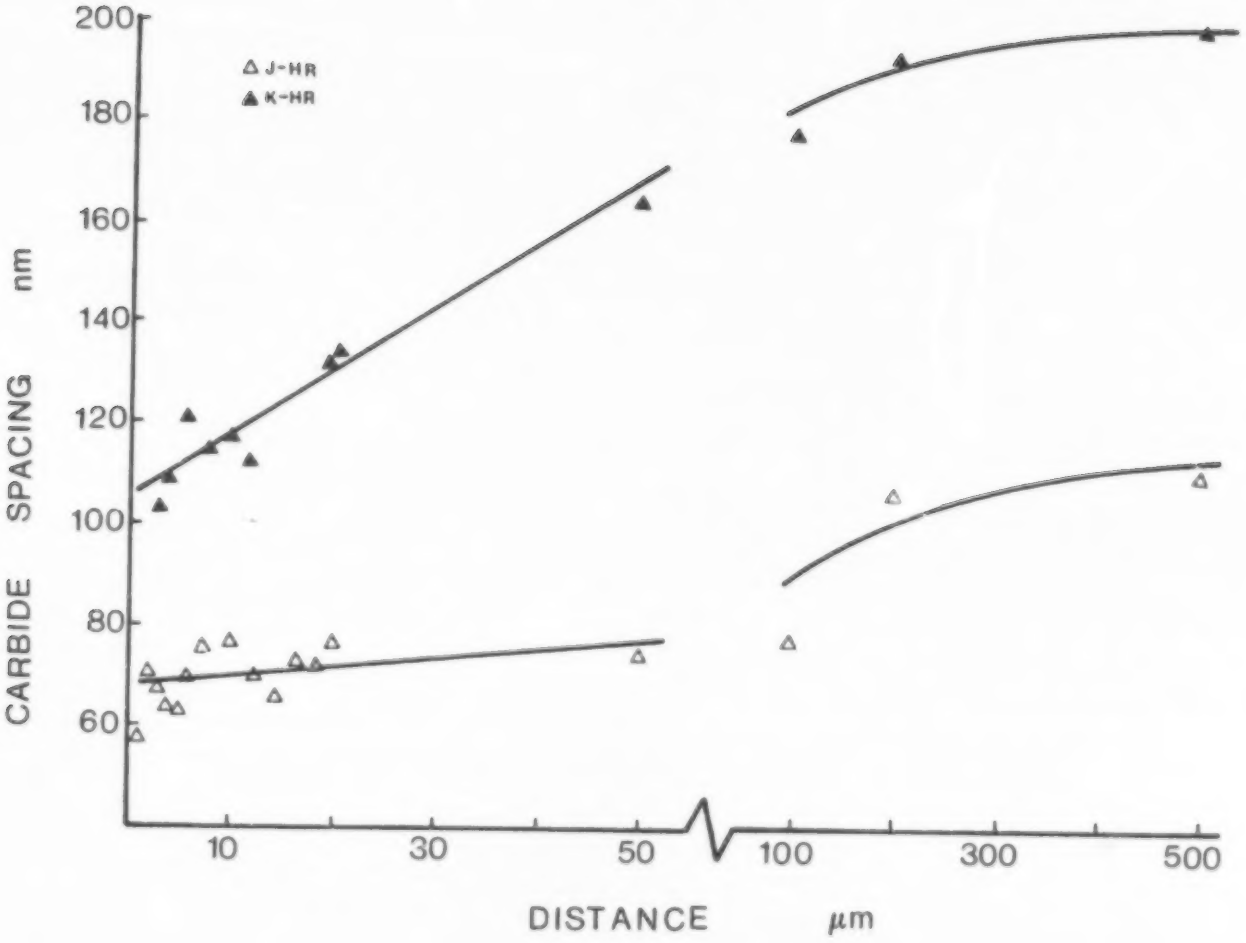

Figure 15: Inter-carbide spacing vs. depth below gauge corner surface (J-HR and K-HR)

POOR
QUALITY
ORIGINAL